UNIVERSITÄT HAMBURG
FAKULTÄT FÜR MATHEMATIK, INFORMATIK
UND NATURWISSENSCHAFTEN

Master Thesis

Towards on-chip THz spectroscopy of quantum materials and heterostructures

Gunda Kipp

gunda.kipp@mpsd.mpg.de
Degree Course: Physics
Student ID Number: 6665148
Semesters of Study: 11

1st Supervisor: PD Guido Meier
2nd Supervisor: Professor Andrea Cavalleri

December 5th, 2019

Abstract

On-chip THz spectroscopy is a powerful tool to investigate the low-energy dynamics of solids. THz pulses generated by photoconductive switches are confined to the near-field by metallic transmission lines, which allows studying micrometer sized heterostructures of different van der Waals materials. Routing sub-picosecond electrical pulses over several millimeters requires a transmission line geometry that avoids dispersion and damping. In this thesis, different geometries are fabricated and characterized to optimize the propagation of THz pulses for on-chip measurements. In addition, electromagnetic simulations are performed and compared to measured data.

The transmission lines are fabricated by optical lithography, thermal evaporation, and lift-off processing. This includes the integration of a heater stage in the thermal evaporator to grow high-quality metal / oxide substrates. The novel transmission line geometry developed for on-chip spectroscopy measurements provides improved signal propagation and a rather simple fabrication process.

To implement on-chip THz spectroscopy in complementary experiments, the photoconductive switches are required to be operated without direct optical access. In the framework of this thesis, first steps are taken to integrate the on-chip circuitry into a scanning near field optical microscopy (SNOM) setup at the Columbia University in New York. Triggering photoconductive switches with fiber-coupled laser pulses is tested and a stage is designed that allows sample mounting, beam alignment, as well as focusing via fiber optics in the SNOM.

Zusammenfassung

On-Chip-THz-Spektroskopie ist eine leistungsstarke Methode zur Untersuchung der niederenergetischen Dynamik von Festkörpern. Von photoleitenden Schaltern erzeugte THz-Pulse werden durch metallische Leitungen auf das Nahfeld begrenzt. Dadurch ist es möglich wenige Mikrometer große Heterostrukturen, welche aus verschiedenen van der Waals-Materialien zusammengesetzt sind, zu untersuchen. Um elektrische Pulse mit einer Dauer von weniger als einer Pikosekunde über mehrere Millimeter zu übertragen, wird eine Leitungsgeometrie benötigt, die Dispersion und Dämpfung gering hält. In dieser Arbeit werden verschiedene Geometrien hergestellt und charakterisiert, um die Propagation von THz-Pulsen für On-Chip-Messungen zu optimieren. Zusätzlich werden elektromagnetische Simulationen durchgeführt und mit den gemessenen Daten verglichen.

Die optimierten Signalleitergeometrien werden mittels optischer Lithographie, thermischer Deposition und Lift-off-Prozessen hergestellt. Dazu gehört die Integration eines beheizbaren Probenhalters in die thermische Verdampfungsanlage, um hochwertige Metall/ Oxid-Substrate zu erzeugen. Die neu entwickelte Leitungsgeometrie für On-Chip-Spektroskopie-Messungen überzeugt durch eine geringe Dämpfung und Dispersion in Kombination mit einem vergleichsweise einfachen Herstellungsverfahren.

Um die On-Chip-THz-Spektroskopie in komplementären Experimenten einsetzen zu können, müssen die photoleitenden Schalter ohne direkten optischen Zugang betrieben werden. Im Rahmen dieser Arbeit werden erste Schritte zur Integration der THz Schaltkreise in einen SNOM-Aufbau an der Columbia Universität in New York realisiert. Um die photoleitenden Schalter mit Laserpulsen zu betreiben, werden die Pulse durch optische Fasern geleitet. Zusätzlich wird ein Probenhalter entworfen, der die Kopplung, Ausrichtung sowie Fokussierung der optischen Fasern im SNOM ermöglicht.

Contents

1. Introduction

Today's world is defined by technology. Multifunctional devices revolutionizing our everyday life are becoming increasingly faster and smaller. The exploration of quantum materials is thus key to open the door for a new generation of electronics and photonics devices with still unimaginable functionalities. The experimental realization as well as gaining control over quantum phases of matter is of particular importance, since this will potentially provide access to quantum phenomena on demand [1].

The characteristic energy scale of electronic interactions in solids ranges from 0.4 meV to 40 meV (0.1 THz to 10 THz) [2]. Therefore, terahertz spectroscopy is a powerful tool to investigate quantum materials and 2D heterostructures [3]. The stable generation and detection of THz radiation (sub-picosecond pulses in time-domain) was extremely difficult for a long time. In the 1960s, a breakthrough was achieved by Auston by developing photoconductive switches [4], which can generate or detect THz fields when triggered by femtosecond laser pulses. But only when mode-locked sub-picosecond lasers were introduced in the early 1980s, THz pulses could be generated and detected reliably, and the door towards THz spectroscopy was opened.

The long wavelengths of THz radiation (3000 µm to 30 µm) limits the resolution in far-field experiments [5]. For example, the resolution limit of 1 THz is 150 µm (half the wavelength) [6]. Thus, far-field THz spectroscopy is restricted to large samples. Moreover, the lowest frequencies generated in far-field THz spectroscopy end at 500 GHz [7].

In recent years, 2D quantum materials and heterostructures with dimensions of the order of ten micrometers have become an active topic of research. However, their small size precludes the use of far-field THz techniques. But by putting THz spectroscopy on-chip, THz pulses generated by photoconductive switches can be confined to the near-field by metallic transmission lines. Thereby, one overcomes the diffraction limit and it is possible to study these tiny structures.

On-chip THz spectroscopy has other advantages as well. For example, the bandwidth spans DC all the way up to a few THz, exceeding that of conventional far-field THz spectroscopy. Additionally, the on-chip THz devices incorporating the sample material allow more control. The small structures can directly be contacted by metal leads and currents can be applied at room as well as cryogenic temperatures. The Fermi level can also be gated.

To do this, THz circuits are required where only one single mode propagates in the transmission line. Recently, such circuits were used to measure the light-induced anomalous Hall-effect in graphene [8]. In this experiment, ultrafast transport properties of monolayer graphene, driven by a mid-infrared femtosecond pulse of circularly po-

larized light, were measured and an anomalous Hall effect in the absence of an applied magnetic field was observed. In this case, the THz circuitry enabled a quantitative measure of anomalous ultrafast Hall currents in graphene.

The THz circuitry was fabricated on doped silicon wafers with dry oxide layer, which formed in combination with the metallic transmission lines a microstrip. Ultrafast Hall currents generated in the graphene were routed in the microstrip, before they were detected by laser-triggered photoconductive switches. The microstrip geometry has a number of advantages such as single-mode propagation, the possibility to gate the Fermi level of the sample by changing the potential of the doped silicon as well as out of plane electric fields. In principle, these circuits could also be used in THz spectroscopy. However, signals suffered notably from dispersion and damping before being detected, which would prevent meaningful THz spectroscopy experiments in future studies.

Thus, there is an urgent need to develop circuitry capable of transporting sub-picosecond current and voltage pulses on-chip with reduced dispersion and damping. Therefore, it is the goal of this thesis to develop and characterize different transmission line geometries to find the best candidate for on-chip THz spectroscopy.

This thesis is organised in the following way: The theoretical background of on-chip THz spectroscopy and transmission lines is provided in chapter 2. Chapter 3 contains the experimental part of this thesis. This chapter includes the design of THz circuits, methods to grow high-quality metal / oxide substrates as well as the fabrication of different transmission line geometries. Further, the experimental setup and the on-chip measurements are introduced. The experimental results are presented and compared to electromagnetic simulations in chapter 4. In chapter 5 the results of this thesis are discussed. The final chapter gives a conclusion of this thesis and an outlook for further implementation of this project in complementary experiments, where first steps are already taken in the framework of this thesis.

2. On-chip THz spectroscopy

This chapter introduces the basics of far-field and near-field THz spectroscopy. Firstly, an overview over THz generation and detection for conventional far-field spectroscopy is given. This work focusses on near-field THz spectroscopy, which is described in the following section. Near-field spectroscopy is particularly useful to study the low-energy dynamics of samples with dimensions below the diffraction limit of THz radiation. To perform near-field spectroscopy, THz radiation needs to be generated, captured, and detected in an on-chip transmission line geometry.

Section 2.2 explains the fundamentals of THz transmission lines, including the Telegrapher's equation, the signal propagation model as well as the skin effect. This background is crucial to understand and eliminate the undesired effects of dispersion and damping during signal propagation.

At the end of this chapter, three different transmission line geometries, which are studied in this work, are discussed in detail.

2.1. THz spectroscopy

Terahertz (THz) spectroscopy has been employed to detect and control properties of matter with electromagnetic radiation between the microwave and the infrared (IR) region (see figure 2.1). The THz spectrum is defined within the frequency range of 0.1 THz to 10 THz, corresponding to wavelengths of radiation from 3000 µm to 30 µm and energies ranging from 0.4 meV to 40 meV [5].

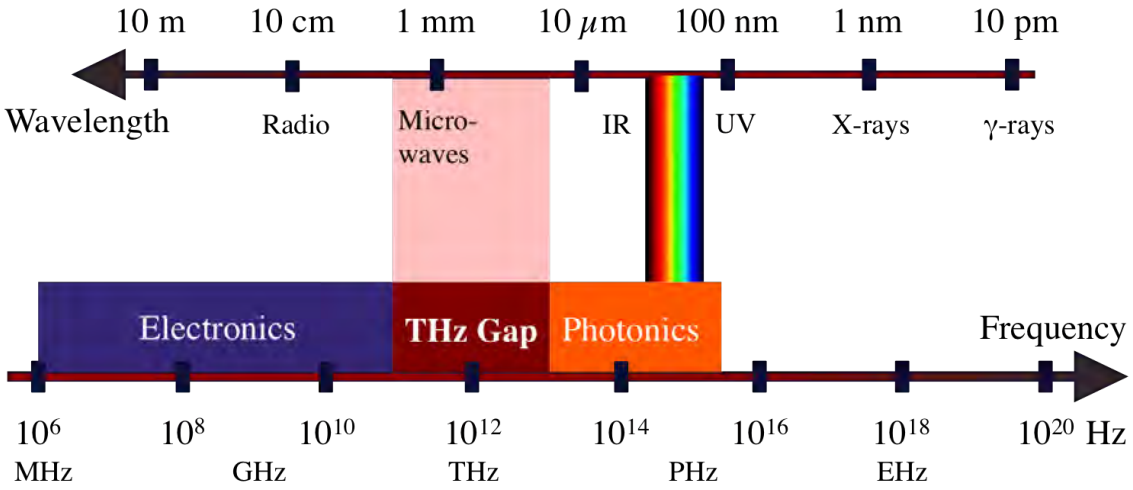

Figure 2.1.: Spectrum of electromagnetic radiation from low energies (left) to high energies (right). The THz spectrum ranges from 30 µm to 3000 µm.

Thus, the THz spectrum bridges the gap between millimeter (electronic) and submillimeter (photonic) wave technologies (therefore, called the THz gap). Terahertz waves are nonionizing, noninvasive, and penetrate materials with penetration depths smaller than that of microwave radiation. The radiation is also very sensitive to many different kinds of resonances as for example translational, vibrational, rotational and torsional states, providing material information, which is not accessible with other techniques [9]. Therefore, THz radiation provides a powerful and unique tool to explore a wide variety of physical phenomena, such as optical phonons in crystals [10], superconductor gaps [11], and Josephson plasma resonances [12].

Compared to its neighbouring frequency ranges, the THz-gap has been less developed since it was hard to generate and detect THz radiation with conventional methods of photonics and electronics. The technology experienced a great breakthrough when broadband THz sources were developed [13]. There are various different methods nowadays to generate and detect THz radiation such as electronic, laser and optically driven sources (see Zouaghi *et al.* [7]). This thesis focusses on optically driven sources, which will be discussed in the following and used for experiments in this work.

2.1.1. THz sources and detection for far-field spectroscopy

Optically driven THz sources rely on frequency conversion of femtosecond lasers, which delivers coherent few-cycle pulses. Thereby, time-domain THz spectroscopy becomes possible, with the ability to characterize the electric field of a THz pulse with full phase and amplitude information [14].

There are two different ways to generate THz pulses among the optically driven sources: Either by optical rectification or by using a photoconductive switch. Optical rectification is a second order nonlinear process. When a laser pulse with a duration of less than 1 ps hits a non-linear crystal, the outcome is a very short single-cycle electromagnetic pulse in the frequency range between 500 GHz and a few THz. The detection of the generated fields can be performed with electro-optical sampling [14].

However, if frequencies below 500 GHz are required, photoconductive switches are the means of choice. Photoconductive switches can be used for both generation and detection at room- as well as cryogenic temperatures. They were first developed by David H. Auston at Bells Labs in the 1960s and are therefore referred to as Auston switches [15].

Figure 2.2 shows a schematic of a photoconductive switch. The switch consists of a transmission line antenna which is bridged by a semiconductor with a short carrier lifetime, such as gallium arsenide or silicon [4]. The two electrodes of the antenna are biased with a voltage of 10 - 100 V. Without focusing a laser beam on the semiconductor,

the switch acts as an insulator. When the semiconductor is hit by a femtosecond laser pulse, electrons are promoted from the valence band into the conduction band, creating free carriers (see figure 2.2 (b)). Subsequently, the free carriers are accelerated by the bias field, leading to a transient current pulse $I(t)$ (see figure 2.2 (c)). The duration of the current pulse is determined by the carrier relaxation time. As depicted in figure 2.2 (d), the transient current generates a coherent single-cycle THz pulse. For silicon photoconductive switches, green laser light ($\sim$ 520 nm wavelength) is required to make this process happen efficiently [16], [17].

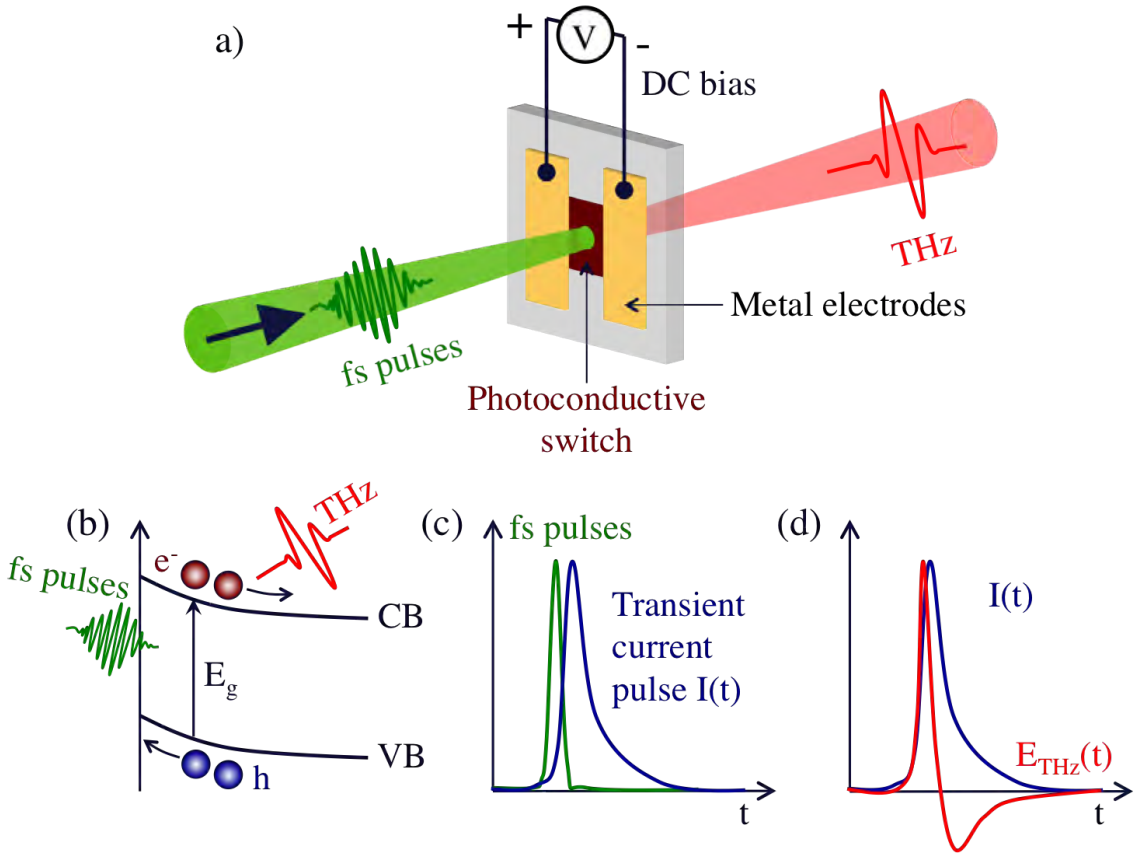

Figure 2.2.: Generation of far-field THz radiation with a photoconductive switch: (a) A photoconductive silicon switch is biased by two metal electrodes and illuminated by 520 nm femtosecond laser pulses to generate THz radiation. (b) General THz emission process in wide gap semiconductors (silicon): A femtosecond laser pulse promotes electrons from the valence band (VB) to the conduction band (CB). (c) The generated carriers are accelerated by the bias field, which creates a transient current pulse I(t). (d) The transient current pulse induces the emission of a THz field (inspired by [5], [18]).

In order to use a photoconductive switch as a detector, the geometry is kept but no bias voltage is applied (see figure 2.3) [19]. Instead, the incident THz field acts as a bias to the photoconductive switch. When the switch is activated by a much shorter ($\sim$ 100 fs) laser pulse, the excited photo-charge carriers are accelerated by the electric field of the THz pulse and a photocurrent flows through the metal electrodes, which

can be measured. The magnitude of the current is related to the THz field strength during the time of switch activation. Therefore, the entire span of the THz pulse can be sampled by varying the time delay between the femtosecond gate pulse and the incident THz pulse (see figure 2.3).

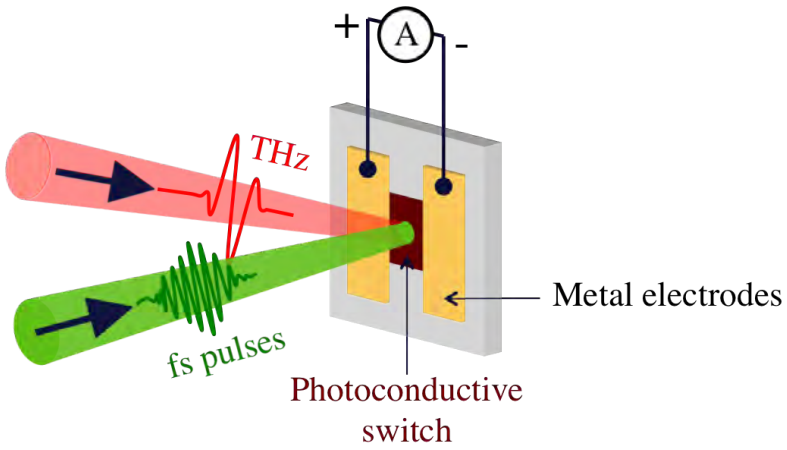

Figure 2.3.: Detection of a THz field with a photoconductive switch: The incident THz field acts as a bias for the photoconductive switch. Upon illumination with short femtosecond laser pulses, photocurrents are generated, which can be measured.

The concepts explained so far concerning THz generation and detection are used for free space THz time-domain spectroscopy, using the generated far fields to analyse materials. The spatial resolution of far field spectroscopy is approximately limited to the wavelength of THz radiation. Thus, many interesting 2D heterostructures such as twisted bilayer graphene, which can only be produced on micrometer scales, cannot be studied with far field spectroscopy. In the next section, the concept of near-field THz spectroscopy is introduced which allows to study samples with micrometer dimensions.

2.1.2. Near-field THz spectroscopy using transmission lines

For near-field THz spectroscopy, photoconductive switches are embedded in transmission line structures. This approach allows to confine the THz radiation generated by photoconductive switches to the near field and to guide the radiation to the sample position. Among higher spatial resolution due to the near field confinement, the integration of THz generation and detection in an on-chip circuitry yields additional advantages: The sample is contacted by the transmission line which allows to send ultrafast current pulses generated by a photoconductive switch into the sample. Also, the Fermi level of the material of interest can be tuned by gating and a much higher frequency resolution ($\sim$ 2 GHz or greater) can be realized by carefully designing the device [5].

A typical on-chip THz spectroscopy setup is shown in figure 2.4: Two photoconductive silicon switches are connected by a transmission line. The generation switch on the left is biased with a DC bias voltage and is excited by focused pump laser pulses of 520 nm wavelength. Thereby, the switch becomes highly conductive and current pulses are coupled to the metallic transmission line, in which they propagate towards the detection switch. The detection switch is excited by a time delayed probe beam of the same wavelength, which excites photo-charge carriers in the photoconductive gap ($\sim 3\,\mu m$). The THz pulse acts as a bias voltage for the detection switch (similar to the free space THz system). When the detection switch is activated while the THz pulse passes by, a photocurrent is generated, which can be measured by the combination of a transimpedance amplifier and a lock-in amplifier, getting feedback from a mechanical chopper. By using an optical delay stage, the probe beam can be delayed in time and the full THz pulse can be mapped.

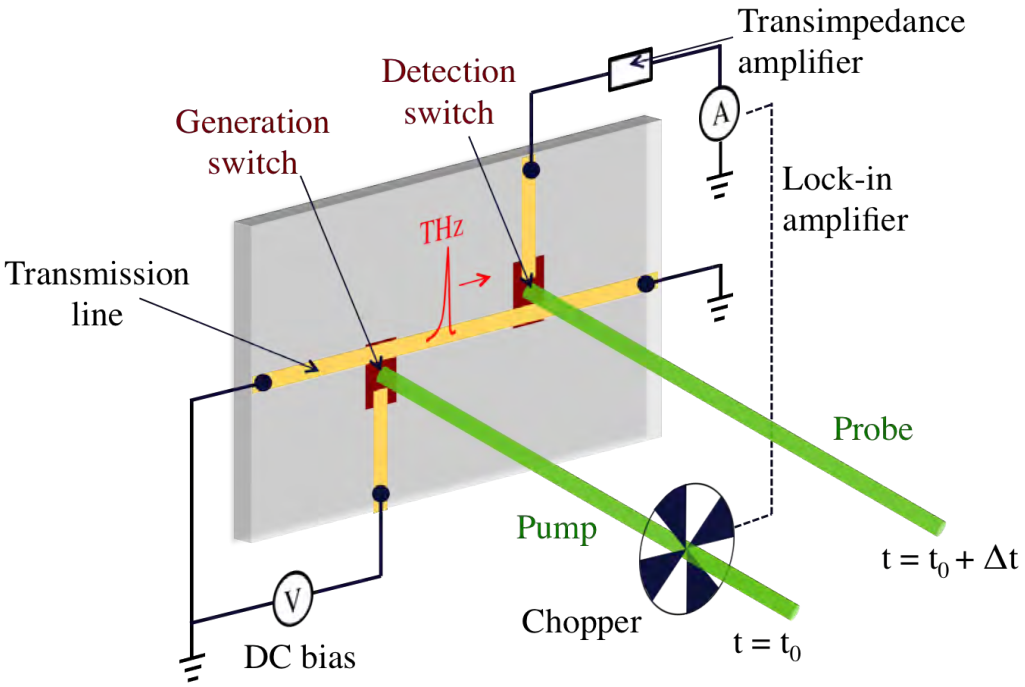

Figure 2.4.: On-chip transmission line system for THz generation and detection: Photoconductive switches are embedded in a metal transmission line to transmit a THz pulse from the generator switch to the detector switch. To sample the entire THz field, the probe beam is delayed with respect to the pump beam. Photocurrents can be measured by a lock-in amplifier using a mechanical chopper for the pump beam.

In former experiments performed by McIver *et al.* [8], such on-chip THz devices were fabricated on doped silicon wafers with a 285 nm SiO_2 layer on top. The doped silicon plane with the oxide layer in combination with the metal line form a microstrip (see chapter 2.3.1) which has various advantages: Silicon wafers are easily accessible substrates, doped silicon can be used as a backgate for tuning the Fermi-level of the re-

spective material, e.g. graphene, and only a single mode is propagating. Nevertheless, the problem was, that THz pulses travelling in such transmission lines over distances in the range of a few hundreds of micrometers suffered from dispersion. Especially in ultrafast transport experiments using THz on-chip spectroscopic techniques, non- or low-dispersive pulse propagation is essential in order to directly measure the induced currents.

In the framework of this thesis, low-dispersive single-mode transmission lines are developed and characterized, with the goal to overcome the above mentioned problems. To understand the pulse propagation between the generation and to be able to develop low-dispersive single-mode transmission lines, the theory of transmission lines is explained in the next chapter.

2.2. Theoretical description of transmission lines

This chapter is dedicated to the fundamental concepts of transmission line theory. Particularly, on-chip planar transmission lines such as microstrips, striplines and coplanar waveguides are discussed here with special emphasize on the frequency regime up to the THz range. All three types of transmission lines are utilized in the experimental section.

2.2.1. Overview

In telecommunication theory, a *transmission line* is defined as a region of space where RF signals can propagate with the best compromise between minimum attenuation and available space. Depending on the transmission line shape, different frequency ranges are transmitted [20].

There are four different types of transmission lines: Coupled wires, parallel plates, coaxial cables and waveguides, whereby the first three types belong to the family of *two conductor* transmission lines, which are treated in this thesis. The physical dimensions of the transmission lines highly influence the natural propagation mode of the line [20].

Each transmission line has one fundamental polarization as well as one fundamental mode of propagation. Both phenomena are of course strongly frequency-dependent and it is also possible that at some frequencies other modes than the fundamental mode propagate [20]. Possible propagation modes for signals travelling in positive x direction are shown in the following table 2.1.

Further, only "long" transmission lines are discussed, where the line length is larger than the maximum wavelength component of the signal divided by four. In this case, wave characteristics of the signal arise.

Table 2.1.: Propagation modes in transmission lines

TE, transverse electric	$E_x = 0$	$H_x \neq 0$
TM, transverse magnetic	$E_x \neq 0$	$H_x = 0$
TEM, transverse electro-magnetic	$E_x = 0$	$H_x = 0$

2.2.2. Telegrapher's equations

Transmission line problems are solved using Heaviside's *transmission line model* [21], which is based on Maxwell's equations. Two sets of linear differential equations exist, which can be applied to every transmission line. The so called telegrapher's equations describe the voltage V and current I along the transmission line with its characteristic impedance Z_0 with respect to distance and time.

In the transmission line model, a two conductor transmission line, which connects a power source to a load, can be represented by a distributed network. The transmission line is divided into infinitesimal pieces dx, when signals are propagating in positive direction x (see figure 2.5).

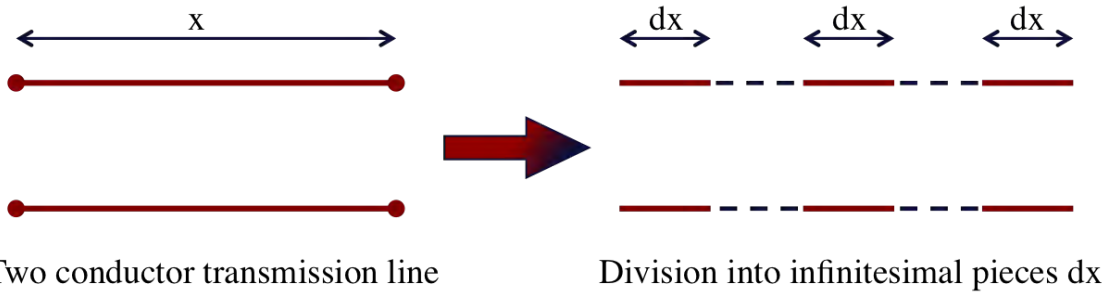

Figure 2.5.: Two conductor transmission line and its distributed network representation: For signals propagating in positive x direction, the transmission line is divided into infinitesimal segments dx.

Furthermore, every infinitesimal piece dx can be modelled as a lumped element circuit with the primary line constants R', L', C' and G' specified per unit length as shown in figure 2.6. R' represents the series resistance due to the finite conductivity of the conductor (expressed in ohms per unit length), L' is the distributed inductance due to self-inductance of the conductor which is represented by a series inductor (in henries per unit length). C' is the capacitance between the two conductors standing for a shunt capacitor, since some electrical energy is stored (expressed in farads per unit length). G' is the conductance which is responsible for the loss in the dielectric material (lossy by nature) separating the two conductors and is represented by a shunt resistor between the signal line and the ground line (in siemens per unit length).

Applying Kirchhoff's circuit laws to the lumped model shown in figure 2.6, the fol-

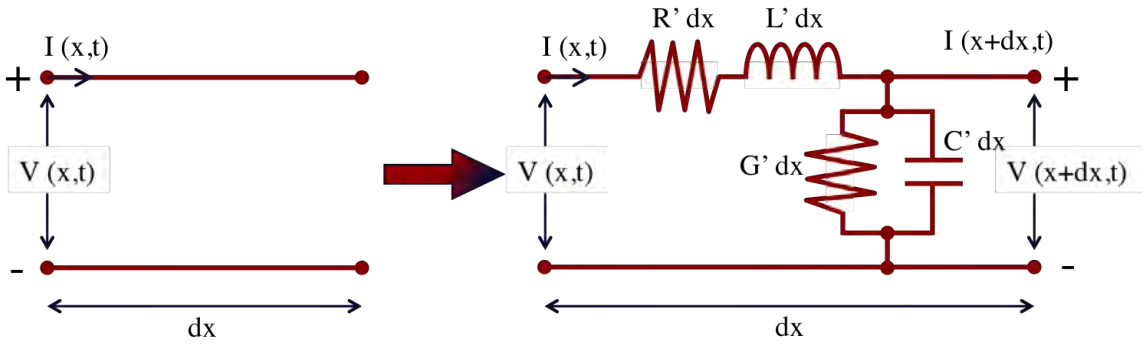

Figure 2.6.: A two conductor transmission line (left) can be represented by a lumped element circuit with the elementary components resistance R', inductance L', capacitance C' and conductance G'. The transmission line consists of an infinite series of the elements shown in the infinitesimal segment of the transmission line.

lowing equations can be found:

$$V(x,t) = R'dx\,I(x,t) + L'dx\,\frac{\partial}{\partial t}I(x,t) + V(x+dx,t) \tag{2.1}$$

$$I(x,t) = G'dx\,V(x,t) + C'dx\,\frac{\partial}{\partial t}V(x,t) + I(x+dx,t). \tag{2.2}$$

By applying the mathematical definition of the derivative and using the phasor forms for time-varying voltage and current as shown in Ref. [22], the telegrapher's equations can be derived:

$$\frac{d}{dx}V(x,t) = -(i\omega L' + R')\,I(x) \tag{2.3}$$

$$\frac{d}{dx}I(x,t) = -(i\omega C' + G')\,V(x). \tag{2.4}$$

Differentiating again, the two following differential equations can be obtained:

$$\frac{d^2V(x)}{dx^2} = (R' + i\omega L')(G' + i\omega C')\,V(x) = \gamma^2\,V(x) \tag{2.5}$$

$$\frac{d^2I(x)}{dx^2} = (R' + i\omega L')(G' + i\omega C')\,I(x) = \gamma^2\,I(x), \tag{2.6}$$

with the complex propagation constant γ:

$$\gamma = \alpha + i\beta = \sqrt{(R' + i\omega L')(G' + i\omega C')}, \tag{2.7}$$

where the real part α is the attenuation constant (signal amplitude reduction) and the imaginary part β is the phase constant that corresponds to the angular wavenumber. Attenuation arises from three different phenomena: conductor loss α_c, dielectric loss α_d and radiation loss α_r. Thus, the propagation constant (which is not constant, but

frequency dependent) is a measure for the undergone change of amplitude and phase of a sinusoidal wave propagating in one direction in a transmission line. For a complex amplitude A_0 at the source and the changed amplitude A_x after a distance x, the propagation constant is defined as

$$\frac{A_0}{A_x} = \mathrm{e}^{-\gamma x}. \tag{2.8}$$

Another important parameter for a transmission line is the characteristic impedance Z. It is a function of geometry and materials, and its value is independent of the transmission line length [23]. Z measures the ratio of the amplitudes of voltage and current of a wave propagating in one direction in a transmission line without any reflections in the other direction. For a transmission line with infinite length, the characteristic impedance is defined to be equal to the input impedance.

Based on the telegrapher's equations, the characteristic impedance Z can be expressed by

$$Z = \sqrt{\frac{R' + i\omega L'}{G' + i\omega C'}}. \tag{2.9}$$

Z is a complex parameter, whose absolute value $|Z|$ and phase Φ are shown as function of frequency ω in figure 2.7. The characteristic impedance reaches the value $|Z| = \sqrt{R'/G'}$ for frequencies $\omega \to 0$. In the weak damping limit, for frequencies $\omega \gg R'/L'$ and $\omega \gg G'/C'$ (occurs for THz frequencies), Z becomes real (Im(Z) $\simeq$ 0) and approaches the value

$$Z_0 = \sqrt{\frac{L'}{C'}}. \tag{2.10}$$

The transition frequencies to the weak damping limit are not fixed values for every transmission line. They are dependent on the primary line constants R', L', C' as well as G' and vary between different transmission line types and geometries.

The primary line constants R', L', C' and G' can be derived from the secondary line constants γ and Z by multiplication or division of equations 2.7 and 2.9:

$$R' = Re[Z \cdot \gamma], \quad L' = \frac{Im[Z \cdot \gamma]}{\omega}, \quad G' = Re\left[\frac{\gamma}{Z}\right], \quad C' = \frac{Im\left[\frac{\gamma}{Z}\right]}{\omega}. \tag{2.11}$$

Further, also the real part α and the imaginary part β of the propagation constant γ can be visualized as function of frequency ω, as shown in figure 2.8. The attenuation constant α has at low frequencies $\omega \to 0$ its minimum value α_{min}:

$$\alpha_{min} = \sqrt{R'G'}. \tag{2.12}$$

In the weak damping limit, the attenuation constant α approaches the value

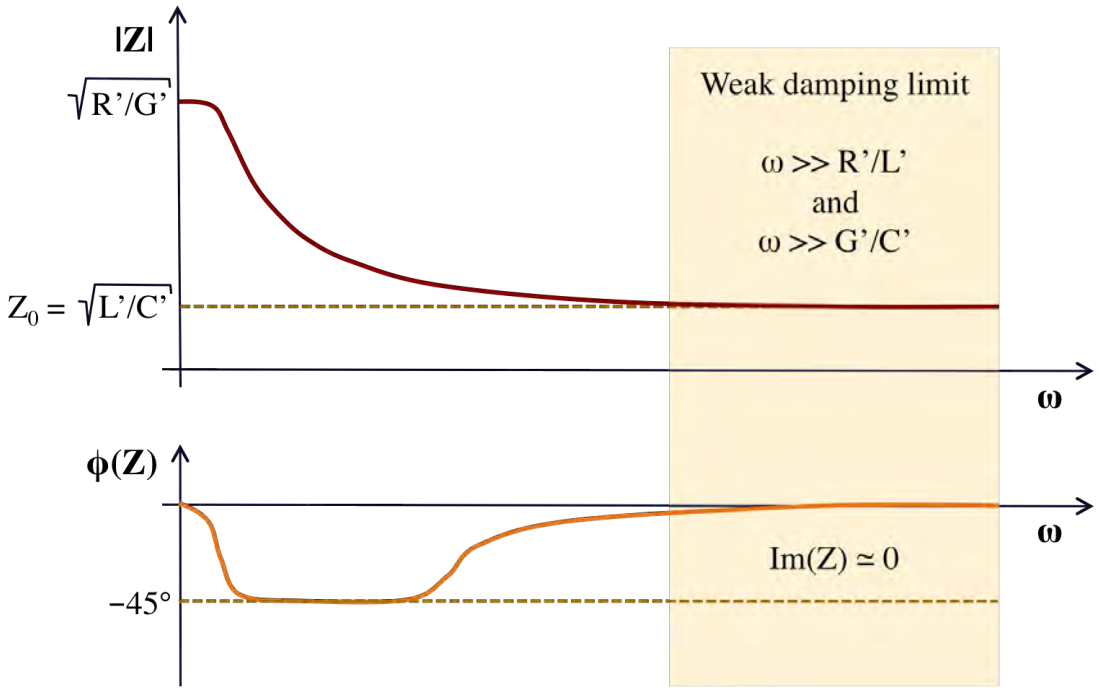

Figure 2.7.: Absolute value $|Z|$ and phase Φ of the characteristic impedance Z as function of ω: In the weak damping limit Z becomes real and approaches Z_0.

$$\alpha_0 = \frac{1}{2}\left(\frac{R'}{Z_0} + G'Z_0\right). \tag{2.13}$$

Thus, weak damping limit does not mean, that the attenuation constant has a minimum value. Furthermore, the attenuation constant is constant for the frequency range of the weak damping limit and thereby signals in this frequency range are propagating as if they would not experience any losses or dispersion.

Signals can be composed of many different frequencies. Since different frequency components propagate at different velocities, pulses suffer from distortion, which is known as dispersion. Therefore, a distortionless propagation is only possible when all waves travel with the same velocity. This comes true in the weak damping limit. The phase constant β corresponds to the wavenumber k:

$$\beta = k = \frac{2\pi}{\lambda} \tag{2.14}$$

and in the weak damping limit, β approaches linearly the curve $\omega\sqrt{L'C'}$ (see figure 2.8). Since the phase velocity is defined as

$$v_{ph} = \frac{\lambda}{T} = \frac{\omega}{\beta}, \tag{2.15}$$

the phase velocity is $1/\sqrt{L'C'}$ in the weak damping limit and is independent of the frequency ω. Usually, signals containing many different frequencies are not only com-

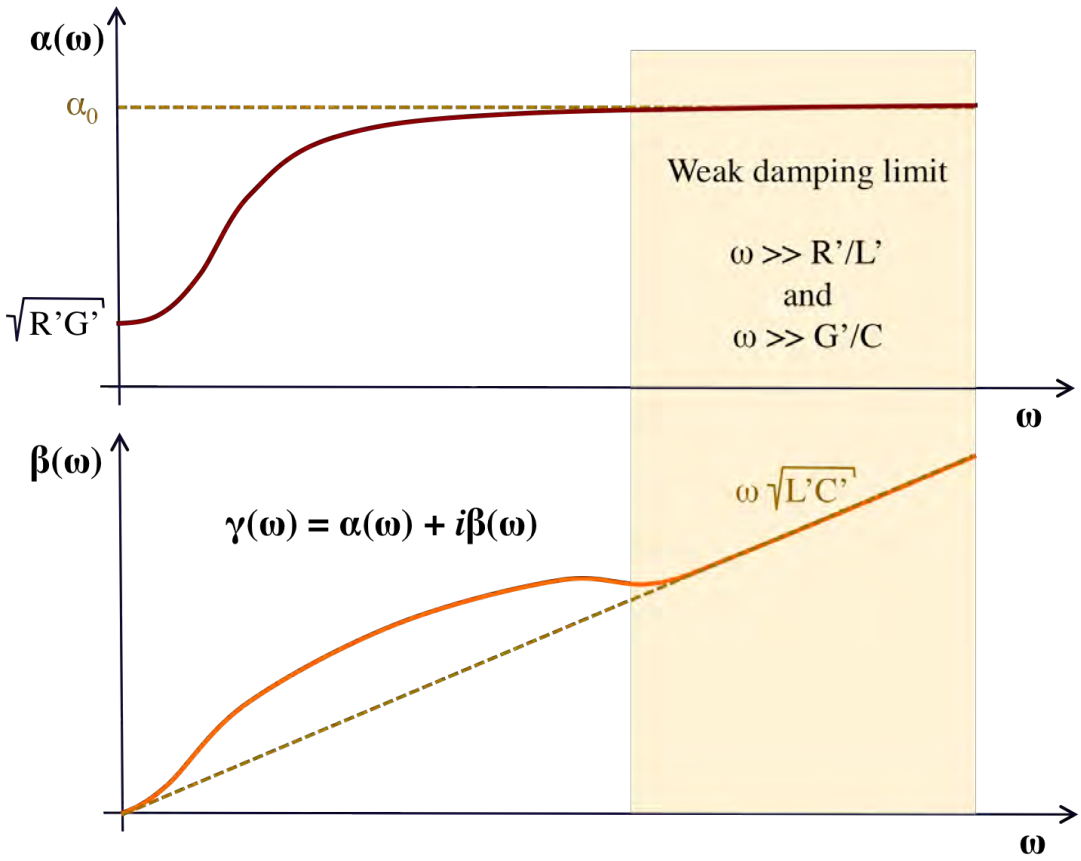

Figure 2.8.: Attenuation constant α and phase constant β as function of ω: $\alpha(\omega)$ approaches α_0 and $\beta(\omega)$ becomes proportional to ω in the weak damping limit.

posed of frequencies in the weak damping limit. Thus, lower frequencies have lower phase velocities and signal distortion occurs. However, the highest frequency components of the signal propagate with the maximum phase velocity without distortion.

2.2.3. Signal propagation model

Another approach to calculate the wave propagation in a transmission line was shown by Thiede [24]. This approach has the additional advantage that signal propagation can be modelled in a simple and visual way.

Thiede understands the propagation constant as a sum of three factors:

$$\gamma = i\omega\sqrt{L'C'} + D\sqrt{L'C'} + \sqrt{L'C'}\left(\sqrt{(i\omega+D)^2 - K^2} - (i\omega+D)\right). \tag{2.16}$$

Equation 2.16 is a transformation of equation 2.7 with the newly introduced damping factor D and distortion factor K:

$$D = \frac{1}{2}\left(\frac{R'}{L'} + \frac{G'}{C'}\right), \quad K = \frac{1}{2}\left(\frac{R'}{L'} - \frac{G'}{C'}\right). \tag{2.17}$$

In the resulting exponential equation

$$e^{-\gamma x} = e^{-i\omega\sqrt{L'C'}x} + e^{-D\sqrt{L'C'}x} + e^{-\sqrt{L'C'}\left(\sqrt{(i\omega+D)^2-K^2}-(i\omega+D)\right)x} \tag{2.18}$$

the first term corresponds to the time delay of the signal $\tau = \sqrt{L'C'}x$, the second term is seen as a damping factor $e^{-\alpha_0 x}$ with the damping constant $\alpha_0 = D\sqrt{L'C'}$ and the third factor can be interpreted as a signal distortion. An exemplary propagation of a rectangular signal modelled with this approach is shown in figure 2.9.

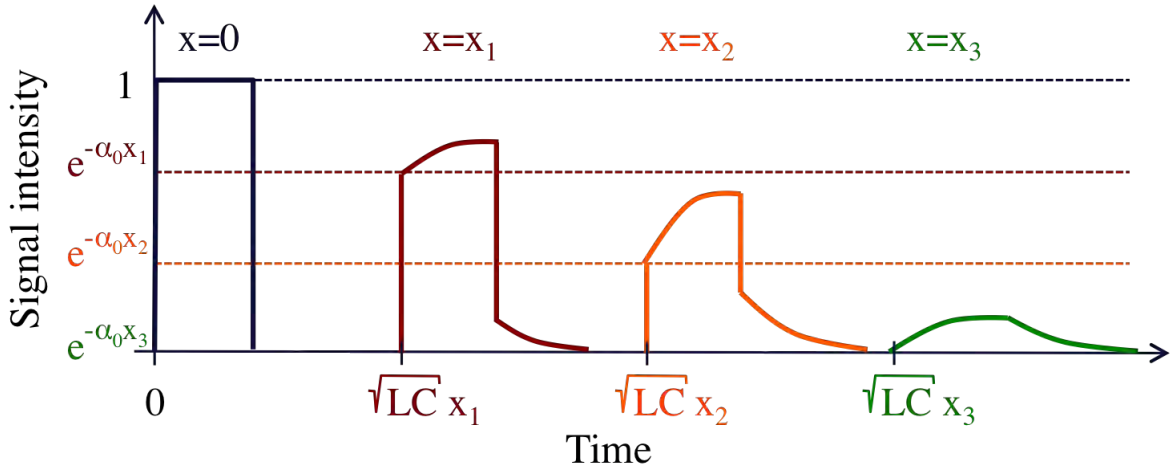

Figure 2.9.: Exemplary propagation of a rectangular signal in a transmission line: A pulse propagating with a maximum phase velocity of $\frac{1}{\sqrt{L'C'}}$ experiences damping (damping constant α_0) and distortion. The maximum phase velocity (phase velocity of the highest frequencies contained in the signal) can be found at the steepest slope.

The damping constant α_0 should not be confused with the attenuation constant α, the real part of the propagation constant (see equation 2.7), because also the third term of equation 2.16 has a real part and contributes to the damping. But α_0 equals α when the transmission line is distortionless, where the third term of equation 2.18 is zero.

As shown by Thiede, also the characteristic impedance Z can be expressed as a function of damping factor D and distortion factor K:

$$Z = Z_0\sqrt{\frac{i\omega+D+K}{i\omega+D-K}}, \tag{2.19}$$

where Z_0 is again the characteristic impedance of a distortionless transmission line. Z equals Z_0 when the distortion factor K is zero, which is the case when the Heaviside condition is fulfilled:

$$\frac{R'}{L'} = \frac{G'}{C'}. \tag{2.20}$$

This is the condition for a distortionless, but not for a lossless transmission line,

because in the distortionless case (weak-damping limit) the attenuation constant α has a non-zero value of α_0 (see figure 2.8).

2.2.4. Skin effect

In the previous sections, the primary line constants R', L', C' and G' were assumed to be constant within pulse propagation in the transmission line and with respect to the propagating frequencies. However, the so called skin effect changes the effective conductor resistivity dependent on the frequency of the propagating signal.

The skin effect defines the phenomenon that high-frequency alternating currents (and magnetic flux) penetrate into the surface of a conductor only up to certain depths, the so called skin depth. Therefore, the current density is largest near the conductor surface and decreases with greater depths in the conductor (see figure 2.10). The skin depth (depth in meters at which the current density is $1/e$ of the surface current density) is defined in the good conductor limit ($\sigma \gg \varepsilon_0 \varepsilon_r \omega$) by

$$\delta = \sqrt{\frac{2\rho}{\omega \mu_0 \mu_r}} = \sqrt{\frac{2}{\omega \mu_0 \mu_r \sigma}}, \tag{2.21}$$

where ρ is the specific resistivity of the conductor, σ is the specific bulk conductivity, μ_0 is the permeability of free space ($\mu_0 = 4\pi \cdot 10^{-7}$ Vs/Am) and μ_r is the permeability of the conductor [25]. Equation 2.21 shows, that the skin effect becomes increasingly prominent with increasing frequency. At higher frequencies, the skin effect causes an increasing effective resistance of the conductor as the skin depth is smaller and the effective cross section of the conductor is reduced [26].

The skin effect occurs due to circulating eddy currents[1] arising from the changing magnetic field of the alternating current. The eddy currents cancel the current flow in the center of the conductor and reinforce it in the surface area (see figure 2.10). Typical skin depths δ in copper and gold for three different frequencies ω are exemplary shown in table 2.2.

Table 2.2.: Skin depths in gold ($\sigma = 4.6 \cdot 10^7$ S/m, $\mu_r = 1$) and copper ($\sigma = 5.96 \cdot 10^7$ S/m, $\mu_r = 0.999991$) for three exemplary frequencies ω.

ω	Gold	Copper
10 GHz	1.86 µm	1.63 µm
100 GHz	0.59 µm	0.52 µm
1 THz	0.19 µm	0.16 µm

[1] Loops of electrical currents induced in a conductor by a changing magnetic field (Faraday's induction law) are called eddy currents.

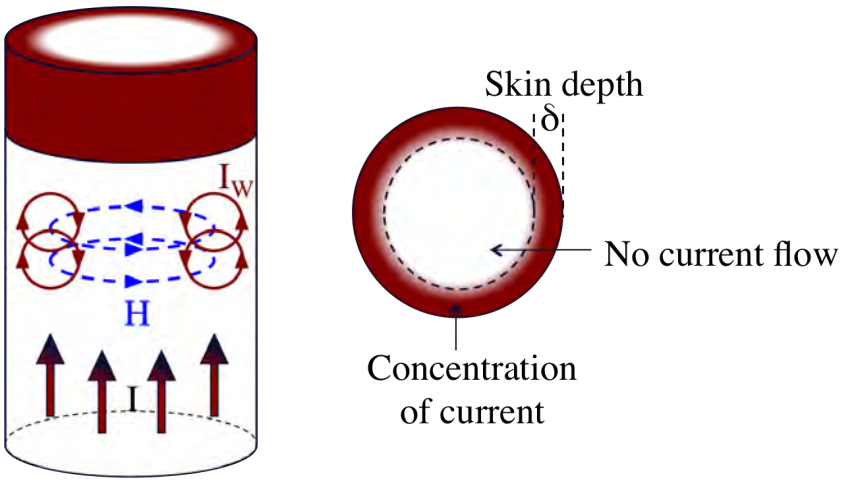

Figure 2.10.: Skin effect in a cylindrical conductor: The current density decreases exponentially from the surface to the center of the conductor for alternating currents. The skin depth δ marks the depth at which the current density is only $1/e$ of the current density at the conductor surface. The effect arises from circulating eddy currents I_W cancelling the current flow I in the center and reinforcing it at the surface.

THz pulses containing a range of frequencies propagating in transmission lines experience an additional dispersion due to the skin effect. Higher frequencies propagate with a higher resistance suffering thereby more from distortion and damping (see equation 2.7 for example).

2.3. Transmission line types

Various geometries can be considered for transmission lines consisting of planar metallic strip conductors sitting on a non-conductive substrate. It is crucial to gain knowledge about their electrical properties as characteristic impedance, effective permittivity, modes of propagation as well as conductor and dielectric losses.

This chapter discusses the design and characterization of the three planar transmission line geometries utilized in the framework of this thesis: Microstrip, stripline and coplanar waveguide. Usually, those transmission lines are used for radio-frequency signals. But some fundamental properties change when higher frequencies such as THz signals are propagating, which is taken into account in the following.

2.3.1. Microstrip

The most popular transmission line type for high-frequency applications due to its technological simplicity is the microstrip. A microstrip consists of a conducting signal strip which is separated from the ground plane by a dielectric layer called substrate. Most of the electric field lines are concentrated in the dielectric substrate, but a fraction

of the field lines also passes though the air or vacuum (see figure 2.11).

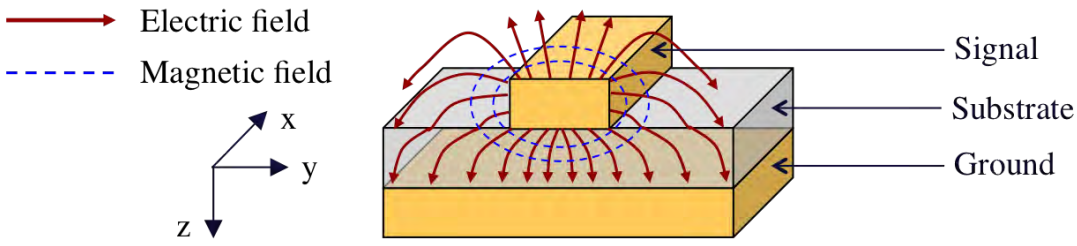

Figure 2.11.: Microstrip geometry with electric and magnetic field lines: A conducting signal strip is separated from the ground plane by a dielectric substrate.

Since the dielectric constant of the substrate is higher than that of the air above, signals are propagating in an inhomogeneous medium. Therefore, the propagation velocity is somewhere between the THz signal velocity in the substrate and the velocity in air. This makes a pure TEM mode propagation impossible, since the electrical field lines are tilted slightly due to the higher propagation velocity in air. The outcome is, that the electrical field has a small component in x direction [27]. This effect is frequency dependent and has to be considered especially for frequencies higher than 10 GHz.

The hybrid TE and TM modes supported by the transmission line are then called quasi-TEM mode. At high frequencies, also higher order modes can propagate (lossy in nature), for example the first higher order mode is a TE mode [20].

In order to describe the quasi-TEM mode propagation, the effective dielectric constant is commonly introduced. This is the dielectric constant of an equivalent homogeneous medium, which exhibits the same phase velocity

$$v_{ph} = \frac{c}{\sqrt{\varepsilon_{eff}}} \tag{2.22}$$

(c is the speed of light in vacuum) as the inhomogeneous medium. The effective dielectric constant ε_{eff} can be approximated by ([28], [29]):

$$\varepsilon_{eff} = \frac{\varepsilon_r + 1}{2} + \frac{\varepsilon_r + 1}{2} \frac{1}{\sqrt{1 + 12h/w}}, \tag{2.23}$$

with ε_r being the dielectric constant of the substrate, h the height of the dielectric substrate and w the width of the conductive signal strip.

Further, the characteristic impedance Z in Ω of a microstrip as proposed by Hammerstad [30] is given by:

$$Z = \begin{cases} \frac{60}{\sqrt{\varepsilon_{eff}}} ln\left(\frac{8h}{w} + \frac{W}{4h}\right) & \frac{w}{h} < 1 \\ \frac{120\pi}{\sqrt{\varepsilon_{eff}}[w/h + 1.393 + 0.667 ln(w/h + 1.444)]} & \frac{w}{h} \geq 1. \end{cases} \tag{2.24}$$

Microstrip transmission lines have a number of disadvantages, for example the line is dispersive. The effective dielectric constant gradually approaches that of the substrate with increasing frequency, as seen in this equation [31]:

$$\varepsilon_{eff,2}(\omega) = \varepsilon_r - \frac{\varepsilon_r - \varepsilon_{eff}}{1 + \sqrt{\frac{Z_0-5}{60}}\left(\frac{\omega}{98.39(Z_0/h)}\right)^2}, \tag{2.25}$$

with substrate height h, implying that most of the energy propagates through the substrate and less through the air at higher frequencies. This phenomenon leads to a gradually decreasing phase velocity [32]. Although the dielectric constant of the substrate gets usually smaller with increasing frequency, this effect even occurs in non-dispersive substrate materials. Additionally, also the characteristic impedance of the transmission line slightly changes with frequency causing dispersion [33].

Besides dispersion, also signal attenuation occurs in microstrips, mainly due to conductor and dielectric losses. Since the microstrip is an open line, radiation losses occur, but using high ε_r materials as well as precise conductor shape and matching, conductor and dielectric losses are predominant [20]. For a propagating quasi-TEM mode, the conductor loss α_c and the dielectric loss α_d are [34]:

$$\alpha_c = \frac{R_s}{Z_0 w}, \quad \alpha_d = \frac{k_0 \varepsilon_r(\varepsilon_{eff}-1)\tan\delta}{2\sqrt{\varepsilon_{eff}(\varepsilon_r-1)}} \tag{2.26}$$

with the wavenumber k_0, microstrip width w, loss tangent $\tan\delta = G'/\omega C'$ [35] and surface resistivity R_s given by $R_s = \sqrt{\pi\mu_r\mu_0 f\rho}$, where μ_r and μ_0 are relative and free space permeability, f is the frequency of operation and ρ is the specific bulk resistivity [36].

The loss tangent usually measures the fraction of the imaginary part over the real part of the complex electrical permittivity. Thereby, the real part refers to the lossy component of an electromagnetic field and the imaginary part to the reactive or lossless imaginary part. If $tan\delta = 0$, there is no dielectric loss.

As seen in equation 2.26, the conductor loss increases with increasing transmission line resistance. In order to construct low-loss lines, strip materials with a high conductivity are prefered, for both signal and ground plane.

With equation 2.26 for the dielectric loss α_d, one finds that

$$\alpha_d \propto \frac{\varepsilon_r(\varepsilon_{eff}-1)}{\sqrt{\varepsilon_{eff}(\varepsilon_r-1)}}. \tag{2.27}$$

Since the effective dielectric constant ε_{eff} is is a linear function of the relative dielectric constant ε_r (see equation 2.23), which can be approximated with

$$\varepsilon_{eff} \cong \varepsilon_r + 1, \tag{2.28}$$

it can be shown that

$$\alpha_d \propto \frac{\varepsilon_r(\varepsilon_r+1-1)}{\sqrt{(\varepsilon_r+1)(\varepsilon_r-1)}} = \frac{\varepsilon_r^2}{\sqrt{\varepsilon_r^2-1}} \overset{\varepsilon_r \gg 1}{\cong} \varepsilon_r. \tag{2.29}$$

So, dielectric losses increase with increasing dielectric constant. In order to minimise dielectric losses, a substrate with a rather low electrical permittivity should be chosen.

Furthermore, also the substrate thickness has an impact on the resulting effective permittivity. Considering finite metal thickness as well as $t/h \leq 0.2$; $0.1 \leq w/h \leq 20$; and $\varepsilon_r \leq 16$, equation 2.25 can be rewritten to [31]:

$$\varepsilon'_{eff} = \varepsilon_{eff} - \frac{\varepsilon_r - 1}{4.6}\frac{t/h}{\sqrt{w/h}}, \tag{2.30}$$

where h is the substrate height, t is the strip height and w is the strip width. Equation 2.30 shows that the effective permittivity decreases with increasing substrate thickness. Thus, thicker dielectric substrates reduce the attenuation in microstrips.

2.3.2. Stripline

Another type of planar transmission lines, which is less dispersive when compared to the microstrip, is the stripline. It can propagate a pure TEM mode. The stripline was first invented by Barrett in the 1950s [37].

The geometric structure and the electric and magnetic field lines for the fundamental TEM mode of a symmetric stripline are shown in figure 2.12.

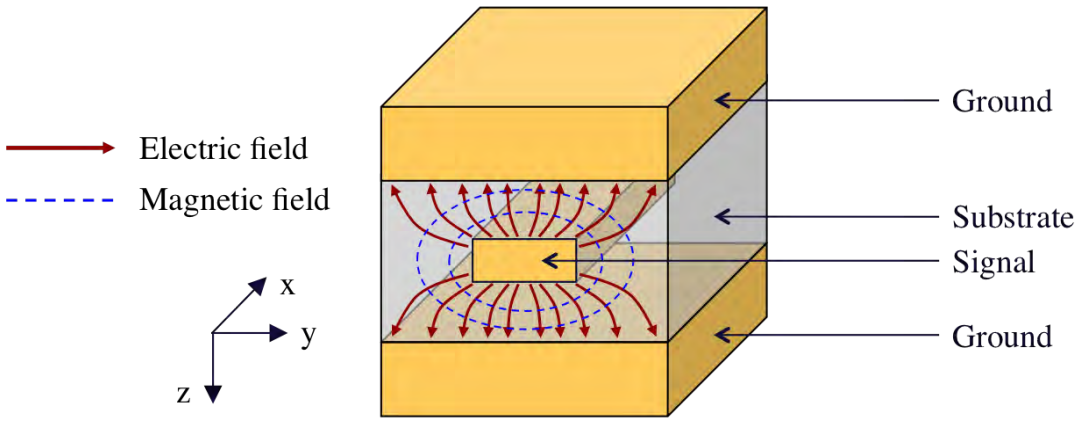

Figure 2.12.: Stripline geometry with electric and magnetic field lines: A conducting signal strip is embedded in a homogeneous dielectric medium enclosed by two parallel ground planes.

Three layers of conductors are required for the stripline construction: The internal signal line is commonly called hot conductor, which is embedded in a homogeneous dielectric with electrical permittivity ε_r. The dielectric medium is a solid material which provides good electromagnetic shielding and low attenuation losses compared

to the microstrip line (and coplanar waveguide) [5]. The other two conductors are the cold or ground conductors, which are connected to signal ground. To prevent propagation of other modes than the fundamental mode, the two ground conductors must be shortened.

Striplines are used in wideband networks and devices because of their non-dispersive behaviour, the high cut-off frequency and their low radiation and attenuation properties. Unfortunately, they present a rather complex geometry, which makes the device fabrication more difficult compared to the microstrip geometry.

A common stripline characteristic is the typically lower wave impedance of the stripline compared to a microstrip. One can easily reach 20 Ω with a stripline which is a value that would cause an immense rise of higher order modes in a microstrip [20].

The characteristic impedance of a symmetric stripline with distance b between the two ground conductors, signal strip height t and strip width w, that fulfill the conditions $w/b < 0.35$ and $t/b < 0.25$ is given by [38]:

$$Z \approx \frac{60}{\sqrt{\varepsilon_r}} ln\left(\frac{4b}{0.67\pi(t+0.8w)}\right). \tag{2.31}$$

Further, the phase velocity of the propagating TEM mode is:

$$v_{ph} = \frac{c}{\sqrt{\varepsilon_r}}. \tag{2.32}$$

Due to the finite conductivity of the stripline conductors as well as the finite resistivity and damping of the dielectric, any stripline exhibits attenuation. In contrast to the microstrip, a stripline is a closed transmission line and radiation losses can be neglected. Attenuation arises from conductor and dielectric losses.

Calculating the conductor loss in a stripline is rather complex as shown by DiPaolo [20]. It is shown that the conductor loss is proportional to the surface resistivity R_s. Therefore, better conductors cause less attenuation. The dielectric losses α_d (in dB per unit length) in a TEM transmission line are given by:

$$\alpha_d = \frac{27.29\sqrt{\varepsilon_r}\tan\delta}{\lambda_0}, \tag{2.33}$$

showing, that dielectric losses become smaller with lower electric permittivities.

2.3.3. Coplanar Waveguide

Coplanar waveguides have been widely used in integrated circuits for microwaves and were invented by Wen in 1969 [39]. They consist of a center conductor separated by a narrow gap from two ground conductors sitting on either side on a dielectric substrate as illustrated in figure 2.13.

In contrast to microstrip and stripline, the electric field lines are strongly coupled

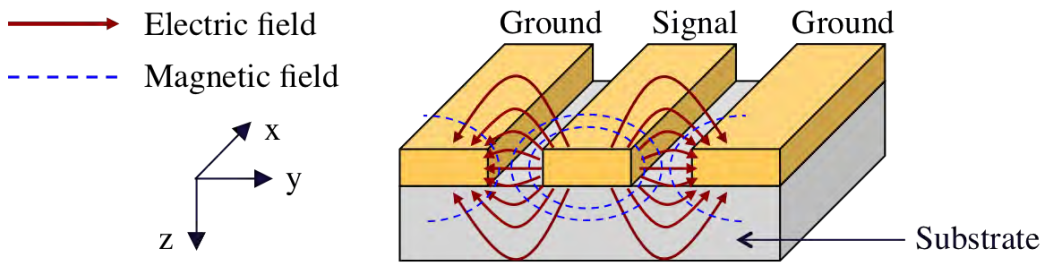

Figure 2.13.: Coplanar waveguide geometry with electric and magnetic field lines: A conducting signal strip is separated by a narrow gap from two ground conductors sitting on either side on a dielectric substrate.

to the ground conductors on both sides, leading to an electrical field confinement in y direction. Microstrip and stripline have an electrical field that is stronger coupled in z direction. Depending on whether horizontal or vertical electric fields are required for the on-chip spectroscopy experiment, one has to chose between either the microstrip or stripline and the coplanar waveguide.

As in the microstrip, the propagation of a true TEM mode is not possible. The electromagnetic wave exists in the dielectric substrate as well as in the air on top. Thus, the wave is travelling in an inhomogeneous medium with

$$\varepsilon_{eff} = \frac{1+\varepsilon_r}{2} \tag{2.34}$$

and a phase velocity of

$$v_{ph} = \frac{c}{\sqrt{\varepsilon_{eff}}}. \tag{2.35}$$

The propagating coplanar mode having non-zero longitudinal components for both the electric and magnetic field is described as a quasi-TEM mode [40]. For the coplanar mode, the electric field is strongly confined to slot gaps, which makes it less dispersive [5].

Besides the coplanar mode (shown in figure 2.13), also the slot line mode exists. The electric field of the slot line mode extends from one ground plane to the other. Usually, a mixed-mode signal is propagating in a coplanar waveguide, consisting of both coplanar mode and slot line mode.

The characteristic impedance Z of a coplanar waveguide is a function of ground line width a, gap width b and effective electric permittivity ε_{eff}. For $1/\sqrt{2} \leq a/b \leq 1$, Z is given by:

$$Z = \frac{30}{\sqrt{\varepsilon_{eff}}} ln\left(2\frac{1+\sqrt{a/b}}{1-\sqrt{a/b}}\right), \tag{2.36}$$

Regarding equation 2.36, the logarithm becomes larger for slot gap widths b being

much bigger than the ground line width a. The characteristic impedance decreases therefor drastically for narrow gap widths.

Coplanar waveguides have a few advantages over other transmission lines. For example, they have more degrees of freedom for device optimization: The signal conductor width as well as the slot gap width can be varied. Further, they require less fabrication steps as a stripline (and the same number of steps as a microstrip), since signal and ground conductors are in the same plane.

Signal attenuation in coplanar waveguides mainly exists due to conductor, dielectric and radiation losses. Dielectric losses α_d in dB/meter are given by [5]:

$$\alpha_d = 8.867 \frac{\tan\delta}{\lambda_0} \frac{\varepsilon_r}{\sqrt{\varepsilon_r}} \frac{\varepsilon_{eff} - 1}{\varepsilon_r - 1}. \tag{2.37}$$

Since ε_{eff} is a linear function of ε_r (see equation 2.34), one can show that α_d is proportional to the square root of ε_r:

$$\alpha_d \propto \frac{\varepsilon_r}{\sqrt{\varepsilon_r}} \frac{\varepsilon_r + 1 - 1}{\varepsilon_r - 1} = \sqrt{\varepsilon_r} \frac{\varepsilon_r}{\varepsilon_r - 1} \overset{\varepsilon_r \gg 1}{\cong} \sqrt{\varepsilon_r}. \tag{2.38}$$

Dielectric losses can therefore be minimized by using a substrate with low dielectric permittivity.

Conductor losses α_c arise by the finite conductivity, the skin effect as well as substrate roughness of the conductive material and increase with decreasing gap dimensions [5].

Radiation losses α_r occur due to the interference of the dominant propagation mode with higher order modes at higher frequencies (this is one reason for dispersion in coplanar waveguides) as well as due to leakage into the substrate. Leakage happens when the phase velocity of the dominant mode is higher than the substrate mode [41], [42]. Radiation losses and dispersion can be minimized by fabricating coplanar waveguides with small slot gap widths [5]. However, this would cause increasing conductive losses. Thus, a compromise in slot gap width has to be found to keep both, radiation losses, dispersion and conductive losses low.

3. Development of low-dispersive single-mode transmission lines

This chapter is dedicated to the experimental development of planar transmission lines for low-dispersive, single-mode signal propagation in on-chip THz experiments.

In experiments by McIver *et al.* [8], THz signals suffered from dispersion and damping. To reconstruct the undistorted signal, an elaborate analysis was required. In these experiments, THz circuitry was fabricated on doped silicon substrates with a 285 nm silicon dioxide (SiO_2) layer. Instead of using a metal ground plane, the doped silicon acts as a ground plane for the so formed microstrip geometry. Due to the low conductivity of the doped silicon, signals propagating in the transmission line disperse strongly. This geometry is referred to as a doped silicon microstrip in the following.

In order to reduce dispersion and damping, a number of different transmission line geometries, dimensions, and materials are investigated. For example, the microstrip can be improved by a more symmetric stripline design, the thickness of the dielectric can be adjusted, and the doped silicon ground plane can be replaced by a more conductive gold layer. All of these approaches are tested and discussed in the following.

The chapter is divided into two main sections: The first section describes the fabrication of transmission lines, including the design of THz circuits (3.1), the fundamentals of THz circuit fabrication (3.2) and different concepts to grow SiO_2 for striplines (3.3). Further, the fabricated devices are presented (3.4). In the second section the experimental pump-probe setup (3.5) and the pump-probe measurements are shown (3.6).

3.1. THz circuit design

THz circuits are designed using the software KLayout [43]. Four different circuits are fabricated on every substrate with distances of 100 µm, 200 µm, 300 µm and 400 µm between the photoconductive switches for pulse propagation characterization (see figure 3.1).

Every single evaporation step is drawn in one layer. The first layer includes the shapes for the photoconductive switches (18 x 20 µm) as well as the markers for the mask alignment for further layers. The second layer contains the transmission line structures with bond pads for wire bonding. The main transmission lines have a width of 10 µm. The rounded transmission lines contacting the photoconductive switches have widths of 20 µm and are smoothly bent to avoid reflections. These contacts are used to apply bias voltages for signal generation and to measure photocurrents during signal detection.

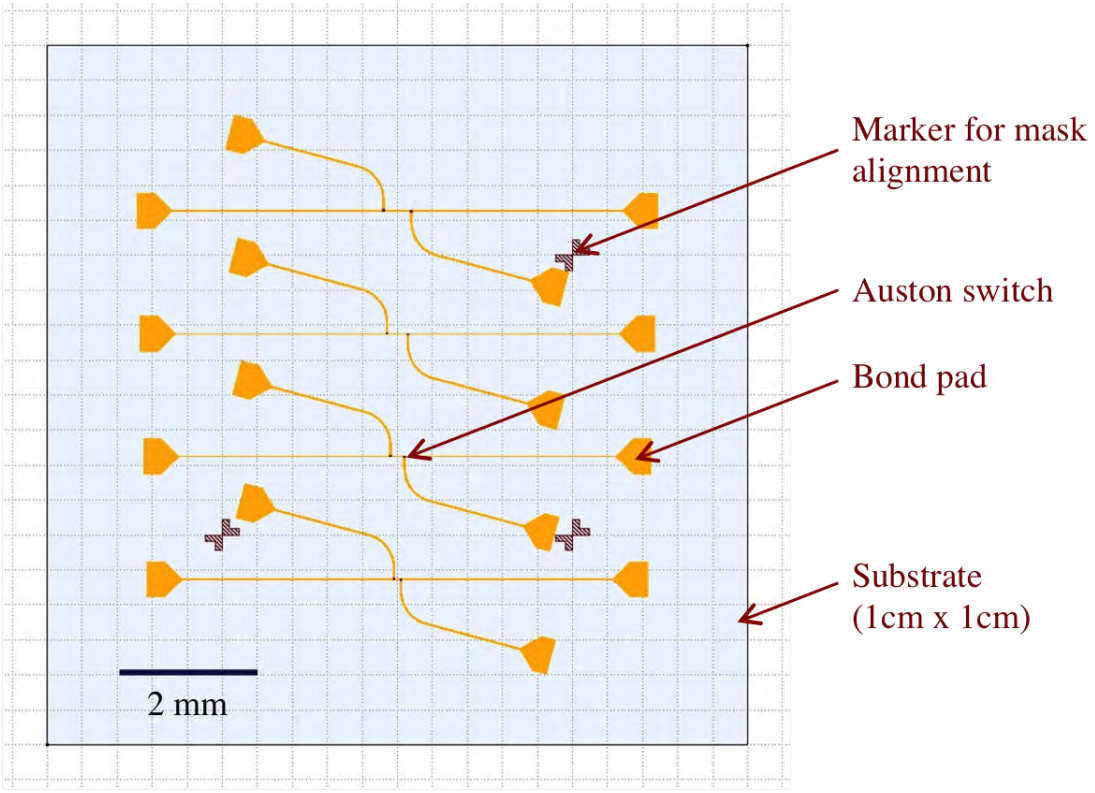

Figure 3.1.: THz circuit design in KLayout with two layers for a 1 cm x 1cm substrate: In a first layer, photoconductive switches and markers for mask alignment are drawn. Transmission line structures with bond pads are designed in a second layer.

The designed circuits are transferred to a direct laser writing lithography system from Heidelberg Instruments (uPG100) and are written in a thin layer of photo resist as explained in the following.

3.2. Fundamentals of THz circuit fabrication

Ultrafast THz circuits are fabricated using optical lithography, thermal evaporation and lift-off processing. They are fabricated in two steps as designed in KLayout: Firstly, amorphous silicon (α-silicon) patches are thermally evaporated, which form the two photoconductive switches. Secondly, metallic structures (Ti/Au) are constructed by thermal evaporation to create transmission lines. A schematic cross-section of such a microstrip geometry is shown in figure 3.2.

For all lithography steps the same procedure depicted in figure 3.3 is used: Firstly a two-layer photo resist system is spin coated on a substrate. The bottom layer is a heat-resistant undercut layer of MicroChem LOR-7B. For the spin coating process, a few drops of resist are placed onto the center of the substrate surface. Then the substrate is spun at high rotation speeds (4500 rpm, acceleration of 2000 rpm/s, 45 sec) to obtain a

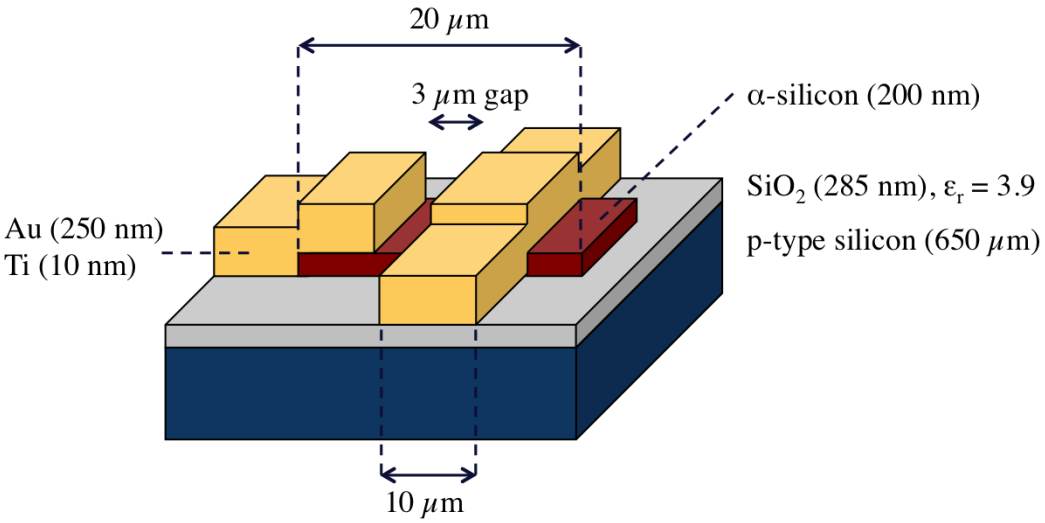

Figure 3.2.: Schematic cross-section of a microstrip geometry at the photoconductive switch position.

homogeneous thin layer of resist (∼ 500 nm). After spin-coating, the LOR-7B-layer is cured for 4 min at 180°C.

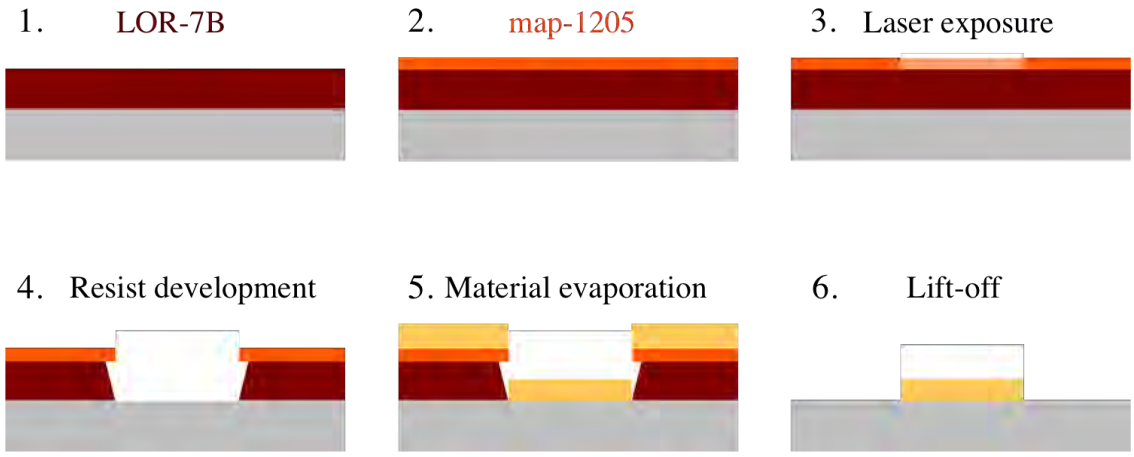

Figure 3.3.: Fabrication of THz circuits in six steps: 1. *LOR-7B* is spin-coated and prebaked on a substrate. 2. Positive photoresist *map-1205* is spin-coated and prebaked. 3. The photoresist is exposed by an optical lithography system. 4. Resist and *LOR-7B* are developed, creating a bi-layer sidewall with an undercut profile. 5. Material is thermally evaporated. 6. Lift-off of bilayer resist which leaves only the desired structure.

A second layer of positive photoresist *micro resist map-1205* is spin-coated with 2000 rpm for 30 s with an acceleration of 2000 rpm/s and heated for 30 s at 100°C. Then, the structures are written in the bilayer photoresist system with a direct-write optical lithography system, where a laser beam only modifies the top photo resist layer (see step three in figure 3.3). Subsequently, the structures are developed using $ma-D331/S$. The developer dissolves the exposed photo resist and the LOR layer underneath. The LOR

will form an undercut as depicted in step three of figure 3.3, which is indispensable for a clean lift-off after material deposition.

The sample is mounted upside down in a thermal evaporation chamber and the material is deposited onto the substrate. In a last step, the photoresist is removed in a bath of $mr-rem700$ remover heated at 50 °C, leaving only the desired structures.

3.3. Methods to deposit high-quality SiO_2 for striplines

As discussed before, doped silicon microstrip transmission lines were used in former on-chip THz experiments to guide THz signals, which suffered from dispersion. The idea is therefore, to construct different transmission line geometries such as striplines to improve the pulse propagation. Striplines can be fabricated out of doped silicon microstrips by covering the signal lines with a dielectric layer such as SiO_2 followed by a second ground layer made of gold (compare figures 2.11 and 2.12).

However, the fabrication of this dielectric SiO_2 layer is not trivial. Different concepts to grow high quality SiO_2 are possible such as spin-coating of HSQ, sputtering as well as thermal evaporation of SiO_2, all of which are tested in the following.

3.3.1. Spin-coating of HSQ

A first approach to deposit SiO_2 films on doped silicon microstrip structures is to use hydrogen silsesquioxane (HSQ). HSQ has the property that it turns itself into a SiO_2-containing material after curing at high temperatures, with a relative permittivity $\varepsilon_{r,HSQ} = 2.9...3.2$ smaller than the permittivity of pure SiO_2 ($\varepsilon_{r,SiO_2} = 3.9$). It is widely used to deposit high quality insulating films for electronic devices such as integrated circuits [45][46].

The precursor of HSQ, FOX-15 (18 % solid content in solvent methyl isobutyl ketone (MIBK)), was purchased from Dow Corning. By changing the amount of MIBK solvent in the HSQ solution, the film-thickness can be varied. In order to construct a symmetric stripline with doped silicon wafers (285 nm dry SiO_2), a film thickness of 285 nm is desirable. Differently diluted FOX-15 solutions are spin-coated on a 1 cm x 1 cm doped Si wafer with 4000 rpm for 60 s with an acceleration of 2000 rpm/s. Measuring the film thicknesses with an atomic force microscope (AFM) reveals that a FOX-15 concentration of 75 % in MIBK provides a film thickness of 285 nm (see figure 3.4).

The analysis of structural changes of HSQ during the curing process has been studied by Loboda *et al.* [46] and Belot *et al.* [47] amongst others. They report that there are four possible stages in the HSQ curing process depending on the curing temperature. For temperatures from room temperature up to 200°C, only solvent loss was observed. For temperatures between 250 and 350°C, the cage-network structure is redistributed and a SiO_2-containing material arises:

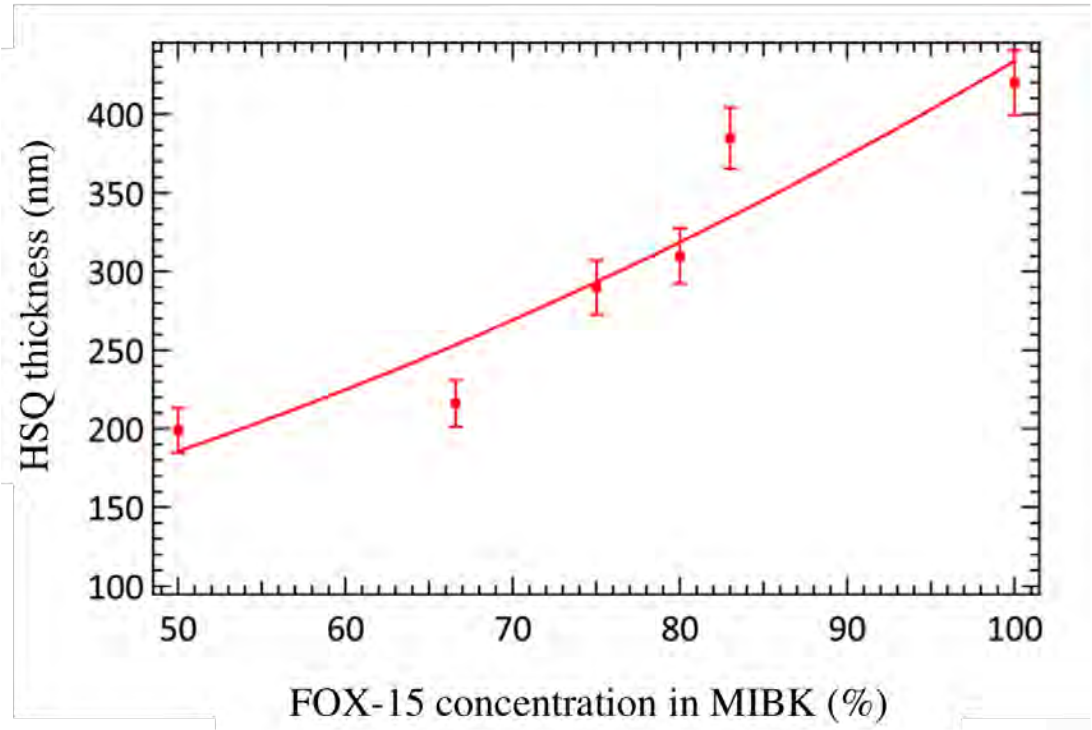

Figure 3.4.: Measured thickness of spin-coated HSQ as function of FOX-15 concentration in MIBK. A concentration of 75 % provides a film thickness of 285 nm.

$$2HSiO_{3/2} \rightarrow H_2SiO_{2/2} + SiO_{4/2} \tag{3.1}$$

$$H_2SiO_{2/2} + HSiO_{3/2} \rightarrow SiO_{4/2} + H_3SiO_{1/2} \tag{3.2}$$

$$H_3SiO_{1/2} + HSiO_{3/2} \rightarrow SiO_{4/2} + SiH_4. \tag{3.3}$$

When the temperature is further increased, thermal dissociation of Si-H followed by a collapse of the pore structure is reported [48].

To deposit SiO_2 layers on doped silicon microstrip structures, HSQ (75 % FOX-15 in MIBK) is spin-coated with 3000 rpm for 30 s. To cure the HSQ on the microstrip structure, the sample is heated to 160° C for 5 min to lose the solvent and afterwards to 300° C for 30 min to redistribute HSQ into the SiO_2 containing material.

The HSQ coated microstrip structure (see figure 3.5 (a)) is then mounted on a sample holder and wire bonded for photoconductive switch resistance measurements. The bond pads have to be scratched for wire bonding, since the HSQ covers the entire circuit including bond pads and switches. The measured switch resistance is 80 Ω, which is three orders of magnitudes lower than the switch resistance former experiments. The microscopic picture of the switches shown in figure 3.5 (b) indicates, that the thermal curing process of the HSQ (see Eqs. 3.1 to 3.3) destroys the switches.

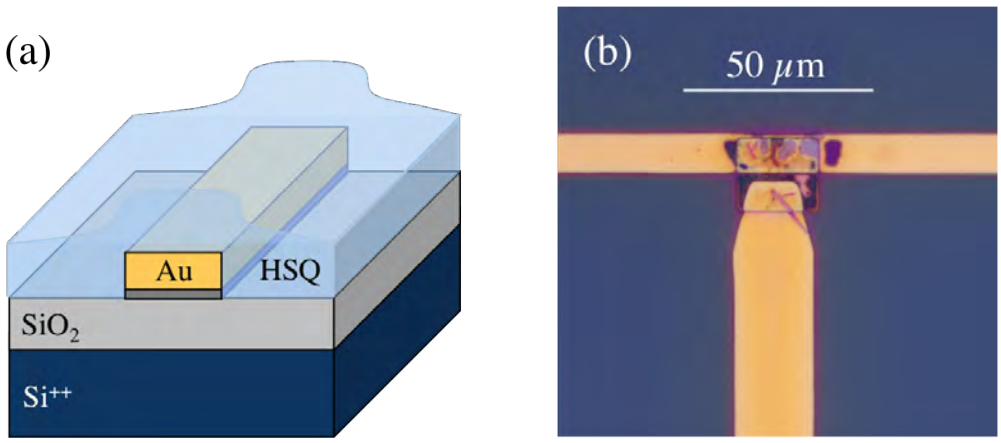

Figure 3.5.: First approach to deposit SiO_2: a) Hydrogen silsesquioxane (HSQ) is spin-coated on a microstrip structure. In order to turn HSQ into a SiO_2-containing material, the sample is heated to 170° C for 5 min and afterwards to 300° C for 30 min. b) The thermal curing process of the HSQ transformed the Auston-switches, which resulted in a measured Auston-switch resistance of only 80 Ω at room temperature.

Since it is not possible to protect the photoconductive switches from the HSQ solution in the spin-coating process, another approach has to be found in order to grow SiO_2 for stripline development.

3.3.2. Sputtering of SiO_2

SiO_2 thin films can also be deposited by radio frequency (RF) magnetron sputtering. In RF magnetron sputtering, Argon ions are accelerated by a RF electric field and hit an electrode consisting of the deposition material. The target material is sputtered radially in all directions and a thin film of the sputter material is grown on the substrate.

The substrate is a 1 cm x 1 cm doped silicon wafer with thermally evaporated photoconductive switches and transmission lines. Prior to deposition, the chamber is pumped to 7×10^{-7} mbar. Sputtering of 285 nm SiO_2 is performed with an Ar pressure of 1×10^{-2} mbar and with a low RF power of 30 W.

The sputtered SiO_2 covers the entire structure including photoconductive switches and transmission lines. In contrast to the HSQ film deposition, the photoconductive switches are not transformed by a chemical reaction. Also, using photolithographic methods, it would be possible to construct a mask that protects the photoconductive switches from sputtered SiO_2. Nevertheless, the disadvantage of sputtering is, that the roughness of the sputtered SiO_2 is ~ 3 nm (see figure 3.6).

In the process of fabricating striplines, there is at least one more evaporation step for the upper Au layer required. Therefore a flat, homogenous SiO_2 film with a lower roughness is preferable. One promising technique for growing ultra-flat films in general is thermal evaporation.

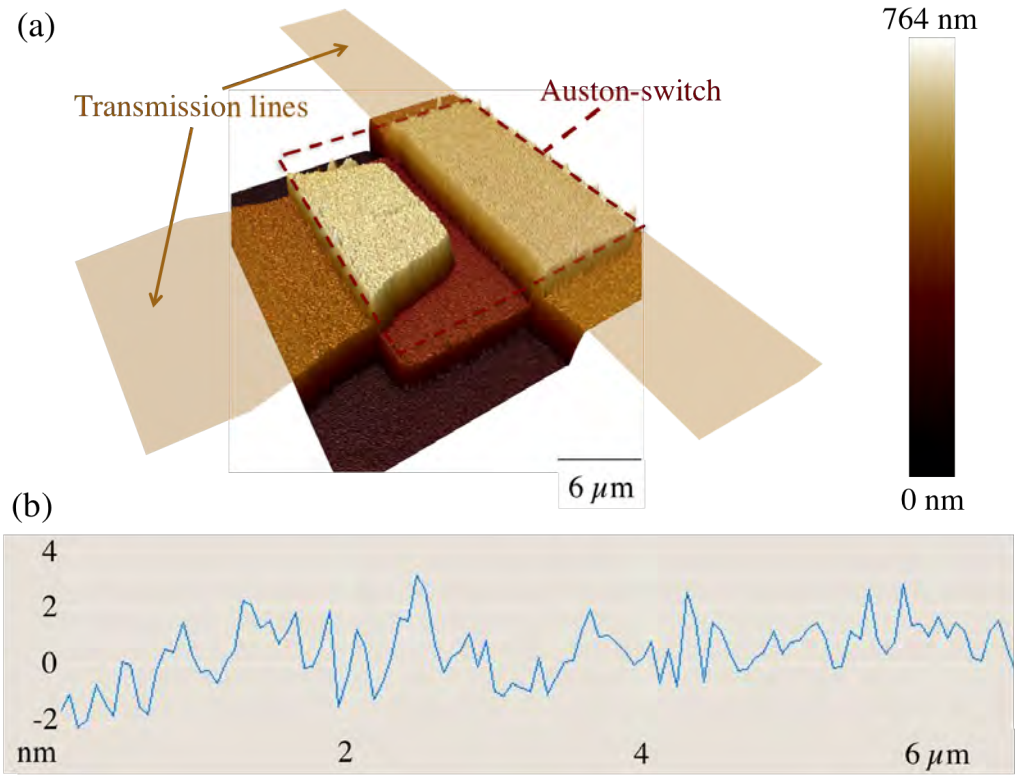

Figure 3.6.: (a) AFM picture of 285 nm sputtered SiO_2 on top of an evaporated photoconductive switch and evaporated transmission lines. (b) The SiO_2 roughness was measured to be ~ 3 nm.

3.3.3. Thermal evaporation of SiO_2

Since spin-coating and heating of HSQ damages the photoconductive switches and sputtering does not provide a smooth SiO_2 film, another approach is required to grow high-quality dielectrics for stripline fabrication. A common technique is thermal evaporation. This method includes the simple process of emission of the heated source material which then condenses on the cold substrate. The source material is stored in a crucible and is evaporated by an electron beam in high vacuum ($< 10^{-7}$ mbar). The deposition rate is determined by the vapor pressure of the evaporating material at the evaporation temperature. Also, the main advantage of electron-gun heating is that contamination by the crucible can be avoided [49].

The evaporator which is used to evaporate silicon, titanium and gold for the microstrip structures, has never been used to deposit SiO_2 before. Thus, SiO_2 evaporation is tested step by step adjusting the deposition rate and sweep diameter of the electron beam on the source material. Since SiO_2 has a low thermal conductivity of $\sim 1.4 W/m \cdot K$ (for comparison: gold has a thermal conductivity of 314 $W/m \cdot K$), the sweep diameter as well as the deposition rate is kept low to deposit smooth films in high vacuum of less than $1 \cdot 10^{-7}$ mbar. A deposition rate of 1.5 Å/s yields the best SiO_2 quality.

Thermally evaporated SiO_2 films have the advantages that the roughness is lower

than the roughness of sputtered SiO_2 and the dielectric can be shaped using standard photoresist and lift-off techniques. However, a problem is that pinholes occur, which limits the break-through voltage of the dielectric (see figure 3.7).

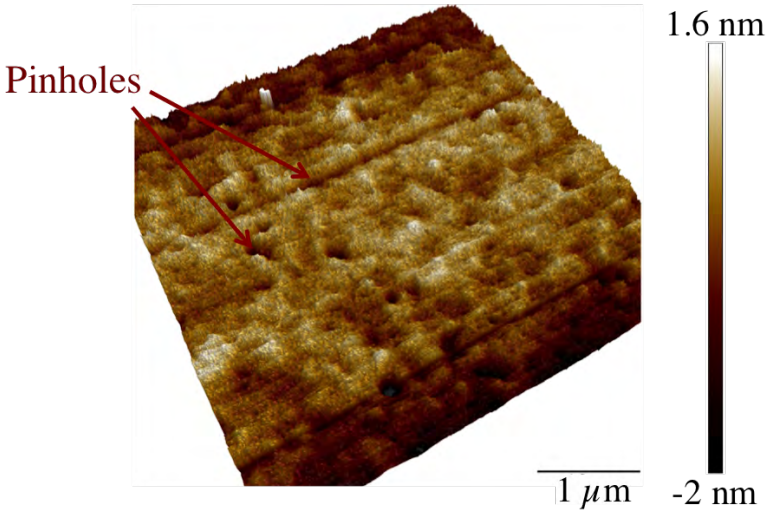

Figure 3.7.: Thermally evaporated SiO_2 (285nm) on a doped silicon substrate: The roughness is 1 nm, but pinholes limit the break-down strength of the dielectric.

Pinholes can be avoided by heating the substrate to high temperatures above 300°C during the thermal evaporation of SiO_2. Therefore, a heating stage is required in the vacuum chamber of the evaporator shown in figure 3.8 (a). The evaporator is not equipped with a heating stage and the installation provides some challenges: Firstly, the heating plate has to be shaped in such a way, that it fits in the circular sample mount holder of the evaporator. Secondly, samples are mounted upside down. Thus, the heating stage has to provide a sample holder for 1 cm x 1 cm substrates. Thirdly, the heater has to be mounted in vacuum with electrical feedthroughs to the outside. Further, the evaporator provides a rotary drive function with which the mounted sample can be rotated and evaporation is performed from different angles. Since the rotation is sometimes useful, the heating stage cannot be connected with fixed cables, but plugs are required to disconnect the heating stage in case the rotary drive is used. And last but not least, the vacuum chamber provides an inner detachable shielding (13 separate peaces) which protects the vacuum chamber from material deposition. All of the peaces have to be exchanged for extra protection of the heating stage connection and simplified mounting for cleaning.

The heater is designed and installed in the framework of this thesis (see figure 3.8), but will only be finished afterwards. Therefore, the samples are fabricated without heating during evaporation.

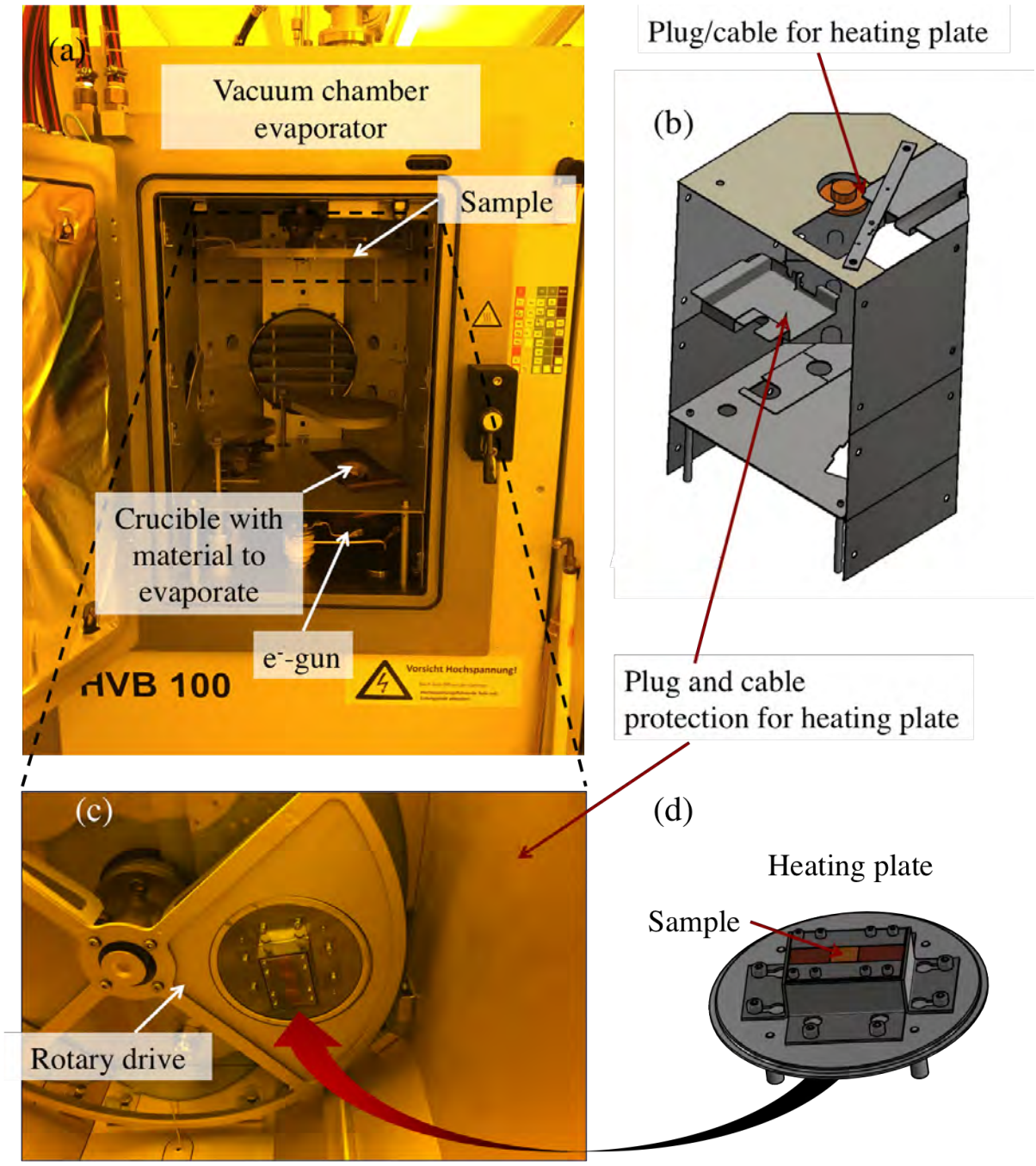

Figure 3.8.: Device for thermal evaporation with implemented heating plate for sample heating during evaporation: (a) A crucible filled with the desired evaporation material is placed in the vacuum chamber of the evaporator and heated by an electron-gun. The sample is mounted upside down in the rotary drive. (b) Technical drawing of the modified vacuum chamber shielding, plug/ cable inlet as well as protection for the heating plate. (c) The rotary drive is switched off, when the heating stage is activated and can only be turned on when the heating plate is not connected. (d) Heating stage mounted on the circular holder for the rotary drive with the sample holder for three 1 cm x 1 cm substrates. The heating system has been realized by Michael Volkmann with help of Boris Fiedler.

After thermal evaporation of SiO_2 it was sometimes observed that the material in the crucible changed its color from transparent to brown. This is an indication for the formation of SiO, silicon monoxide. SiO_2 can turn into SiO when reacting with silicon, carbon or hydrogen [50], especially at higher temperatures. Achieving higher vacuum before SiO_2 evaporation ($< 10^{-8}$ mbar) is one approach to avoid SiO formation. Another method is to insert pure oxygen in the high vacuum. Since SiO oxidizes rapidly to SiO_2, no SiO will be deposited on the substrate. The evaporator already provides a gas inlet, thus, oxygen insertion can be realized.

3.4. Fabrication of low-dispersive transmission lines

In the framework of this thesis five different devices are fabricated and measured to implement a low-dispersive, single-mode transmission line for on-chip THz spectroscopy. Every sample is measured before the next sample is fabricated. This chapter presents the sample fabrication. The results are discussed in later chapters.

The first sample is a **doped silicon microstrip**, similar to the one used in former on-chip THz experiments. As shown in figure 3.9, the microstrip structure is constructed in two steps of thermal evaporation. Firstly, 200 nm of silicon is deposited to form the photoconductive switches. Then, 10 nm of titanium and 250 nm of gold are evaporated for the transmission lines. The titanium serves as an adhesion promoter between the gold and the smooth SiO_2 surface of the silicon wafer.

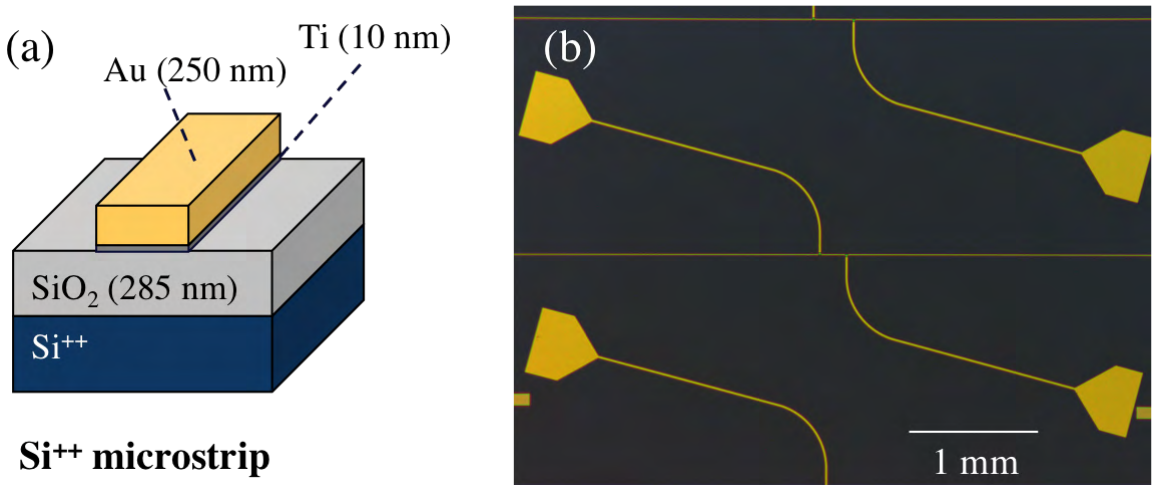

Figure 3.9.: (a) **Si^{++} microstrip**: Transmission line structure in two evaporation steps. Firstly, 200 nm silicon in shape of patches for the photoconductive switches is evaporated on a clean doped silicon wafer with a 285 nm thick dry oxide layer. Secondly, 10 nm titanium and 250 nm gold are evaporated for the microstrip structure. (b) Microscope picture of the fabricated doped silicon microstrip.

To improve the THz signal propagation, the doped silicon microstrip is modified to

a **simplified stripline**. Figure 3.10 shows the simplified stripline. The doped silicon acts as the lower ground line and a gold layer forms the top ground line. As discussed in chapter 2.3.2, striplines are less dispersive compared to a microstrip. The disadvantage is, that more fabrication steps are required. Therefore, this simplified stripline is fabricated as a first approach. Simplified, because the upper ground line is not plane and the distance from the signal line to the upper and lower ground lines are different (compare figure 3.10 (a) and figure 3.11).

The simplified stripline is fabricated in four evaporation steps. The first two steps are the same as those for the doped silicon microstrip. In a third step, 285 nm SiO_2 is evaporated on the entire substrate. 285 nm are chosen to ensure that no short between the signal line and the upper ground line occurs and to keep the dielectric thicknesses underneath and on top of the signal line equal. In a last step, 250 nm gold is deposited onto the sample. In this step, a resist mask is used to open windows in the gold film, so that the switches can be triggered by laser light and the bond pads can be contacted via wire bonds.

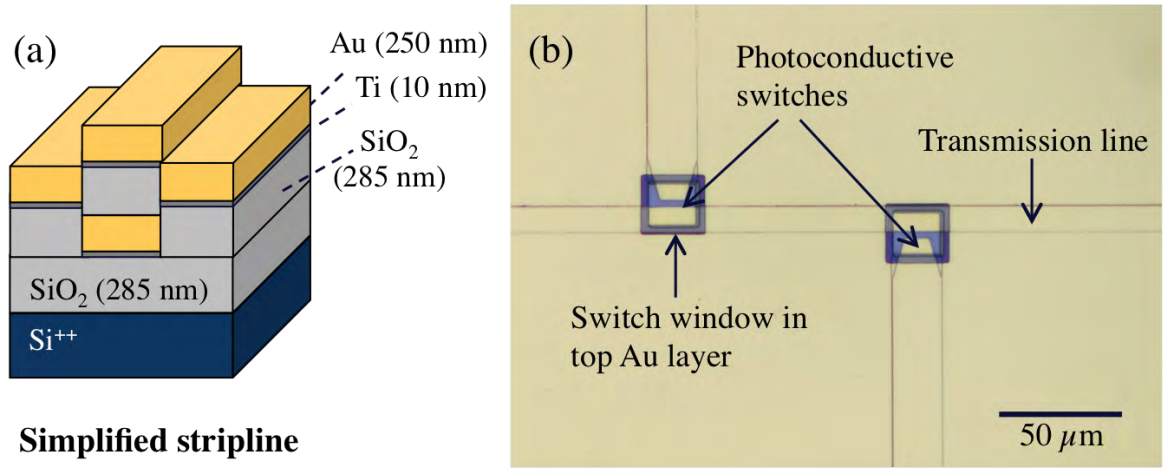

Figure 3.10.: **Simplified Stripline** (a) Firstly, the microstrip structure as shown in figure 3.9 is evaporated. Subsequently, 285 nm of SiO_2 is evaporated. In a last evaporation step, 250 nm of gold is deposited on the whole sample, but not on the switches and not on the bond pads (see figure (b)).

As a third sample, a **stripline** is fabricated in four evaporation steps as shown in figure 3.11. In the first two steps, the doped silicon microstrip structure is fabricated. Then, a lithography step is used to evaporate 270 nm of SiO_2 in broad strips around, but not on top of the transmission lines and photoconductive switches. Thereby, the SiO_2 and the signal line (10 nm Ti + 250 nm Au + 10 nm Ti) have equal heights and form a plane. In a fourth step, a resist mask is used to evaporate 285 nm of SiO_2 as well as 10 nm Ti and 250 nm Au on the transmission lines as well as on the previously deposited broad SiO_2 strips. The resist mask is also used to open windows in the top SiO_2 /Au layer to allow access to the photoconductive switches.

When SiO_2 is deposited on the sample without heating the sample to high temperatures (250 - 350°C), pinholes can occur. Thereby, currents can tunnel from the signal line through the evaporated SiO_2 layer in the upper Au ground line. Thus, currents can bypass the photoconductive switch and the generation as well as detection of currents is only possible for low bias voltages or in the worst case becomes impossible.

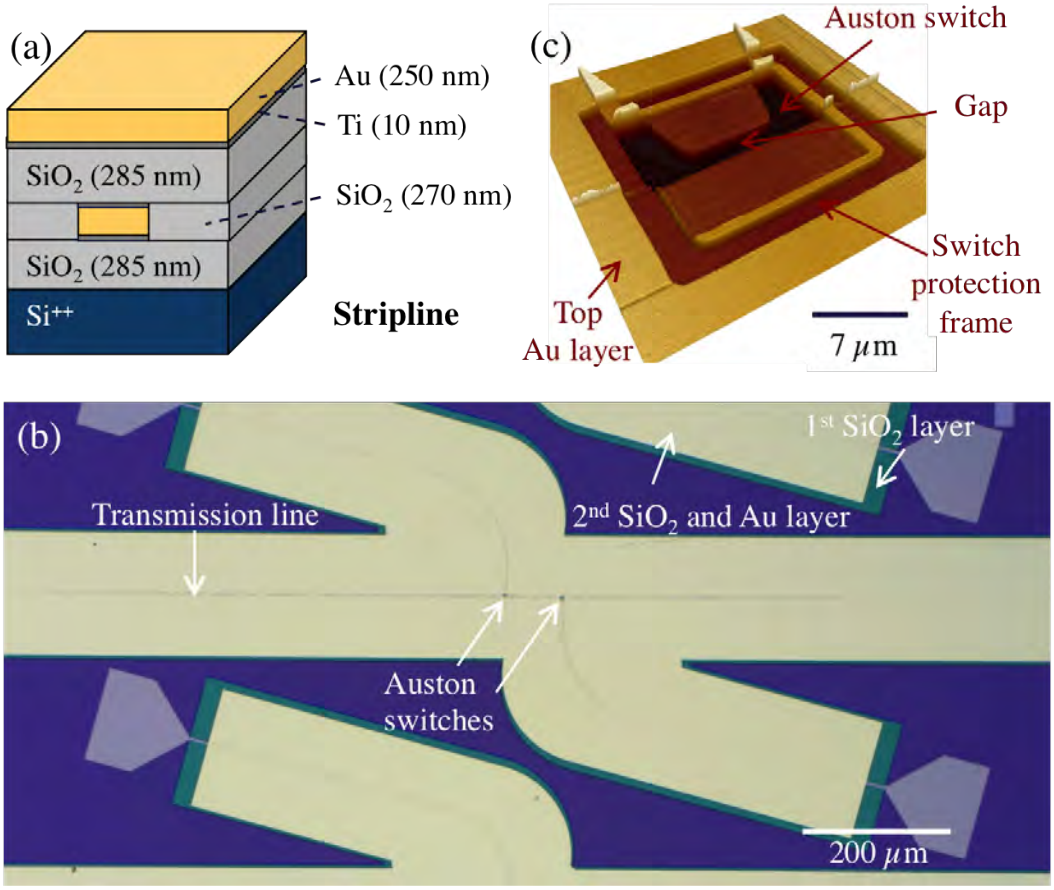

Figure 3.11.: **Stripline** (a) Cross section of the stripline structure: 270 nm of SiO_2 is evaporated in broad strips around but not on top of the transmission lines to form a plane with the gold signal line. Then, 285 nm of SiO_2, 10 nm Ti and 250 nm Au are evaporated on the transmission lines as well as on the previously deposited SiO_2. (b) Microscope picture of the sample. (c) AFM picture of a photoconductive switch. A resist mask is used to open windows in the top SiO_2/ Au layer to allow access to the switches.

The implementation of the sample heater in the evaporator is laborious as explained in chapter 3.3.3 and is performed in parallel to the sample fabrication and measurement. To bypass the pinhole problem without sample heating, another sample is designed. This fourth sample, the **stripline with stripline islands**, has SiO_2 as well as ground line islands with floating potentials, which are not connected to each other (see figure 3.12). Thereby, DC voltages across the switch will not lead to a current through the top SiO_2/ Au layer. The sample with stripline islands is fabricated similarly to the stripline sample, only using different resist masks to construct the islands.

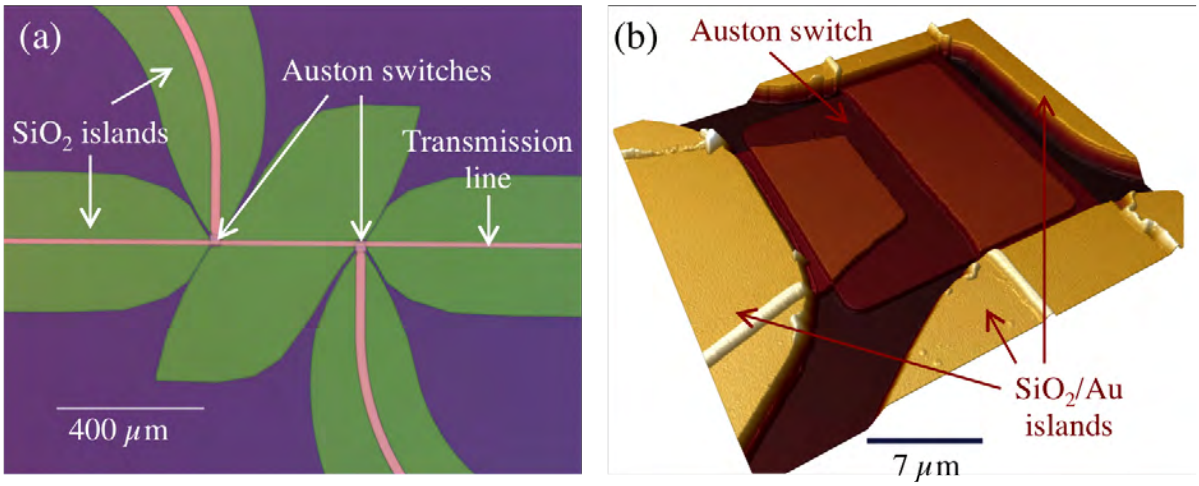

Figure 3.12.: **Stripline with stripline islands**: The sample is fabricated similarly to the stripline sample, only using different resist masks to construct the islands. Thereby, tunnelling of currents through pinholes in the evaporated SiO_2 can be prevented. (a) Microscope picture of the sample with evaporated SiO_2 islands. (b) AFM picture of a photoconductive switch.

The striplines have symmetric geometries around the signal line, but the ground lines are composed of materials with vastly different conductivities: Doped silicon ($3{\cdot}10^4$ S/m) and gold ($4.6 \cdot 10^7$ S/m). Therefore, not only the transmission line geometry by itself influences the signal propagation, but also the conductivity of the material used for the ground lines. Since gold wafers with an oxide layer are not as easily accessible as doped silicon wafers, gold substrates are fabricated. Constructing and measuring **gold microstrips** will provide new insights into the effect that the material of the conductive ground has to pulse propagation in transmission lines.

A first step to produce gold/SiO_2 substrates is to fabricate a flat gold surface. When gold is evaporated without heating, the roughness amounts to 1.8 nm. Compared to silicon substrates with roughnesses smaller than 0.1 nm, this value is too high. Alloys can be used to evaporate flatter metal films. For a comparison with the gold film, a gold germanium layer is evaporated. The roughness of the gold germanium film is measured to be 0.9 nm, which is an improvement, but not flat enough to grow high-quality substrates. In addition, gold germanium has a lower conductivity than gold.

As shown by Wagner *et al.* [51], ultra-flat gold surfaces can be fabricated with the method of template stripping. A thin film of gold (250 nm) is evaporated with 0.5 Å/s on a clean 6" silicon wafer. Then, properly cleaned small silicon wafers (1 cm x 1 cm) are glued upside down on the evaporated gold (see figure 3.13 (a)).

Several different glues such as HSQ, stycast 2850 FT and epoxy glue (epo-tek 353 ND) are tested with different curing procedures. Only the epoxy glue allowed template stripping without gold film distortion.

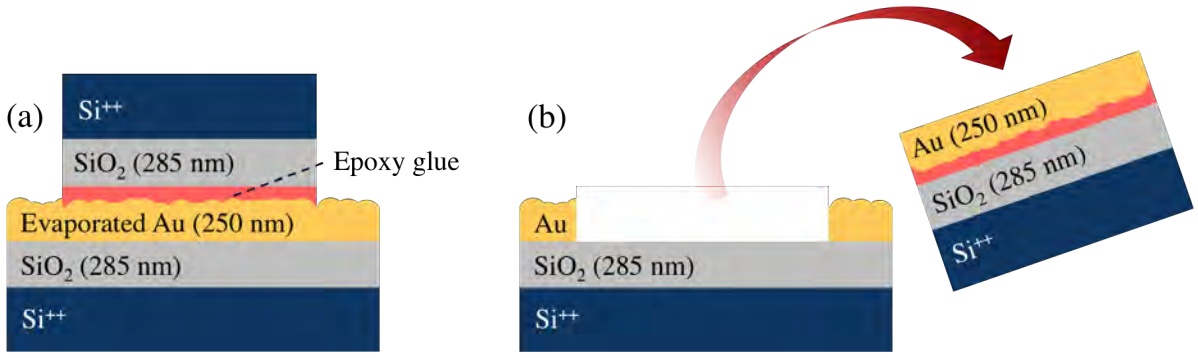

Figure 3.13.: Template stripping for ultra-flat gold surface fabrication. (a) A 6″ wafer is evaporated with 250 nm gold. Then, a small silicon wafer (1 cm x 1 cm) is glued upside down on the gold surface with epoxy glue. (b) After curing at temperatures up to 320 °C, the wafers can be stripped using a tape.

The epoxy glue is a two-component glue with low viscosity that can deal with temperatures up to 350°C. To avoid micro air bubble formation in the glue between the small silicon wafers and the gold film, the mixed glue is put in a vacuum chamber for 30 min. Meanwhile, the 6″ wafer with the gold film is placed on a 70°C hotplate to vaporize residual molecules from the gold surface. Additionally, the glue viscosity is lower when heated up. Small drops of the glue are then placed on the gold film wafer and the small silicon wafers are placed upside down on the drops and pressed down.

For curing, the hotplate temperature is slowly increased to 320°C in the time frame of 4 hours. After cooling the wafer down, the small silicon wafers are stripped off from the 6″ wafer with help of a tape (see figure 3.13 (b)). Thereby, 1 cm x 1 cm substrates with a gold surface with a roughness of 0.3 nm are fabricated (see figure 3.14 (a)).

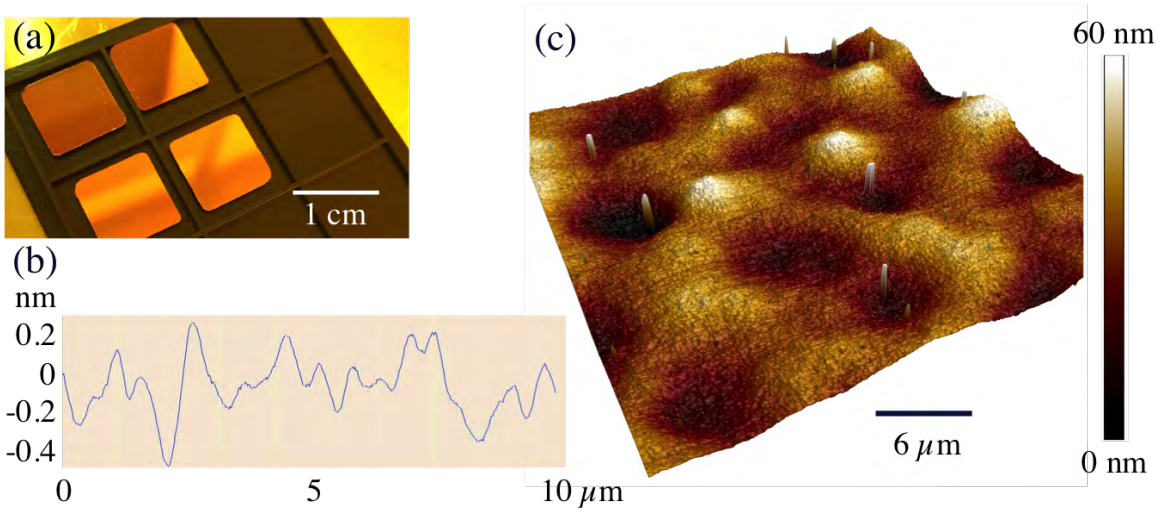

Figure 3.14.: (a) Template stripped gold wafers. (b) The roughness of gold before heating is 0.3 Å. (c) After heating the gold templates for two hours at 310°C, bubbles have formed.

To grow high-quality SiO_2 via thermal evaporation, the substrates need to be heated to temperatures of 250 - 350°C for several hours before and during the evaporation. In order to test wether the fabricated gold templates can deal with such temperatures without being protected by the silicon wafer, the templates are heated up to 310°C for several hours. A surface measurement with an AFM reveals that during the unprotected heating large bubbles are formed (see figure 3.14 (b)). Therefore, template stripped gold wafers cannot be used to grow high-quality gold/ SiO_2 substrates.

As a first approach to fabricate a gold microstrip without heating the substrate during evaporation, 10 nm titanium, 250 nm gold, 10 nm titanium and 600 nm SiO_2 are evaporated on a doped silicon substrate at a pressure of $7 \cdot 10^{-8}$ mbar. Titanium is required to promote adhesion between the gold and oxide layers. The increased SiO_2 thickness is chosen to reduce attenuation and to improve the signal propagation compared to the doped silicon microstrip with a SiO_2 thickness of 285 nm as discussed in chapter 2.3.1.

Photoconductive switches as well as transmission lines are evaporated on the gold/ SiO_2 substrate, as described before. Since the fragile SiO_2 layer is deposited on a soft gold layer, wire bonding will punch through the oxide and short the signal and ground line. Therefore, the sample has to be contacted manually using uncoated gold wires and silver conductive paste (see figure 3.15)

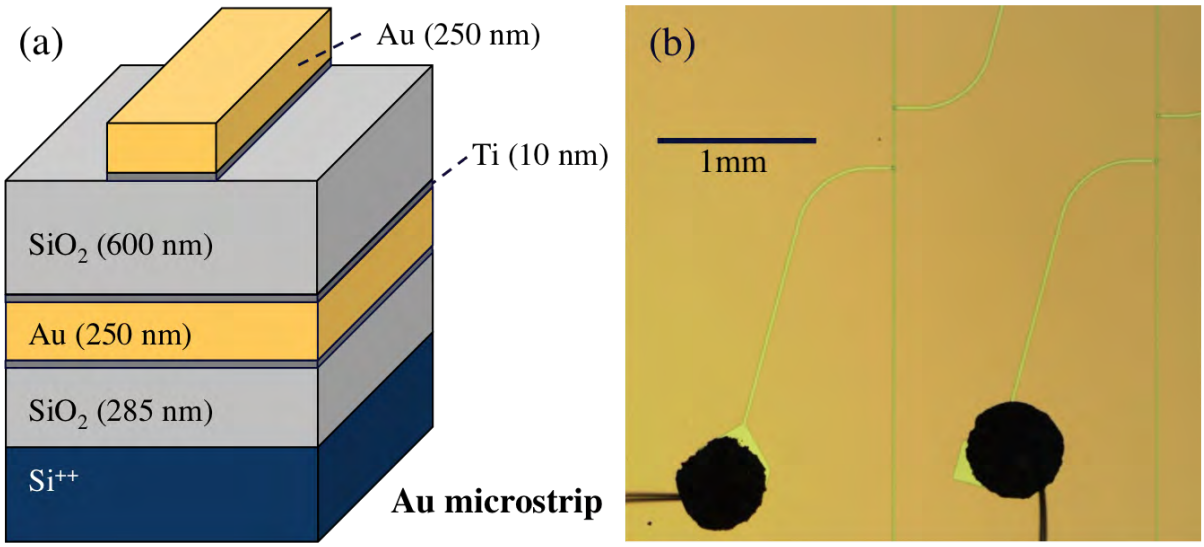

Figure 3.15.: **Au microstrip**: (a) Firstly, 10 nm titanium, 250 nm gold, 10 nm titanium and 600 nm SiO_2 are deposited on a doped silicon wafer to fabricate a gold/ SiO_2 substrate. Then, photoconductive switches and transmission lines are deposited. (b) Micrograph of the sample with manually contacted gold wires (black blobs are silver conductive paste).

3.5. Experimental pump-probe setup and methods

A block diagram of the experimental setup used for pump-probe measurement to characterize the propagation properties of all transmission lines is shown in figure 3.16.

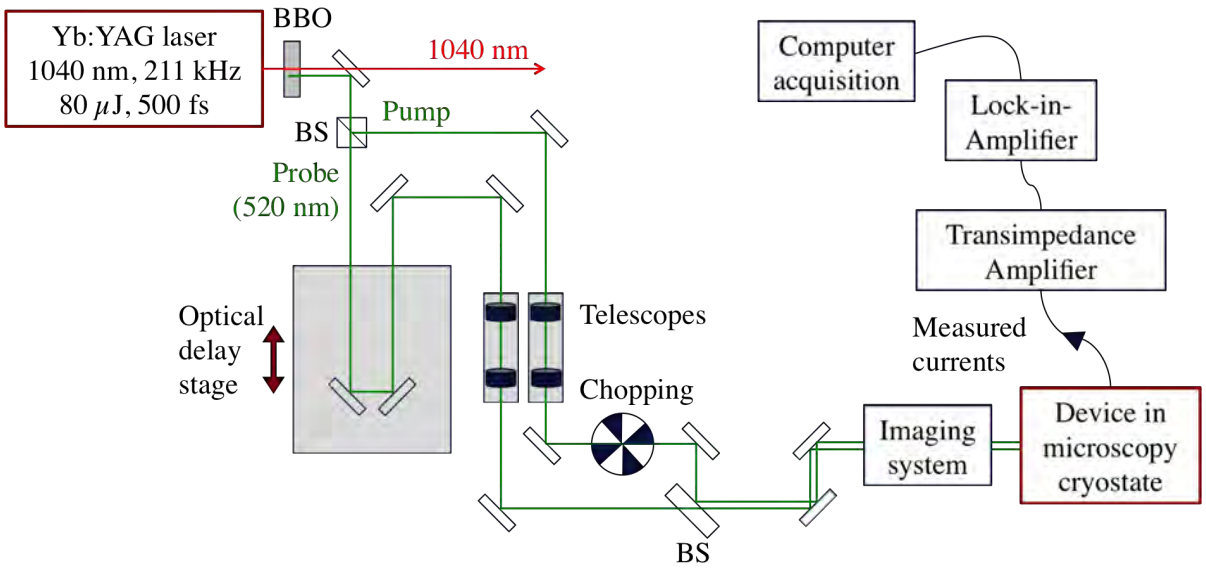

Figure 3.16.: Block diagram of the experimental pump-probe setup.

A commercial Yb-based laser system provides a train of ultrafast laser pulses with a central wavelength of 1040 nm, pulse duration of $\sim$ 500 fs, repetition rate of 211 kHz and pulse energy of $\sim$ 80 µJ. 1 % of the total power of 16 W is converted to the second harmonic wavelength of 520 nm by sending the beam through a β-barium-borate (BBO) crystal. The 520 nm light, which is required to trigger the photoconductive switches, is separated from the 1040 nm light by a dichroic mirror.

The green 520 nm beam is then routed through a beam splitter and divided into pump and probe beam. The path length of the probe beam can be adjusted via an optical delay stage to change its timing with respect to the pump beam. For on-chip measurements, both beams are coupled into the microscope and focused on the switches. The switches are operated with peak fluences of $\sim 15\,\mathrm{mJ/cm^2}$, ensuring a non destructive operation, while inducing a large change of conductivity in the silicon. The spot sizes (FWHM) of the focused beams are determined by knife-edge-measurements[1]. The spot size of 15 µm (see figure 3.17) is ideal to evenly illuminate the gaps of the photoconductive switches (gap size: 3 µm).

The device is mounted in an optical microscopy cryostate with wire ring for high frequency transport measurements. During the measurements, the sample is imaged via an optical microscope setup. The devices are cooled down to a base temperature

[1] A razor blade is mounted on a translation stage and moved though the beam at focus position. By recording the power behind the razor blade for different positions, the beam profile can be measured.

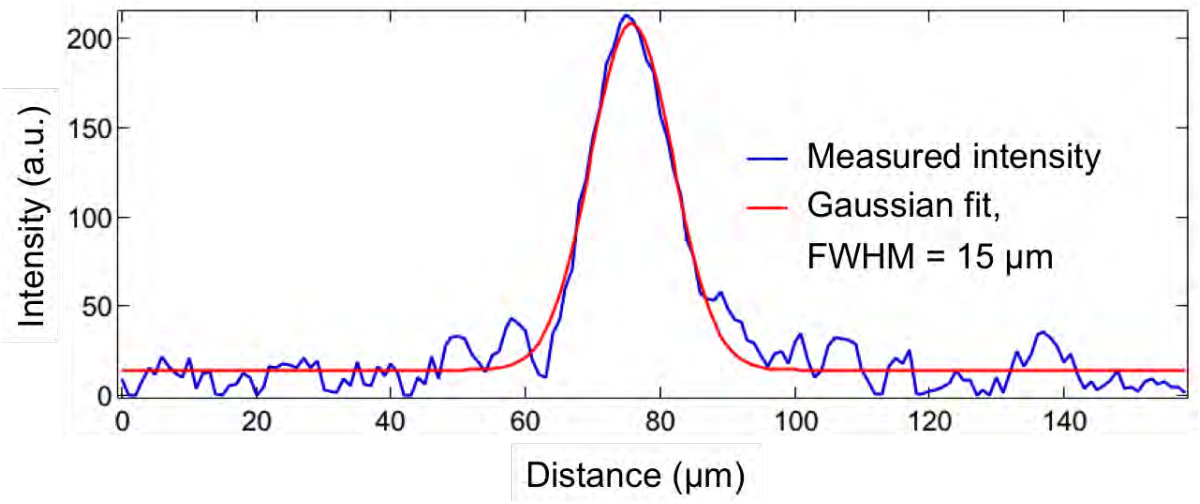

Figure 3.17.: Measured profile of the green 520 nm pump beam. The red line is a Gaussian fit to the data.

of 80 K. The green laser beams are aligned onto the switches using the imaging of the sample and are actively stabilized during the measurements.

Generated currents are amplified by a home-built transimpedance amplifier (developed by T. Matsuyama, SSU-UE, bandwidth: 1-10 kHz, amplification: $2{\cdot}10^9$ V/A, DC input signals are blocked with 1 µF capacitance). Signals can be isolated using a standard lock-in amplifier and optical chopping techniques for the pump beam: A mechanical chopper rotates continuously at a frequency of 406 Hz and feedback is given to the lock-in amplifier [8].

3.6. On-chip THz measurements

This section describes the procedure of on-chip pump-probe measurements to characterize the THz propagation in the five fabricated transmission line geometries. The following sections focus on the transmission line circuits with 400 µm distance between the photoconductive switches, where dispersion and damping are most prominent. To characterize the signal damping, measurements of 100 µm and 400 µm structures are compared.

Firstly, the photoconductive switches are annealed and characterized. Then, pump-probe data can be collected, as described in the following sections.

3.6.1. Characterization of the photoconductive switches

For photoconductive switches used for THz generation and detection, a short carrier lifetime is crucial to ensure that the pulses are fast enough to generate THz frequency components. In addition, a high switch resistivity is desirable to suppress any background currents and increase the signal-to-noise ratio. Therefore, the photoconductive

switches are laser annealed (laser power: 1 mW) at room temperature in vacuum reducing their resistance from hundreds of MΩ to tens of MΩ. This process provides a significant decrease of the carrier lifetime by diffusing gold into the silicon switch.

After annealing, the sample is cooled down to a temperature of 80 K and the switch resistance is measured by recording I-V curves. A linear switch response (ohmic contact) is crucial to generate and detect signals in the transmission lines. Figure 3.18 shows the I-V curves for the doped silicon microstrip sample (a) and the simplified stripline geometry (b). The two switches in the doped silicon microstrip show a linear I-V characteristic with a switch resistance of 1.6 GΩ. This is in good agreement with previous sample generations.

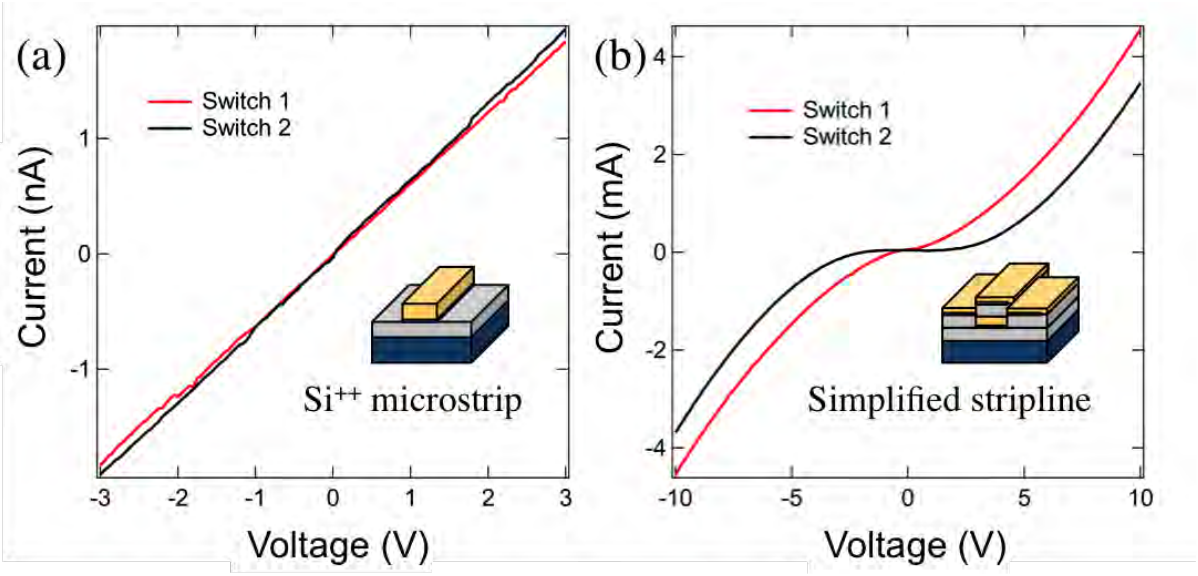

Figure 3.18.: IV sweep characteristics with varying bias of the two switches of the transmission line circuit with 400 µm distance between the switches for the (a) doped silicon microstrip and (b) simplified stripline. In the simplified stripline, signals can tunnel through the pinholes of the evaporated SiO_2 which is leading to a low photoconductive switch resistance.

In contrast, the switches on the simplified stripline seem to exhibit a strong diode-like behaviour. Note that the current for an applied bias voltage of 10 V exceeds 3 mA. This is explained by the low breakdown voltage of the evaporated SiO_2. For voltages larger than $\sim$ 2 V, the SiO_2 breaks down and currents tunnel from one side of the switch through the evaporated dielectric to the top gold layer and then in the contacted transmission line on the other side of the switch. Thereby, the switch is bypassed and the I-V curve no longer characterizes the switch, but rather describes the behaviour of the SiO_2 layer. This phenomenon is found on all samples except the doped silicon microstrip and the stripline with stripline islands, where the top gold layers are separated from each other in the switch regions. As a result, the generation switch can only be biased with small voltages. Thus, the generated THz pulse is small

and the signal-to-noise ratio of the measured curves is low.

This shows that the quality of the evaporated SiO_2 is important and still object of optimization. Fortunately, this problem will be solved as soon as the heater is installed in the evaporator.

In order to quantify the dispersion and damping of the electric field propagating in the transmission lines, the photoconductive switches have to be calibrated. This is performed by measuring the generated photocurrent in the switches upon illumination with laser light. First, the pump and probe beam (laser power per beam is 1 mW) are focussed onto the generation and detection switch using mirrors in front of the microscope objective. The final alignment is accomplished by maximizing the photocurrents generated by the switches.

Then, the switches are individually calibrated. The lock-in voltage is recorded for different applied DC bias voltages across each photoconductive switch. A calibration curve for the doped silicon microstrip is shown in figure 3.19. The calibration factor is given by the slope of the curve. In order to compare data taken from different transmission lines, the recorded data is divided by the calibration factor of the detector and the generator switch.

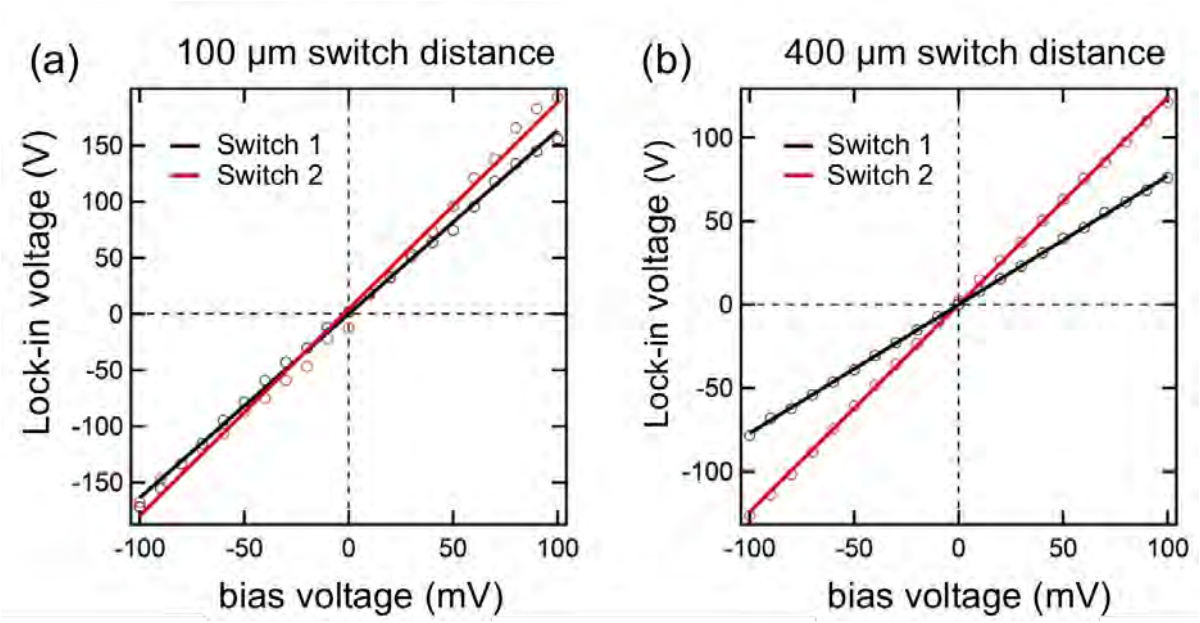

Figure 3.19.: Calibration curves for the doped silicon microstrip. Switches are separately calibrated for the 100 µm circuit (a) and the 400 µm circuit (b). The lock-in voltage is recorded as function of bias voltage across the switch. To calibrate the different circuits, the measured signal is divided by the slopes of the curves for the generation and detection switch.

3.6.2. Pump-probe signal data collection

Once the photoconductive switches are characterized, pump-probe signal data can be collected. Therefore, the generation switch is biased with a DC voltage and illuminated by the pulsed laser beam with an average power of 1 mW. The generated THz pulse is detected at the second switch, which is triggered by time delayed laser pulses (see figure 2.4). To increase the signal-to-noise ratio and to eliminate photocurrents generated by the unbiased detection switch, the pump beam is periodically modulated by a mechanical chopper. Photocurrents are measured with a transimpedance amplifier and lock-in techniques using the feedback of the mechanical chopper.

The generation switch can be biased with voltages of 1 to 30 V, depending on the break-down voltage. The measured signals are presented in the next chapter.

3.6.3. Van der Pauw measurement of doped silicon

The specific conductance σ of the doped silicon wafer is an important parameter for the electromagnetic simulations. As discussed in the theory chapter, the transmission line properties change for different values of the specific conductance of the ground plane. σ depends on the doping and varies between silicon wafers from different manufacturers. Therefore, σ of the utilized doped silicon wafers is measured in a Van der Pauw measurement [52].

A 1 cm x 1 cm doped silicon wafer with a thickness t_{Si} = 790 µm is contacted in the four corners. The contacts are numbered from 1 to 4 in a counter-clockwise order, beginning at the bottom left contact. A current I is imprinted from contact 1 to 2 and the voltage drop U_{34} across contacts 3 and 4 is measured. Then, the measurement configuration is rotated by 90° and the voltage U_{23} is recorded. The specific conductance σ, which is the inverse of the sheet resistance ρ, can be calculated by

$$\sigma = \frac{1}{\rho} = \frac{ln2}{\pi t_{Si}} \frac{2I}{U_{34} + U_{21}} \frac{1}{f(U,I)}, \tag{3.4}$$

where $f(U,I)$ is the correction factor [52].

4. Experimental results and electromagnetic simulations

This chapter presents the results from on-chip pump-probe measurements of the five samples studied here: Doped silicon microstrip, simplified stripline, stripline, stripline with stripline islands and gold microstrip (see chapter 3.4). Measured signals are compared to electromagnetic simulations performed by Toru Matsuyama with the full wave analysis software CST microwave studio.

For frequency domain simulations the software utilizes S-parameter analysis. S-parameter analysis (S for scattering) is a convenient method to describe a given circuit in terms of waves rather than voltages or currents, when high frequencies are propagating. The approach is discussed in detail for example by Caspers [53]. Thereby, transmission and reflection coefficients of the propagating wave are calculated with matrix calculations, delivering the secondary line constants γ (propagation constant) and Z (characteristic impedance) as function of frequency ω. The primary line constants R', L', C' and G' can be derived from γ and Z as shown in equation 2.11.

The transmission line geometries are constructed with a mesh that is fine enough to capture THz frequencies. Simulations are performed in time and frequency domain.

For frequency domain simulations, a transmission line of 420 µm length is chosen, in which an excitation signal of 800 GHz bandwidths is analysed after 10 µm (reference), 100 µm, 200 µm, 300 µm and 400 µm.

For time domain simulations, the structures are extended by 1 mm to 1.42 mm to avoid reflections from the end of the transmission line. Time domain simulations use a gaussian excitation with length (FWHM) of 1 ps (which corresponds to a bandwidth of 800 GHz). The propagating pulse is analysed simultaneously to the frequency domain simulations after 10 µm (reference), 100 µm, 200 µm, 300 µm and 400 µm.

The excitation signal in time domain simulations is a symmetric gaussian in order to provide information about any distortion caused by dispersion and damping. In experiment, the pulse shape is slightly asymmetric. The photoconductive switches are triggered with gaussian femtosecond laser pulses, causing a rapid excitation of free carriers in the switch (as discussed in chapter 2.1.1). However, these free carriers require in spite of the short carrier lifetime of α-silicon some time to recombine after the excitation, causing an asymmetric pulse shape. This effect is small, but has to be considered when comparing experimental and simulated results.

Measurement data and results from electromagnetic simulations are presented in section 4.1 for the doped silicon microstrip, in section 4.2 for the stripline geometries, and in section 4.3 for the gold microstrip.

4.1. Doped silicon microstrip

The doped silicon microstrip is the transmission line structure that has been used in former experiments and is known to be dispersive. The goal of this thesis is to develop single-mode transmission line geometries that are less dispersive compared to the formerly utilized structure. The doped silicon microstrip was measured and is presented here as a reference.

Calibrated measured signals after 100 µm and 400 µm propagation are shown in figure 4.1.

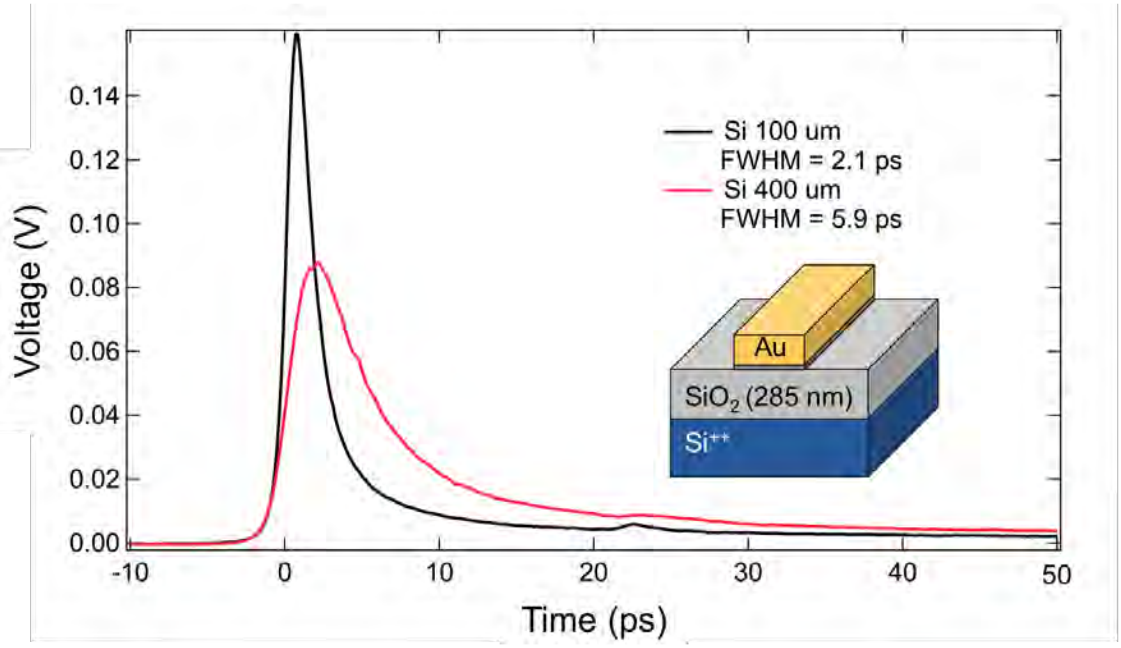

Figure 4.1.: Measured signals in the doped silicon microstrip after 100 and 400 µm propagation: The THz pulse disperses from < 1ps at excitation to 2.1 ps FWHM after 100 µm propagation. After 400 µm propagation, the pulse has a FWHM of 5.9 ps and is damped by roughly 50 % in respect to the pulse amplitude at 100 µm.

THz pulses in the doped silicon microstrip disperse from < 1ps (FWHM) at excitation to 2.1 ps (FWHM) after 100 µm propagation. After propagating 400 µm, the pulse distorted to 5.9 ps (FWHM) and the amplitude is reduced by a factor of two compared to a propagation distance of 100 µm.

As discussed in chapter 2.2.3, the maximum phase velocity $\frac{1}{\sqrt{L'C'}}$ can be found at the steepest slope of the measured signals. The maximum phase velocity of the signal propagating in the doped silicon microstrip can be determined by measuring signals propagating from switch 1 to switch 2 (bias voltage at switch 1, lock-in at switch 2) and the other way around without changing the laser alignment. In both measurements the optical delay stage changes the path length of the laser beam on switch 1. Additionally, the pump-probe measurements are conducted for positive and negative bias voltages, as shown in figure 4.2.

The time delay Δt between the pump and probe laser pulse is created by moving the stage by a distance Δs, so that the laser pulses going in and out of the stage are delayed by $\Delta t = 2\Delta s/c$, where c is the speed of light. The distance Δs = 1.6 mm shown in figure 4.2 corresponds to the time the pulse requires to travel twice the switch distance. For the black curve, laser pulse 1 triggering switch 1 arrives earlier on the sample than pulse 2. The time delay $\Delta t_1 = d/v_{ph,max}$ corresponds to the time the pulse requires to travel from switch 1 to switch 2. For the red curve, laser pulse 2 hits the sample before laser pulse 1. Here, the pulses are delayed by $\Delta t_2 = -d/v_{ph,max}$. Consequently, the distance Δs corresponds to the time delay $\Delta t = \delta t_1 - \Delta t_2 = 2d/v_{ph,max}$. Thus, the maximum phase velocity is given by:

$$v_{ph,max} = \frac{d \cdot c}{\Delta s} = \frac{0.4\,\mathrm{mm} \cdot c_0}{1.6\,\mathrm{mm}} = 0.25c. \tag{4.1}$$

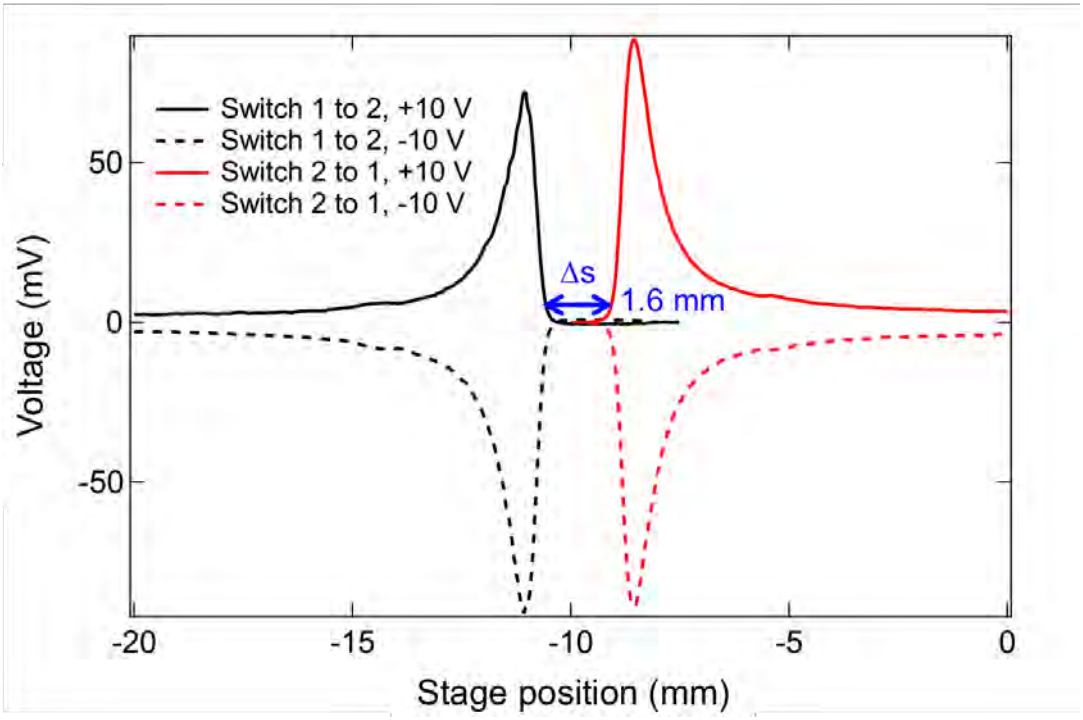

Figure 4.2.: Pump-probe measurement of the 400 µm circuit from switch 1 to switch 2 and vice versa for positive and negative bias voltage. With a steepest slopes distance of 1.6 mm, the maximum phase velocity of the pulses propagating in the doped silicon microstrip at THz frequencies is 0.25c.

A Fourier transform of the measured signals for 100 µm and 400 µm switch distances is shown in figure 4.3. The bandwidth decreases by a factor of two when the signal propagates from 100 µm to 400 µm distance in the doped silicon microstrip. Especially the higher (THz) frequencies are disappearing after a propagation distance of 400 µm.

In order to perform electromagnetic simulations for the doped silicon microstrip, the specific conductance of doped silicon is measured by the van der Pauw method as describes in chapter 3.6.3. The correction factor f from equation 3.4 can be set to one,

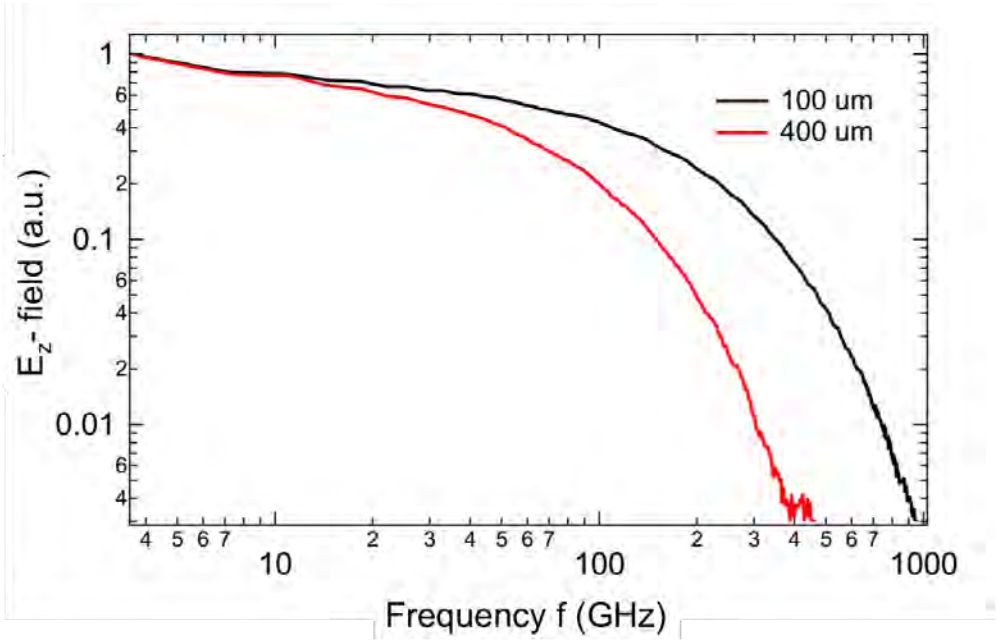

Figure 4.3.: Fourier transformation of the measured signals in the doped silicon microstrip after 100 µm and 400 µm of propagation: The bandwidth is decreasing by a factor of two after propagating 300 µm and higher (THz) frequencies are vanishing.

because the measurements rotated by 90° varied only by a factor of less than two. The measured specific conductance of doped silicon σ_{Si} = 30000 S/m is constant over the temperature range from 20 K to 300 K.

The results of the simulations are studied in the following. Figure 4.4 depicts a cross section of the electric field of the THz pulse in the doped silicon microstrip structure.

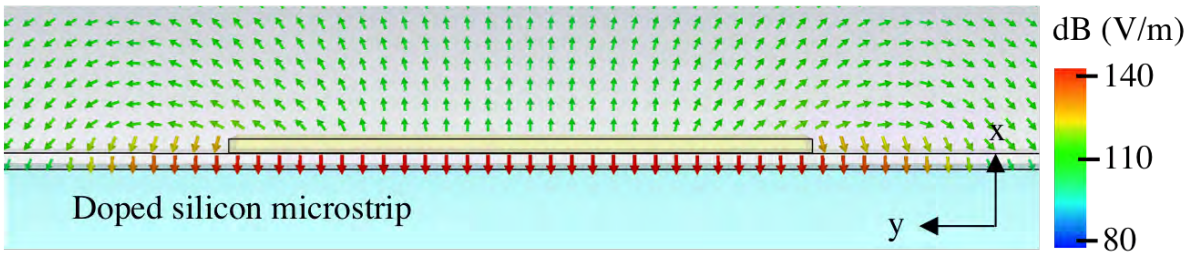

Figure 4.4.: Cross section of the electric field of the THz pulse in the doped silicon microstrip: The electric field lines are strongly confined between the gold signal line and the doped silicon ground.

The results for the simulated mode propagation are presented in figure 4.5. The solid lines in figure 4.5 show the electric field of the quasi-TEM mode with a reference signal (after 10 µm of propagation) and snap shots of the signal taken after 100 µm, 200 µm, 300 µm and 400 µm propagation distance. The dashed lines represent a higher order mode and will be discussed later.

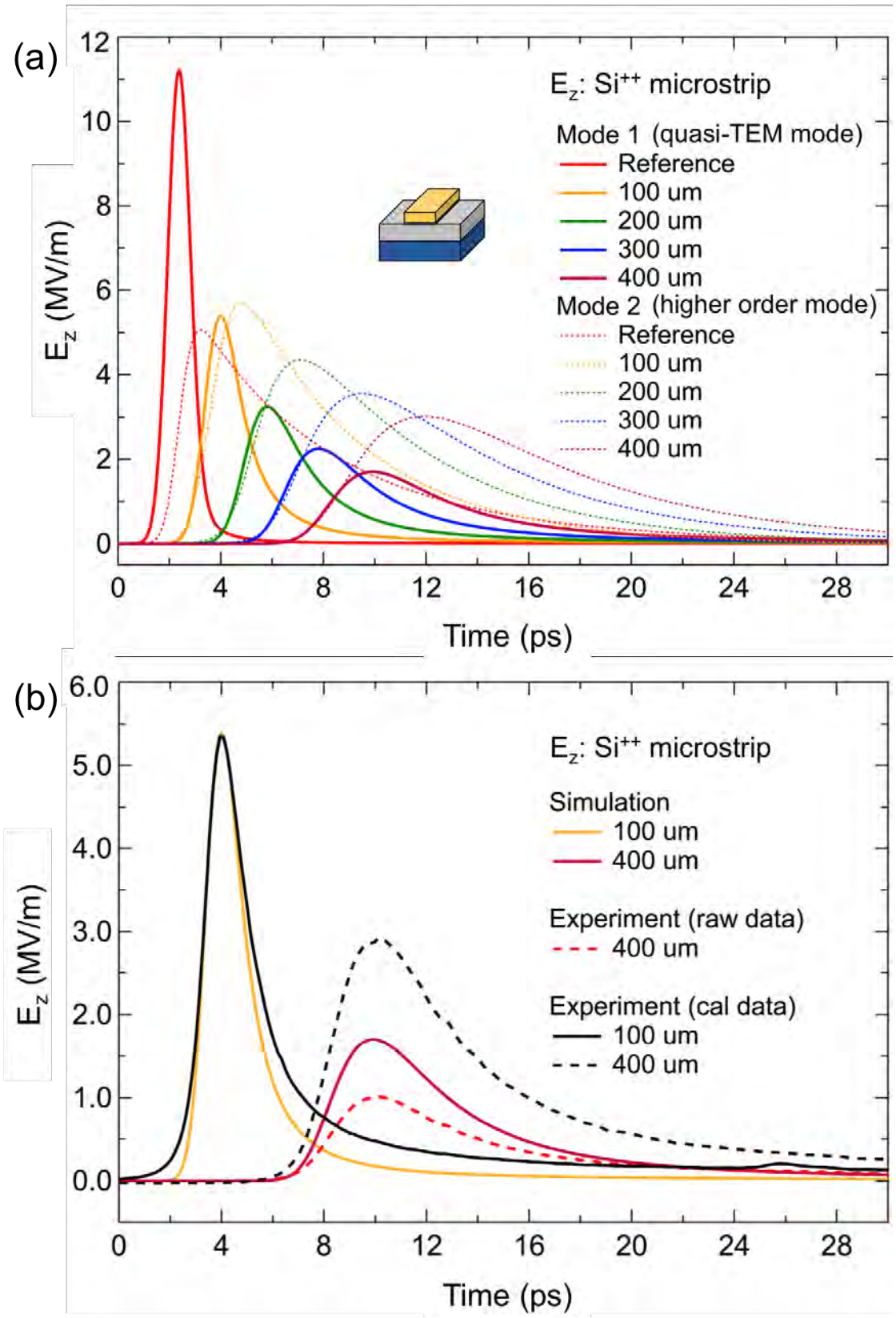

Figure 4.5.: Measured and simulated pulse propagation in a doped silicon microstrip with 285 nm SiO_2 layer and 10 µm wide signal lines: (a) Simulated propagation of the quasi-TEM mode and the first higher order mode for five different propagation distances (Reference = 10 µm). (b) Simulated data as well as experimental (raw and calibrated) data is shown for 100 and 400 µm propagation distances.

For comparison, measured signals with 100 µm and 400 µm distance between the photoconductive switches are depicted in figure 4.5 (b). The amplitudes of the measured signals are scaled just that the signal amplitudes of measured and simulated signals for the 100 µm circuits are equal. For the measured 400 µm propagated signal, both raw and calibrated data is shown. The simulated pulse (400 µm) has an amplitude with a value between the measured raw and calibrated data. Since power and pointing of the pump as well as probe beam can slightly vary during the measurement, small errors can occur.

However, the amount of pulse dispersion is in good agreement between measurement and simulation. The measured signals are slightly broader and have longer decays. Two reasons can be identified for this behaviour. Firstly, the signal generated by a photoconductive switch has an asymmetric shape with a longer decay, which is due to the carrier relaxation process (as discussed above). Secondly, the simulations reveal that a second higher order mode can propagate in the microstrip. The amplitude of this mode relative to the quasi-TEM mode is strongly dependent on the choice of ports as well as the chosen free space around the microstrip structure. Thus, a reliable statement about the impact of this higher order mode in experiment is not possible. Nevertheless, the fact that the measured signals show a longer decay than the simulated signals of the quasi-TEM mode suggests that also this higher order mode is weakly excited by the photoconductive switch.

Spectra for the simulated signals propagating in a doped silicon microstrip are calculated for different propagation distances. The result is shown in figure 4.6 and matches well with the Fourier transform of the measured pulses shown in figure 4.3.

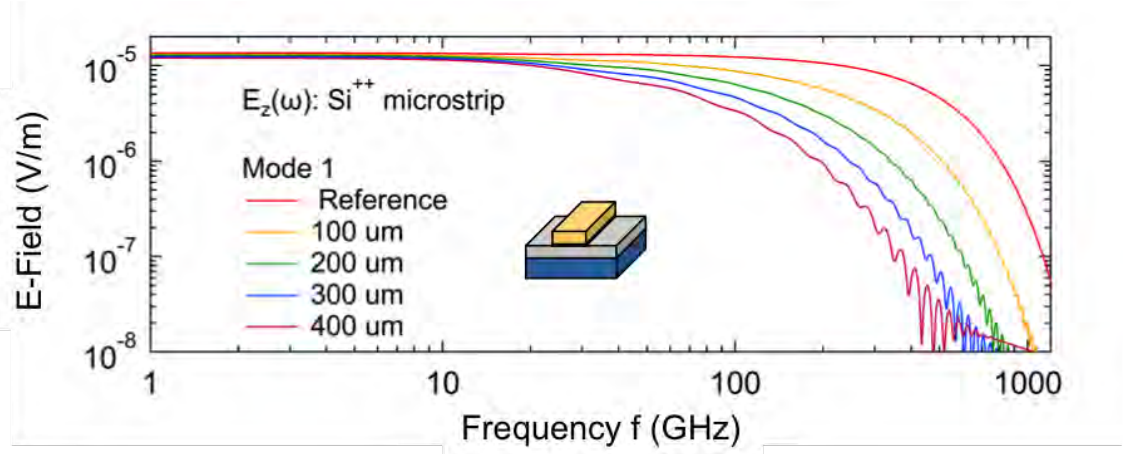

Figure 4.6.: Simulated spectra for signals propagating in a doped silicon microstrip: The pulse bandwidth is decreasing with the signal propagation length. Especially THz frequencies are vanishing after a propagation of a few hundreds of micrometers.

Measurements and simulations of the doped microstrip presented in this section show that this transmission line geometry is not ideal to guide ultrashort pulses. High

dispersion and attenuation suppresses high frequency components and after only 400 µm of propagation almost no frequency component at 1 THz remains. The following sections show that the more sophisticated stripline designs introduced before indeed yield an improvement for the propagation of THz pulses.

4.2. Stripline

The fabrication of striplines is a first approach to develop less dispersive transmission line geometries for on-chip THz spectroscopy experiments. In contrast to the microstrip, striplines are symmetrically surrounded by a dielectric medium and two ground planes (see chapter 2.3.2). Theory suggests that this type of transmission line is less dispersive and only one pure TEM mode is propagating.

As discussed in chapter 3.4, three different types of striplines are fabricated for on-chip measurements: The simplified stripline with a nonplanar gold ground layer on top, the stripline with a planar symmetric ground layout and the stripline with stripline islands with a symmetric ground plane but with islands of SiO_2 and gold to avoid breakdown of the evaporated SiO_2. When the heater is installed in the evaporator, it will be possible to evaporate high-quality SiO_2 with high breakdown strength.

Measured signals from the three different stripline designs and the doped silicon microstrip with 400 µm switch distance are shown in figure 4.7.

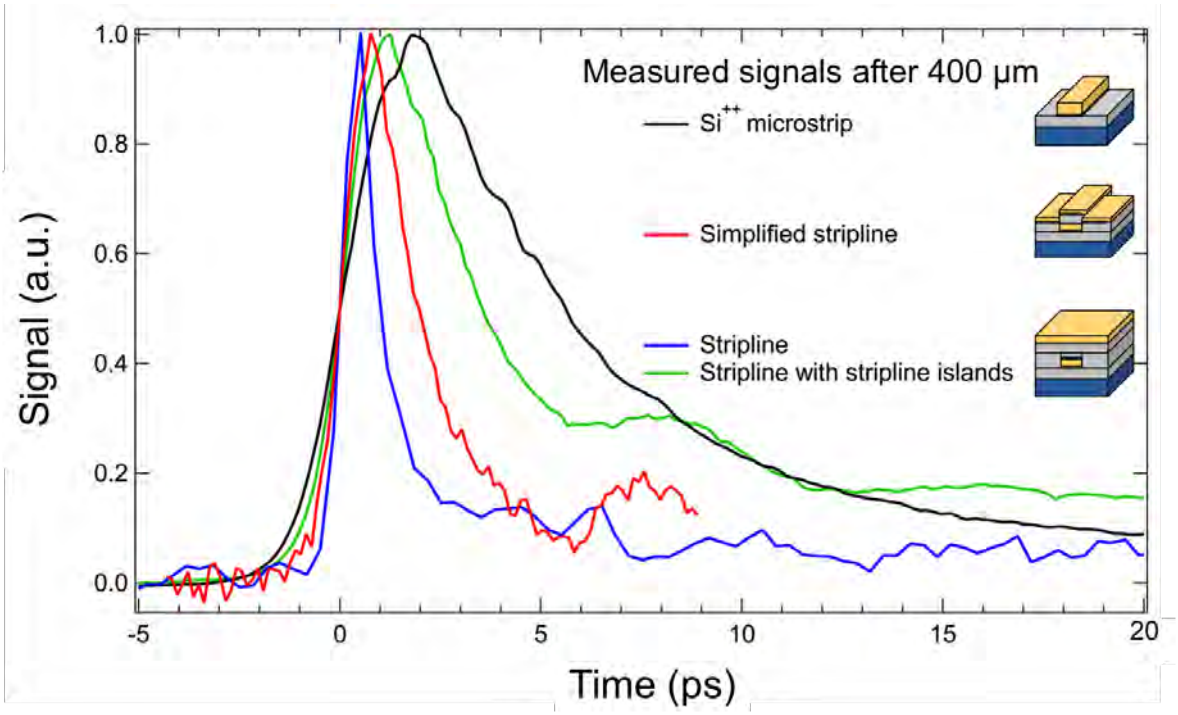

Figure 4.7.: Measured signals after 400 µm propagation distance in the doped silicon microstrip and the three different stripline designs: The width (FWHM) of the signal is 5.9 ps in the doped silicon microstrip, 2.0 ps in the simplified stripline, 1.1 ps in the stripline, and 3.5 ps in the stripline with islands.

The signal in the doped silicon microstrip (black curve), has a FWHM of 5.9 ps after a propagation distance of 400 µm. This signal is the benchmark for the more sophisticated stripline geometries. With the simplified stripline, the pulse dispersion can be limited to 2.0 ps FWHM. The symmetric and planar ground layers of the stripline sample further improves the pulse dispersion to only 1.1 ps FWHM. The signal propagating in the stripline with stripline islands is broadened to 3.5 ps. Thus, the stripline with islands is more dispersive than the other two stripline designs. The more developed distortion is presumably caused by reflections from the pulse at the edges of islands of the top ground layer.

To check nonlinearities in the signal generation, propagation, and detection, different sized signals are coupled into the stripline with stripline islands. Signals for bias voltages on the generation switch ranging from -30 V to 30 V are shown in figure 4.8. The linear dependence of the signal size on the bias voltage shows that the circuits are operated in the linear regime. This is an important detail to perform and calibrate measurements.

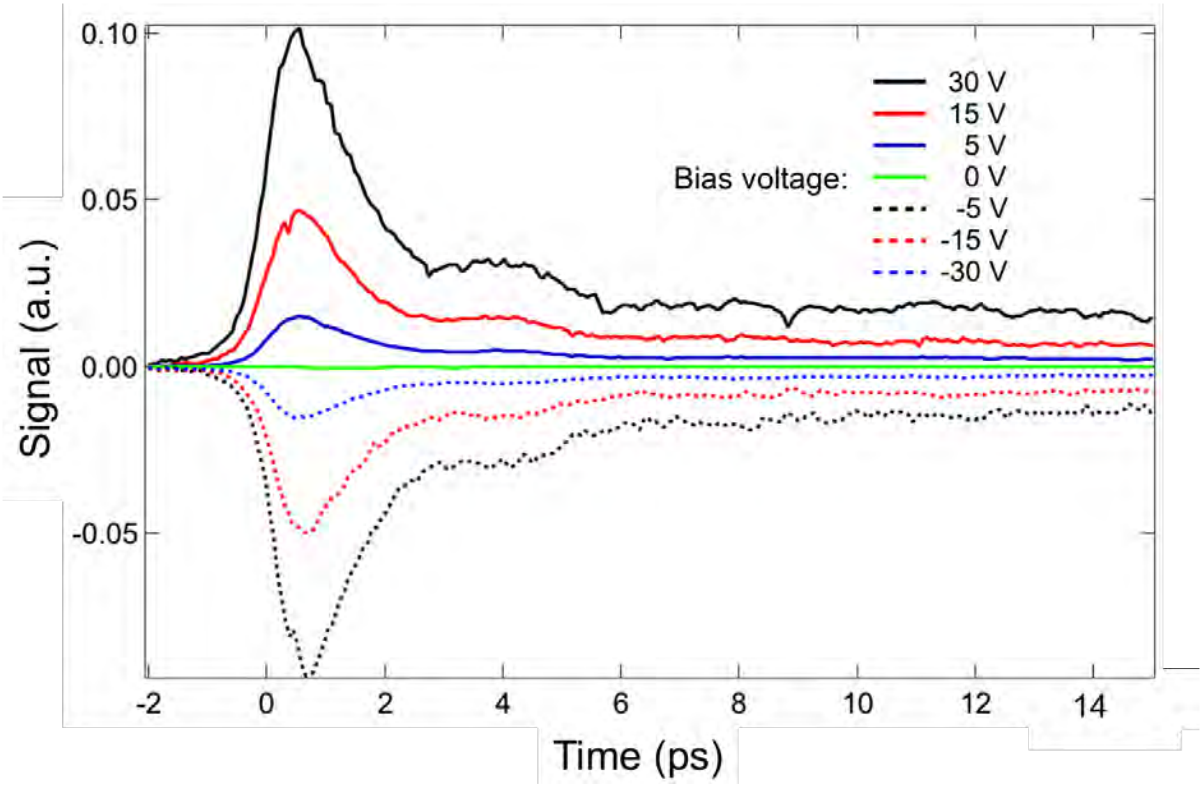

Figure 4.8.: Signals propagating in the stripline with stripline islands measured with different applied bias voltages: The signal amplitude is proportional to the applied bias voltage.

Electromagnetic simulations are performed for the simplified stripline and the stripline sample and are studied in the following. Figure 4.9 depicts the cross sections of the electric field of the THz pulse in the simplified stripline structure and the stripline structure.

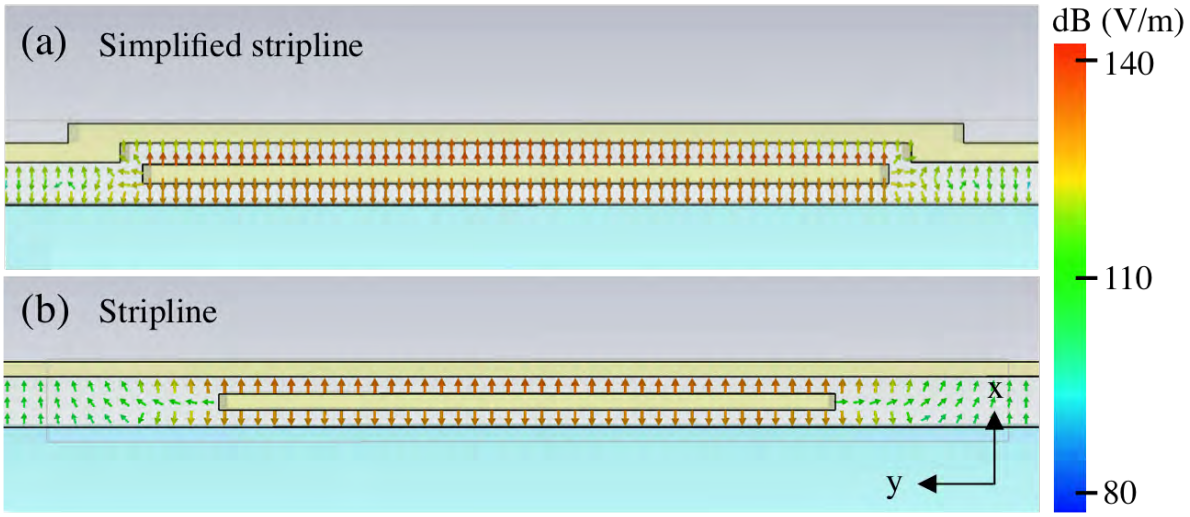

Figure 4.9.: Cross section of the electric field of the THz pulse in the (a) simplified stripline structure with a nonplanar top gold ground and (b) stripline structure with planar grounds. The blue area depicts the doped silicon ground.

Results gathered from experiment as well as simulation for the simplified stripline are shown in figure 4.10.

As shown in figure 4.10, simulations are performed for the simplified stripline with and without switch windows in the top ground layer. In experiment it is not possible to fabricate striplines without such windows since the photoconductive switches have to be laser triggered (switch windows are shown in figure 3.10).

In figure 4.10 (a) the simulation for pulse propagation in an ideal stripline without windows is shown. Since striplines have two ground lines, the electric field can propagate on top and on bottom of the signal line. Since the simplified stripline is not symmetric (planar doped silicon ground versus nonplanar gold ground), the field propagating on top is smaller compared to the field propagating on bottom. However, pulses propagating in simplified striplines suffer less from dispersion in contrast to the doped silicon microstrip.

When switch windows are added to the simulation for the simplified stripline, especially the 100 µm propagated signal matches well with the simulation as shown in figure 4.10 (b). The underswing around 6 ps is only present in the geometry with windows, which indicates that it is caused by reflections at the window, which interrupts the ground line. The measured pulse in the 400 µm circuit is broader and has a higher amplitude than the simulated signal. This is possibly due to reflections in the switch window of the generation switch. In the simulation, only one switch window for the detection switch, which is 3 µm larger than the switch itself in all directions, has been realized. The simulation of a generation switch window is not possible, since an excitation signal is directly guided into the simulation box via a wave port.

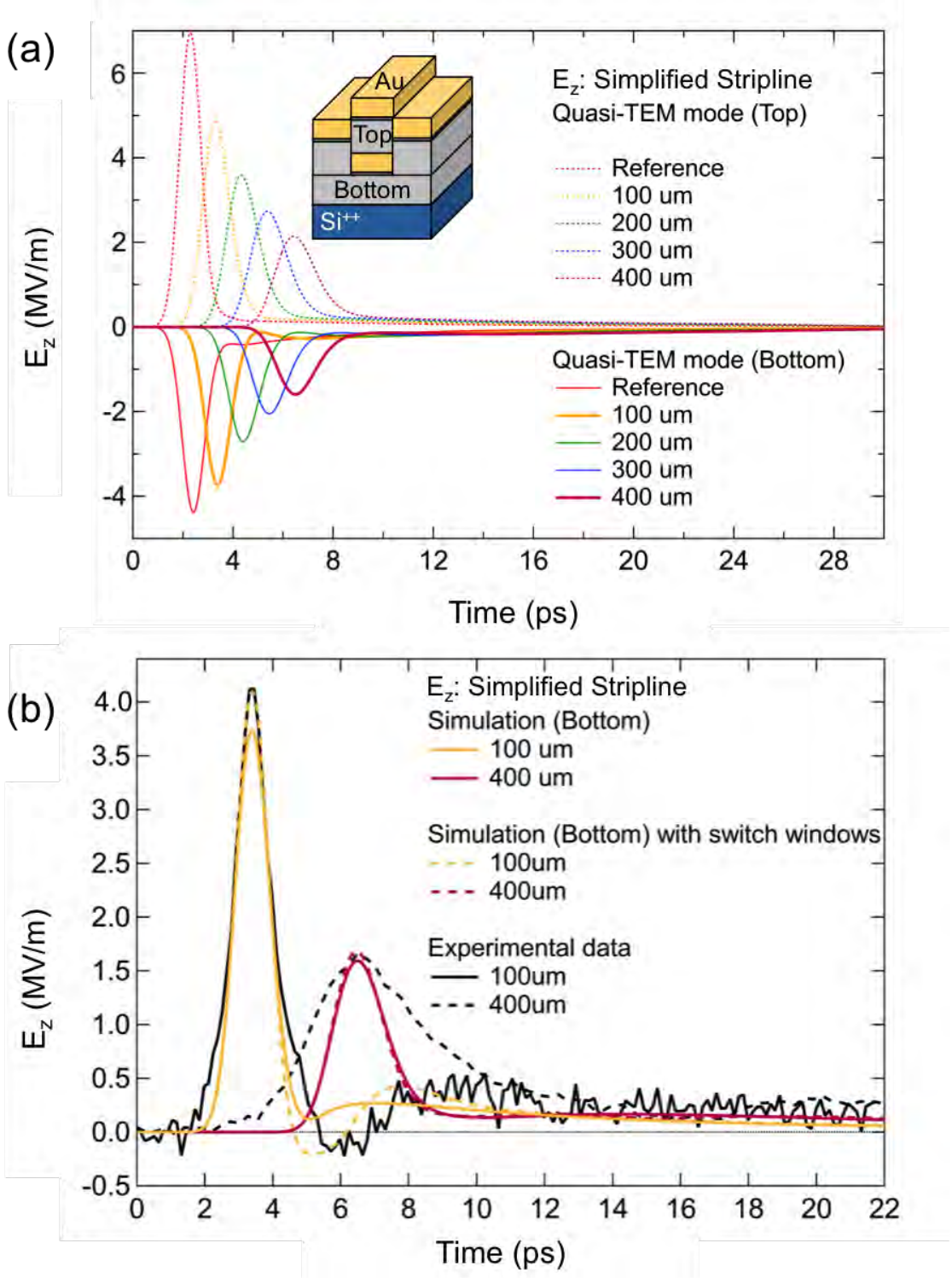

Figure 4.10.: Measured and simulated pulse propagation in the simplified stripline. (a) Simulated pulse propagation of the quasi-TEM mode for different propagation distances in a simplified stripline without windows for the photoconductive switches. The z-component of the electric field is measured above (top, dashed lines) and below (bottom, solid lines) the signal line. (b) Experimentally measured pulses for 100 and 400 µm propagation distances in comparison with simulated propagation in a simplified stripline without and with switch windows in the top gold ground layer. In the experiment the windows are required to trigger the switches with laser pulses.

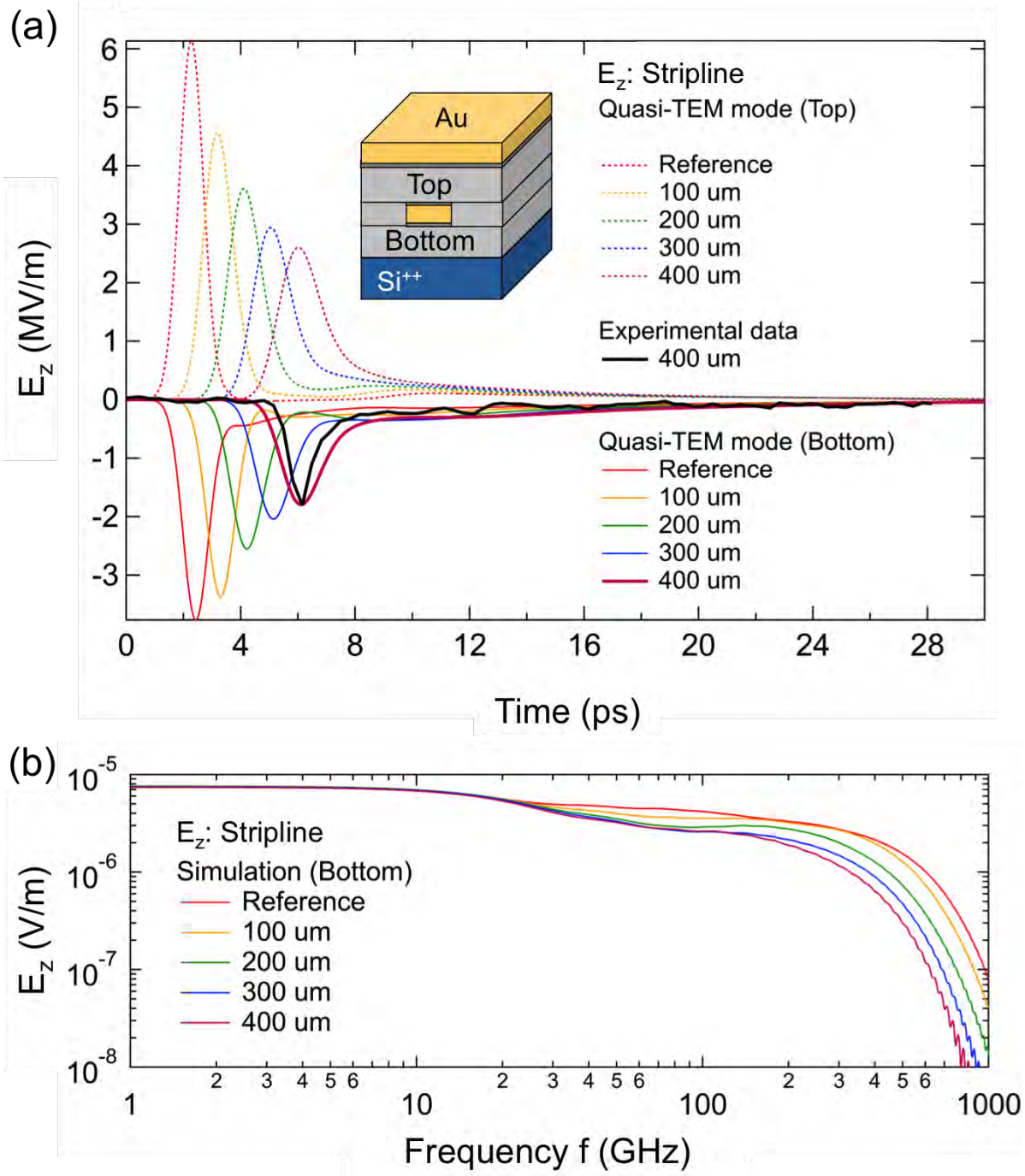

Figure 4.11.: (a) Simulated propagation of the electric field (z-Component) above (dashed lines) and below (solid lines) in the stripline without windows for the photoconductive switches. The black curve represents the corresponding experimental data. (b) Simulated spectra for signals propagating in a stripline: The pulse bandwidth is higher in comparison to the doped silicon microstrip.

Next, simulations for the stripline sample are performed. The simulated propagation for the top and bottom electric field as well as experimental data is shown in figure 4.11 (a). Only the pulse for the 400 µm circuit is shown, since other circuits with different distances between the photoconductive switches on this sample suffered either from a

high amount of reflections or shorts between signal line and top gold layer. This underlines the difficulty to fabricate such symmetric striplines with common laser lithography and thermal evaporation methods. However, the measured pulse is in good agreement with the simulation.

Additionally, spectra for the propagating signals in the stripline are simulated and shown in figure 4.11 (b). The bandwidth of the propagating signals is clearly higher in comparison to the doped silicon microstrip (compare figure 4.6). THz frequencies are vanishing less with increasing propagation distance.

Simulations for the stripline with stripline islands are not performed, since the measured amount of pulse distortion and reflections are too high to be a serious candidate for an on-chip THz spectroscopy transmission lines.

4.3. Au microstrip

The last transmission line design investigated in this thesis is a microstrip on an Au/ SiO_2 substrate. The idea is that not only the transmission line geometry, but moreover the conductivity of the material used for the ground is crucial to allow low-dispersive signal propagation. In the doped silicon microstrip, the ground is doped silicon with a measured specific conductance of 30000 S/m (see chapter 4.1). In the fabricated striplines, the bottom ground is doped silicon, but the top ground is gold. The specific conductance of gold is $4.6 \cdot 10^7$ S/m. First, a microstrip is built on the Au/ SiO_2 substrate, to test the substrate quality. Later, also the more complicated stripline designs can be built on the new substrate.

The measured signal in the gold microstrip which propagated over a distance of 400 µm is shown in figure 4.12. The signal has a FWHM of 1.1 ps, the same width as the measured signal in the stripline. Therefore, the higher conductivity of the ground material and the higher dielectric thickness improves the dispersion by more than a factor of five with respect to the doped silicon microstrip.

The results of the electromagnetic simulations are studied in the following. Figure 4.13 depicts a cross section of the electric field of the THz pulse in the gold microstrip structure.

The simulated signal propagation in the fabricated gold microstrip geometry is depicted in figure 4.14 (a). The measured signal matches well with the simulated signal. The simulation further shows, that besides the low dispersion, also the damping is low in the gold microstrip compared to all other fabricated and simulated transmission lines.

A further simulation result is shown in figure 4.14 (b), where the bandwidth of the pulse is almost constant for the four propagation distances. Especially, the THz frequencies are not vanishing, which is an important improvement for on-chip THz spectroscopy experiments.

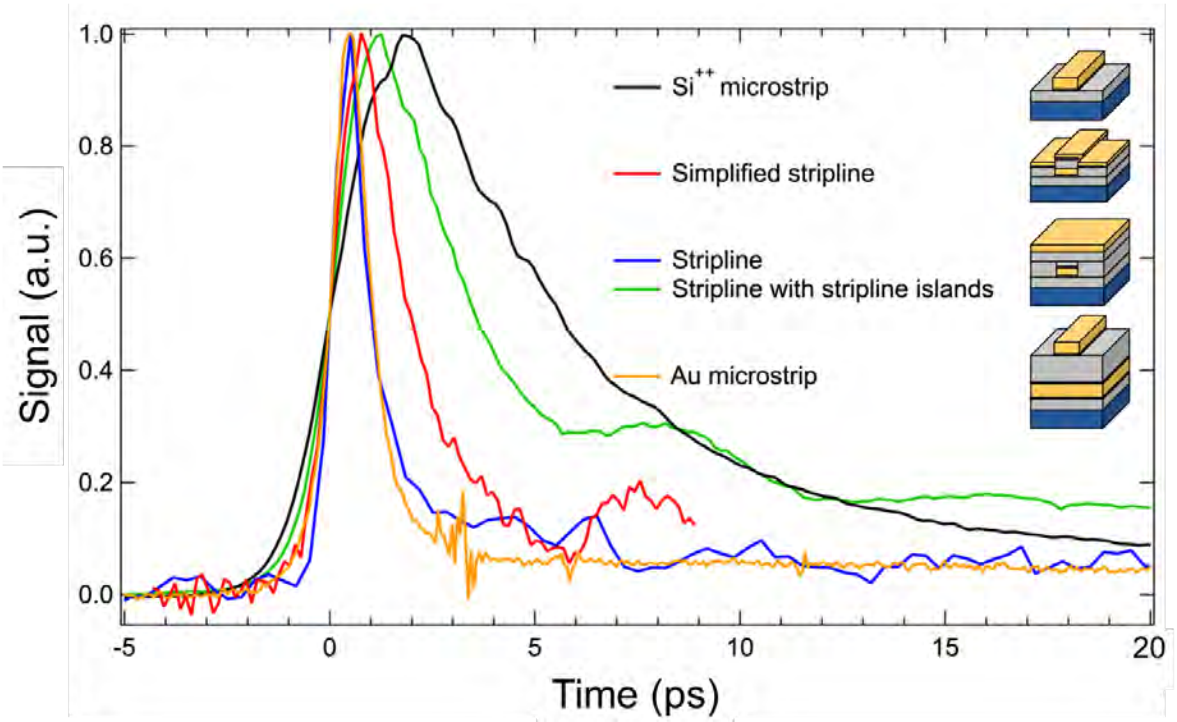

Figure 4.12.: Measured signals in the gold microstrip and all other fabricated samples after 400 µm propagation distance: The signal has a FWHM of 5.9 ps in the doped silicon microstrip, a FHWM of 2.0 ps in the simplified stripline, a FWHM of 1.1 ps in the stripline, a FWHM of 3.5 ps in the stripline with stripline islands and a FWHM of 1.1 ps in the gold microstrip.

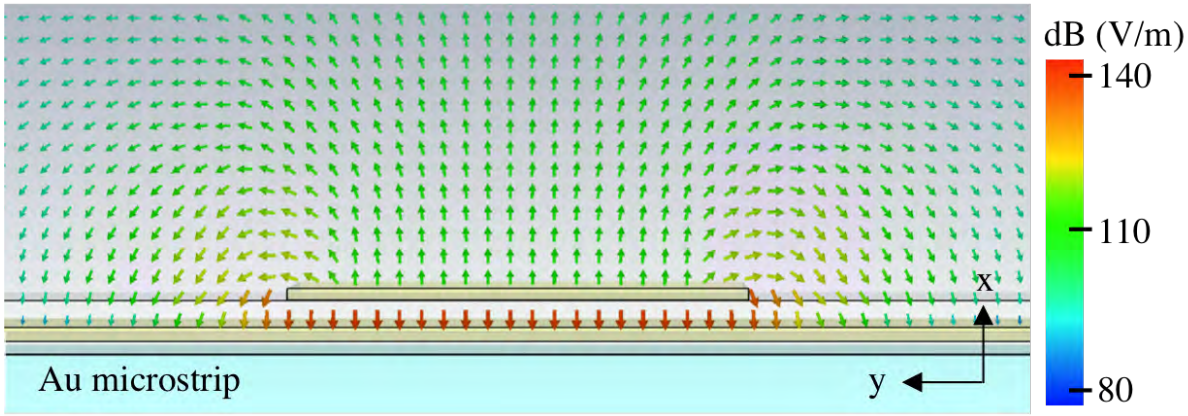

Figure 4.13.: Cross section of the electric field of the THz pulse in the gold microstrip: The electric field lines are strongly confined between the gold signal line and the gold ground.

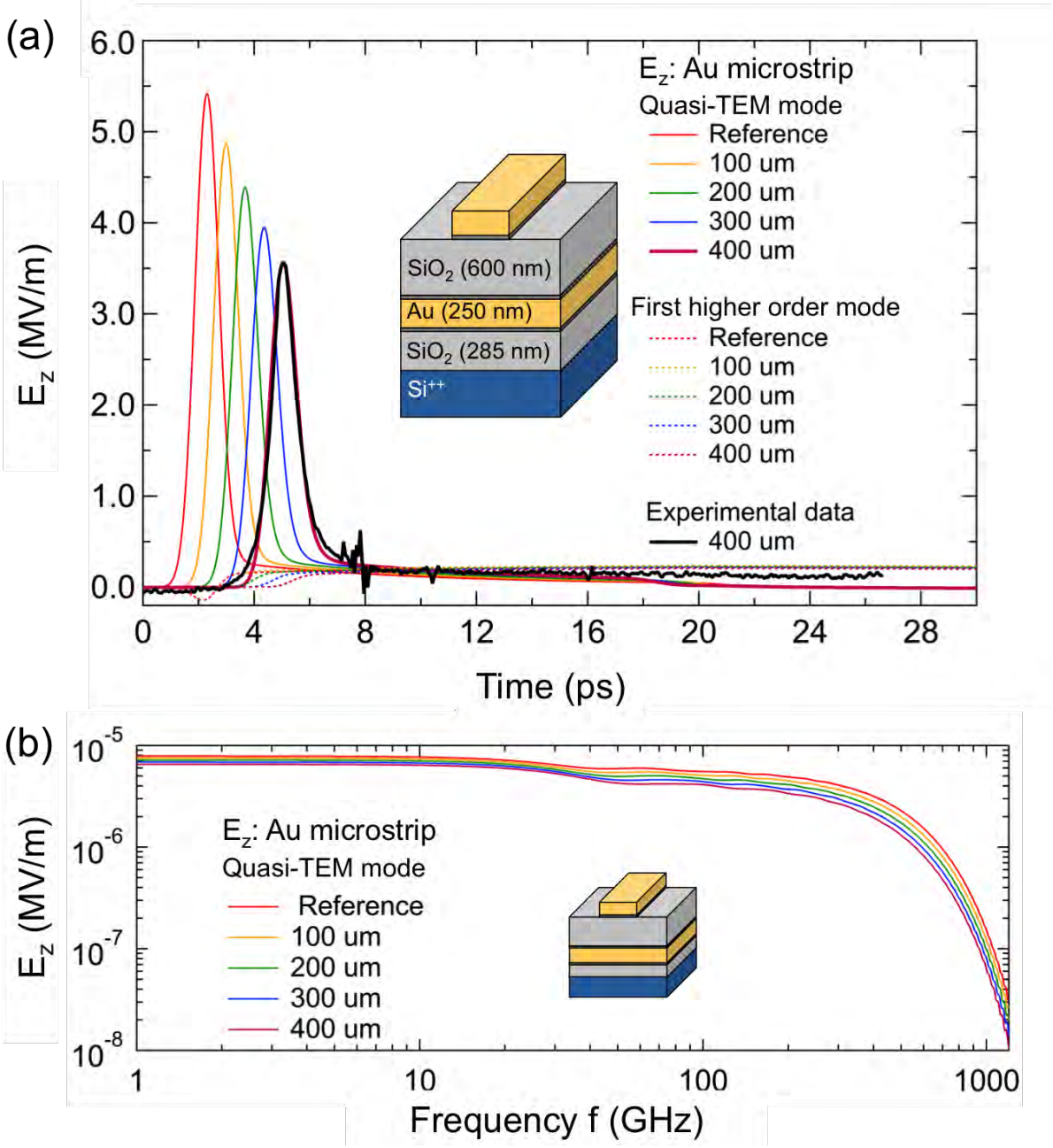

Figure 4.14.: Simulated and measured signal propagation in a gold microstrip with 600 nm thick oxide layer and 10 µm wide signal lines. The dominating quasi-TEM mode (solid lines) and the first higher order mode (dashed lines) are shown. The measured pulse after 400 µm propagation (black line) is in good agreement with the simulation. The signal bandwidth is almost constant for all propagation distances.

5. Discussion

This chapter discusses the results from measurements as well as electromagnetic simulations. To explain the differences in damping and dispersion of the different transmission line geometries, further simulations of common transmission line properties such as real and imaginary part of the propagation constant γ, characteristic impedance Z, and phase velocity v_{ph} are shown and discussed here for the eight different geometries listed in table 5.1. Besides the structures studied in the experimental part, four adjusted gold and doped silicon microstrips with different dielectric thicknesses and signal strip widths are discussed here. Further, also the skin effect in gold and doped silicon as well as origins of losses in the fabricated samples are studied.

Table 5.1.: Simulated transmission lines: The first four transmission lines correspond to the fabricated and measured samples in this thesis. The last four transmission lines are adjusted doped silicon and gold microstrips with smaller signal line widths and different dielectric thicknesses.

Transmission line	Dielectric thickness	Signal line width
Si^{++} microstrip	285 nm	10 µm
Simplified stripline	285 nm on top & bottom of signal line	10 µm
Stripline	285 nm on top & bottom of signal line	10 µm
Au microstrip	600 nm	10 µm
Si 1 (microstrip)	285 nm	6 µm
Si 2 (microstrip)	600 nm	6 µm
Au 1 (microstrip)	285 nm	6 µm
Au 2 (microstrip)	600 nm	6 µm

The experimental and simulated results for the fabricated transmission lines show that the stripline samples already provide a great improvement in dispersion, damping as well as band width preservation in comparison to the doped silicon microstrip, which has been used in formed on-chip THz experiments. However, THz frequencies are vanishing in striplines (see figure 4.11) and also higher order modes are propagating.

These problems could be solved with the gold microstrip. The gold microstrip differs from the doped silicon microstrip by the conductive material of the ground line and by the thickness of the dielectric (doped silicon microstrip: 285 nm SiO_2, gold microstrip: 600 nm SiO_2). In order to distinguish the impact on the signal propagation, the real part (α) and imaginary part (β) of the propagation constant γ are studied for the eight different transmission line geometries listed in table 5.1 (see figure 5.1).

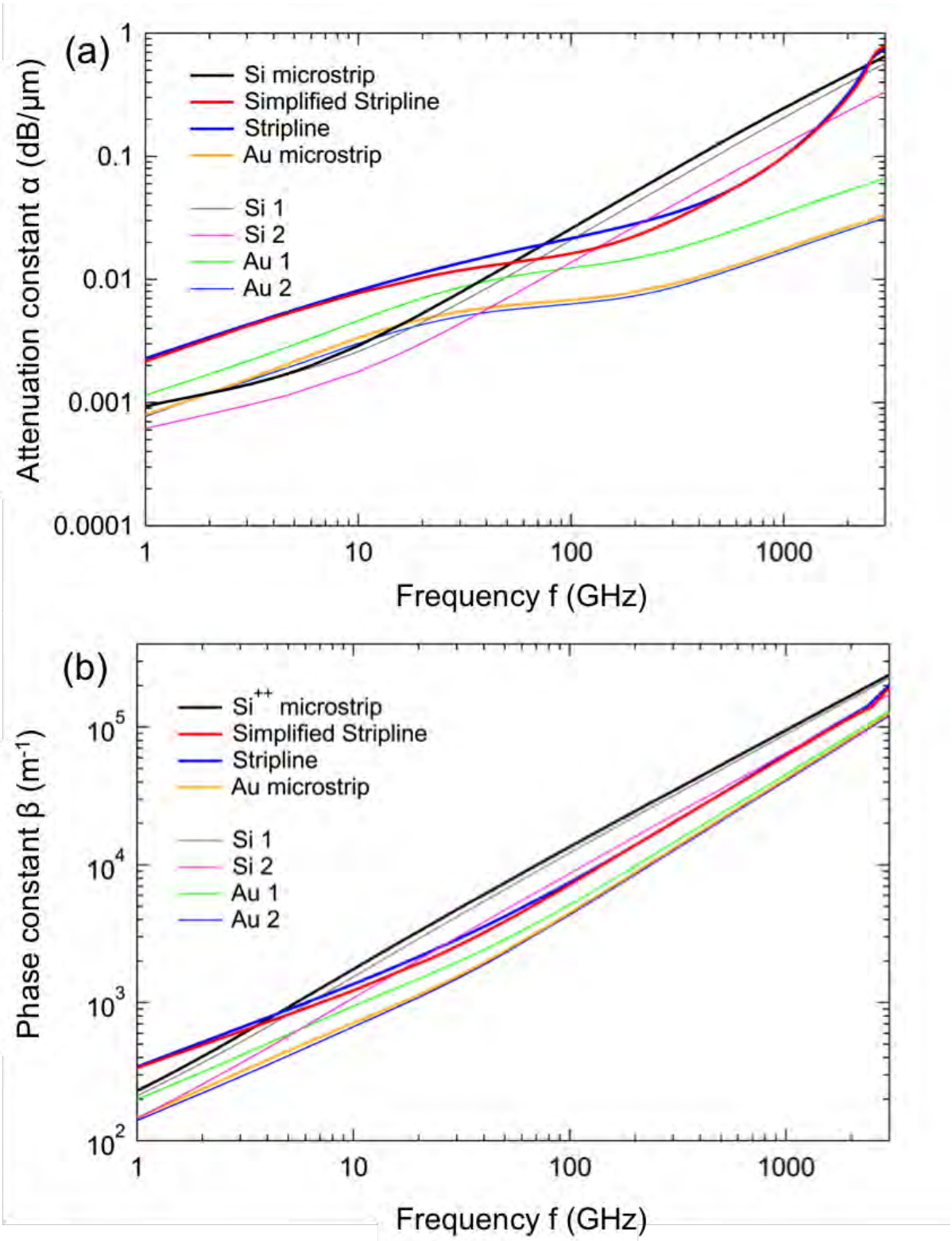

Figure 5.1.: Real part α (a) and imaginary part β (b) of the propagation constant γ for eight simulated transmission line geometries: α corresponds to the attenuation and β to the distortion (phase). Attenuation and distortion is lowest for the gold microstrip with 600 nm thick dielectric and 6 µm broad signal strips.

As discussed in chapter 2.2.2, the real part α corresponds to the signal attenuation and the imaginary part β to the signal dispersion. Regarding figure 5.1, α and β are highest for THz frequencies in the doped silicon microstrips. The stripline geometries provide an improvement, but are beaten by the gold microstrip.

Figure 5.1 shows that narrower signal lines (compare Au microstrip (yellow) and Au 2 (blue)) and thicker dielectrics (compare Au 1 (green) and Au 2 (blue)) lead to lower attenuation and less dispersion. Thus, signals propagating in gold microstrips with 600 nm SiO_2 thickness and 6 µm signal line widths experience the lowest amount of damping and distortion in comparison to all other simulated structures.

In figure 5.2 (a), the characteristic impedance Z is shown. One finds that Z is lowest for the stripline structures, followed by the gold microstrips and highest for the doped silicon structures. Further, the characteristic impedance is higher for smaller signal strip widths and thicker dielectrics. However, the main message, that the curves for the characteristic impedance show, is not the value of Z by itself, but the transition frequencies to the weak damping limit of the different geometries. As discussed in chapter 2.2.2 (figure 2.7), Z approaches a constant value Z_0 in the weak damping limit for frequencies $\omega \gg R'/L'$ and $\omega \gg G'/C'$ (frequency-dependent simulations of the primary line constants R', L', C' and G' are shown in Appendix A of this thesis). Signals are propagating without distortion in the weak damping limit.

Regarding figure 5.2 (a), the characteristic impedance of the gold microstrips approaches a constant value at frequencies higher than 100 GHz. For the two stripline designs, the weak damping limit is reached at frequencies higher than 130 GHz. For the doped silicon microstrip, the plateau cannot be seen in the depicted frequency range. Thus, the doped silicon microstrip does not reach the weak damping limit within the bandwidth of the generated pulses. The lower the transition frequency to the weak damping limit, the less dispersive is the transmission line, meaning that also the simulation results for the characteristic impedance show, that the gold microstrip is least dispersive compared to all other structures.

Figure 5.2 (b) presents the simulation results for the frequency-dependent phase velocities in units of the vacuum light velocity c_0 of the eight simulated transmission lines. The phase velocity is increasing with increasing frequency and the highest frequency component propagated with the maximum phase velocity. The gold microstrips have a maximum phase velocity of $\sim 0.5c_0$, the striplines of $\sim 0.35c_0$ and the doped silicon microstrips of $\sim 0.25c_0$. The result for the maximum phase velocity of the doped silicon microstrip is in good agreement with the measured maximum phase velocity of the fabricated sample (see equation 4.1).

Further, the phase velocities of the gold microstrips are approaching a constant value for frequencies higher than 100 GHz (weak damping limit), which causes less dispersion, since those frequency components travel with the same velocity.

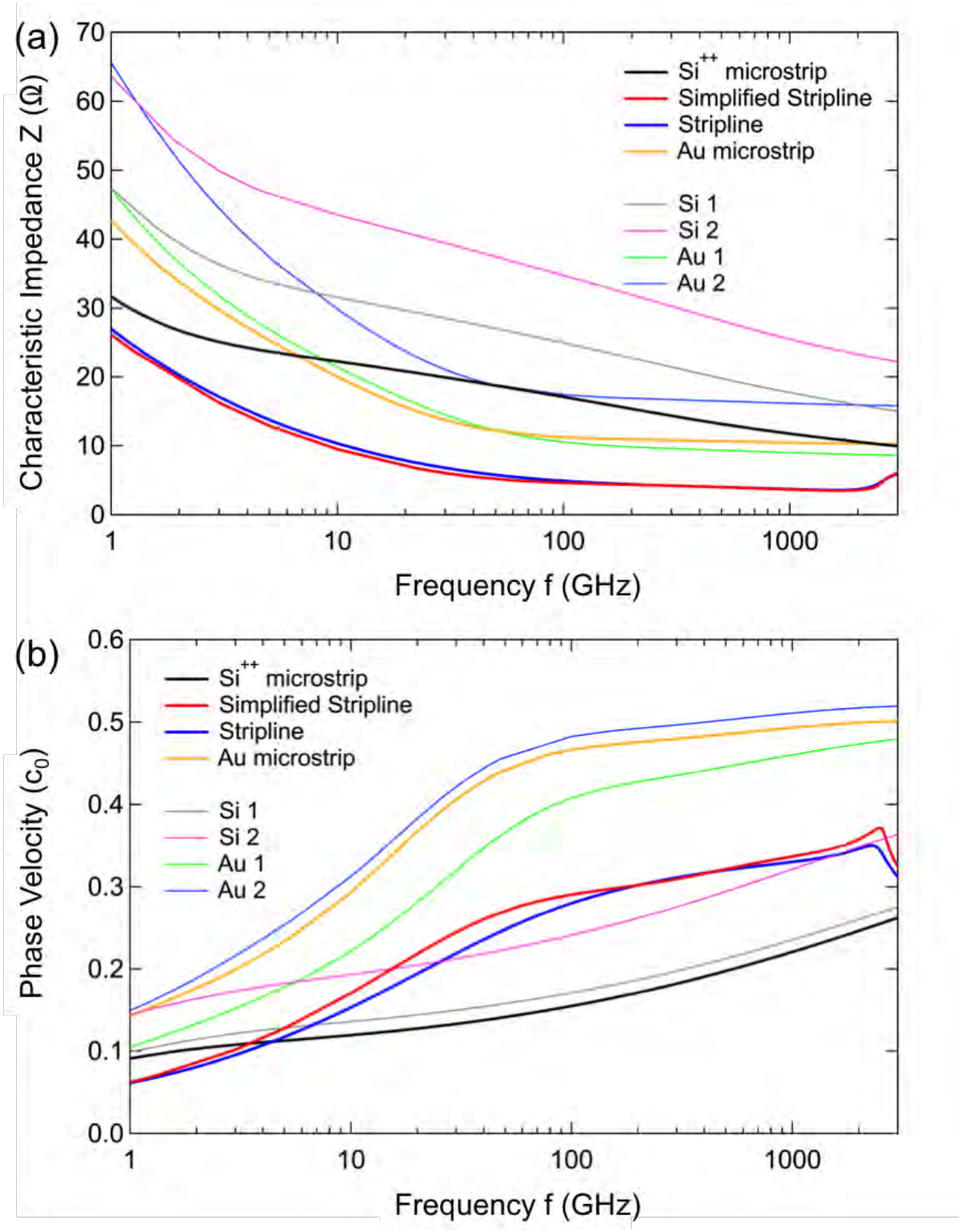

Figure 5.2.: Characteristic impedance Z (a) and phase velocity v_{ph} (b) in units of the speed of light in vacuum c_0.

The previous discussion shows that the microstrip geometry (dielectric thickness, signal line width) influences the amount of signal damping and distortion, but the material used as a conductive ground line has the highest impact on the signal propagation. As already discussed, gold has a conductivity of $4.6 \cdot 10^7$ S/m and as shown in chapter 4.1, the conductivity of doped silicon was measured to be $3.3 \cdot 10^5$ S/m. Accompanied by the different conductivities, the two conductive materials have also different skin depths (see chapter 2.2.4). The frequency-dependent skin depth can be calculated from equation 2.21 for the two different materials as shown in figure 5.3. One finds that the skin depth in doped silicon is approximately 40 times higher than in gold.

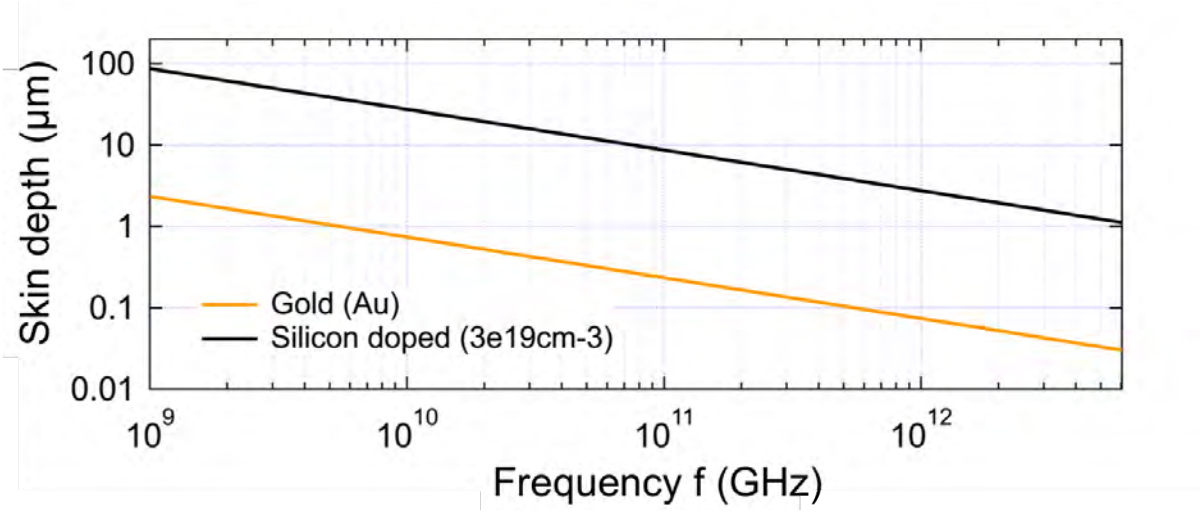

Figure 5.3.: Calculated skin depths of gold (σ = $4.6 \cdot 10^7$ S/m) and doped silicon (σ = 30,000 S/m) as function of frequency ω. The skin depth in doped silicon is roughly 40 times larger than in gold.

As shown in equation 2.21, the skin depth δ is proportional to the inverse of the square root of the conductivity σ:

$$\delta \propto \frac{1}{\sqrt{\sigma}}. \tag{5.1}$$

Since the conductance G of a transmission line is proportional to the product of conductivity σ and skin depth δ, G is proportional to the inverse of δ:

$$G \propto \sigma \cdot \delta \propto \frac{1}{\delta}. \tag{5.2}$$

Therefore, the conductance G of the transmission line is decreasing with increasing skin depth. In particular, the conductance in doped silicon is 40 times worse than in gold. This is leading to a higher amount of conductor losses in doped silicon.

Figure 5.4 shows the results of simulated conductor losses for the doped silicon microstrip, the stripline and the gold microstrip. Conductor losses in the doped silicon

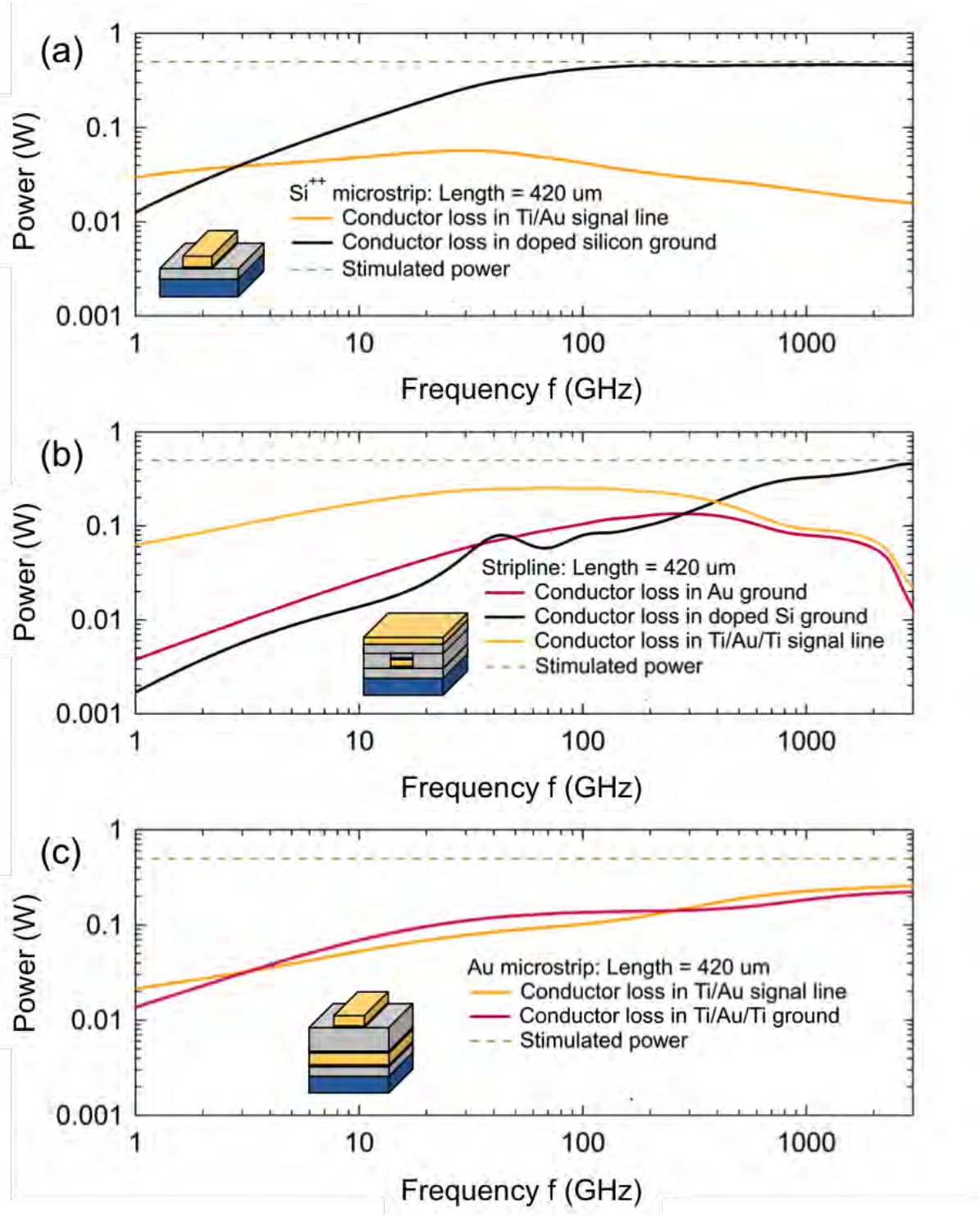

Figure 5.4.: Simulated conductor and radiation losses after 420 µm of propagation as function of frequency ω for the fabricated samples: (a) Doped silicon microstrip. (b) Stripline. (c) Gold microstrip. The dashed lines indicate the imprinted power of the waves at the input port. Conductor losses in the doped silicon microstrip and stripline mainly arise in the doped silicon ground. Especially THz frequencies are lost in the doped silicon microstrip. Conductor losses also occur in the gold signal line (all three structures) and the gold grounds (stripline and gold microstrip), but these losses are orders of magnitudes smaller compared to the losses in the doped silicon. Conductor losses in the doped silicon of the wafer do not arise in the gold microstrip, since the gold ground acts as a shield.

microstrip and in the stripline mainly arise due to the doped silicon ground for THz frequencies. THz frequencies are almost completely lost. Conductor losses also occur in the gold signal line and the gold ground, but these losses are significantly smaller compared to the losses in the doped silicon. This reveals that doped silicon is a bad choice as a ground material for transmission lines.

6. Conclusion and outlook

In this thesis, low-dispersive, single-mode transmission line geometries have been investigated for on-chip THz spectroscopy measurements. Five different transmission line geometries have been fabricated to characterize the signal propagation via pump-probe measurements. Firstly, a doped silicon microstrip was measured, the geometry that has been used in formed on-chip THz experiments. This structure is the benchmark for the more sophisticated geometries: The three different types of striplines and the gold microstrip.

Experiments and simulations have shown that the stripline geometry provides improvements for the propagation of THz signals compared to the doped silicon microstrip. In the doped silicon microstrip, signals disperse from 1 ps to 5.9 ps after 300 µm propagation. The signal is damped by approximately 75 % and the bandwidth decreases drastically that nearly all THz frequency components vanish after this short propagation distance. The stripline geometry provides an improved dispersion of only 1.1 ps (measured) or 1.9 ps (simulated) and damping of 50 % after 300 µm propagation. Further, the bandwidth is higher and some THz frequencies are preserved. However, the gold microstrip significantly surpasses the stripline geometry. Signals report a minimum amount of dispersion (1.1 ps) as well as damping ($\sim$ 30 %) after 300 µm propagation and the transmission line geometry preserves the entire bandwidth of the propagating pulse. Therefore, it turned out that not the geometry by itself has the highest impact on dispersion and damping. Moreover, it is the conductivity of the ground material. Doped silicon has a specific conductivity that is three orders of magnitudes lower than the specific conductivity of gold. This causes a high amount of conductor losses in the doped silicon, especially of the desired higher (THz) frequency components of the signal.

Besides the improved signal propagation, a further advantage of the gold microstrip geometry is the rather simple fabrication process. The gold/ SiO_2 substrate can be prepared prior to the fabrication of delicate samples such as twisted bilayer or other multilayer heterostructures. After the sample is placed on the substrate, every step of the lithography process increases the risk of damaging or losing the sample. Therefore, the two steps of lithography and evaporation required to build the photoconductive switches and the transmission lines of a gold microstrip device are ideal compared to the five steps required for the stripline geometry.

In addition, it was shown that thicker dielectrics (600 nm instead of 285 nm) and narrower signal lines (6 µm instead of 10 µm) further improve the signal propagation in the microstrip geometry.

The novel transmission line geometry of choice has a broad range of different applic-

ations in the future. For example, they can be used to perform on-chip THz spectroscopy experiments on structures such as twisted bilayer graphene at millikelvin temperatures to explore superconducting states. In this case, the sample has to be placed in a closed millikelvin cryostate and the photoconductive switches need to be operated without direct optical access. Therefore, fiber optics are required to guide laser pulses into the setup. In the framework of this thesis, preliminary results are achieved by implementing fiber-coupled pump beams in the experimental pump-probe setup (see Appendix B).

A further application of fiber-coupled photoconductive switch devices can be found in the combination of scanning near-field optical microscopy (SNOM) experiments of current pumped materials, which are planned in collaboration with the group of Professor Dimitri Basov from the Columbia University in New York. This experiment is motivated by the desire to understand the interaction between ultrashort current pulses generated by a photoconductive switch with a material such as (twisted) bilayer graphene. Possible phenomena that may emerge include plasmonic waves or band gap openings in bilayer graphene structures. In order to perform such experiments, a fiber-coupled pump beam has to be implemented in the SNOM setup. In this thesis, first steps are taken by developing a SNOM stage that allows sample mounting, beam alignment, as well as focussing via fiber optics in the SNOM setup (see Appendix C).

At the moment, delicate bilayer graphene samples encapsulated in boron nitride with a graphite backgate for a first current pump - SNOM probe experiment in collaboration with the Columbia University are in fabrication. Another experiment that will be pursued in the framework of a PhD position is the integration of on-chip THz spectroscopy in a millikelvin magnet setup. A first exciting experiment in this new setup is the characterization of the superconducting states in twisted bilayer graphene.

Bibliography

[1] D. N. Basov, R. D. Averitt, D. Hsieh, *Towards properties on demand in quantum materials*, Nature materials, 16, 1077, doi:110.1038/NMAT5017, 2017.

[2] P. Salen, M. Basini, S. Bonetti, J. Hebling, M. Krasilnikov, A. Y. Nikitin, G. Shamuilov, Z. Tibai, V. Zhaunerchyk, V. Goryashko, *Matter manipulation with extreme terahertz light: Progress in the enabling THz technology*, Physics Report, 836-837, 1-74, doi:10.1016/j.physrep.2019.09.002, 2019.

[3] Peng Han, Xinke Wang, Yan Zhang, *Time-Resolved Terahertz Spectroscopy Studies on 2D Van der Waals Materials*, Advanced Optical Materials, doi:10.1002/adom.201900533, 2019.

[4] D. H. Auston, *Picosecond optoelectronic switching and gating in silicon*, Applied Physics Letters, 26, 101, doi:10.1063/1.88079, 1975.

[5] M. Kumar, *The Development of On-Chip THz Time-Domain Spectroscopy*, The University of Leeds, School of Electronic and Electrical Engineering, Dissertation, 2016.

[6] A. J. L. Adam, *Review of Near-Field Terahertz Measurement Methods and Their Applications*, Journal of Infrared, Millimeter, and Terahertz Waves, 32, 976, doi:10.1007/s10762-011-9809-2, 2011.

[7] W. Zouaghi, M. Thomson, K. Rabia, R. Hahn, V. Blank, H. Roskos, *Broadband terahertz spectroscopy: principles, fundamental research and potential for industrial applications*, European Journal of Physics, 34, 179, doi: 10.1088/0143-0807/34/6/S179, 2013.

[8] J. W. McIver, B. Schulte, F.-U. Stein, T. Matsuyama, G. Jotzu, G. Meier, A. Cavalleri, *Light-induced anomalous Hall effect in graphene*, Nature Physics, doi:10.1038/s41567-019-0698-y, 2019.

[9] W. Ghann, J. Uddin, *Terahertz (THz) Spectroscopy: A Cutting-Edge Technology*, doi:10.5772/67031, 2017.

[10] A. von Hoegen, R. Mankowsky, M. Fechner, M. Först, A. Cavalleri, *Probing the Interatomic Potential of Solids with Strong-Field Nonlinear Phononics*, Nature, 555, 79-82, doi:10.1038/nature25484, 2018.

[11] M. Mitrano, A. Cantaluppi, D. Nicoletti, S. Kaiser, A. Perucchi, S. Lupi, P. Di Pietro, D. Pontiroli, M. Riccò, S. R. Clark, D. Jaksch, and A. Cavalleri, *Possible light-induced superconductivity in K3C60 at high temperature*, Nature, 530, 461-464, doi:10.1038/nature16522, 2016.

[12] S. Rajasekaran, J. Okamoto, L. Mathey, M. Fechner, V. Thampy, G. D. Gu, A. Cavalleri, *Probing optically silent superfluid stripes in cuprates*, Science, 369, 6375, 575-579, doi:10.1126/science.aan3438, 2018.

[13] P. Y. Han, X.-C. Zhang, *Free-space coherent broadband terahertz time-domain spectroscopy*, Measurement Science and Technology, 12, 11, doi:10.1088/0957-0233/12/11/301, 2001.

[14] MPSD - condensed matter dynamics department, *Broadband Time-resolved terahertz spectroscopy*, http://qcmd.mpsd.mpg.de/index.php/Broadband-Time-resolved-terahertz-spectroscopy.html, Request: 10/2019.

[15] P. H. Siegel, *Terahertz Pioneer: David H. Auston*, IEEE Transactions on Terahertz Science and Technology, 1, 1, 6-8, doi:10.1109/TTHZ.2011.2151130, 2014.

[16] C. A. Schuttenmaer, *Exploring Dynamics in the Far-Infrared with Terahertz Spectroscopy*, Chemical Reviews, 104, 4, 1759-1780, doi:10.1021/cr020685g, 2004.

[17] M. C. Nuss, J. Orenstein, *Terahertz time-domain spectroscopy. Millimeter and Submillimeter Wave Spectroscopy of Solids*, Topics in Applied Physics, 74, 7-50, doi:10.1007/BFb0103419, 1998.

[18] Y. Sakai, I. Kawayama, H. Nakanishi, M. Tonouchi, *Visualization of GaN surface potential using terahertz emission enhanced by local defects*, Scientific Reports, 5, 13860, doi:10.1038/srep13860, 2015.

[19] J. Zhang, Y. Hong, S. Braunstein, K. Shore, *Terahertz pulse generation and detection with LT-GaAs photoconductive antenna*, IEE Proceedings - Optoelectronics, 98-101, doi:10.1049/ip-opt:20040113, 2004.

[20] F. DiPaolo, *Fundamental Theory of Transmission Lines*, Networks and Devices Using Planar Transmission Lines, Ph.D., CRC Press LLC, 2000.

[21] O. Heaviside, *Contributions to the Theory of the Propagation of Currents in Wires*, Paper XX in Electrical Papers, 1, 141-181, 1892.

[22] S. R. Talluri, *Analysis of Transmission Line Models with Non Linear Elements for Opposite Phase and Group Velocities*, Jaypee University of Information Technology, Dissertation, chapter 2, 2016.

[23] P. Wilson, *The Circuit Designer's Companion*, Newnes, Fourth Edition, 1-47, 2017.

[24] A. Thiede, *Einführung in die Hochfrequenztechnik*, Universität Paderborn, Lecture Script, 2013.

[25] H. A. Wheeler, *Formulas for the Skin Effect*, Proceedings of the IRE, 30, 9, 412-424, doi:10.1109/JRPROC.1942.232015, 1942.

[26] K. Brun, R, Kurz, *Compression Machinery for Oil and Gas*, Gulf Professional Publishing, 326, doi.org/10.1016/C2017-0-02064-5, 2019.

[27] D. M. Pozar, *Microwave Engineering*, Addison-Wesley Publishing Company, ISBN 978-81-265-4190-4, 2017.

[28] H. A. Wheeler, *Transmission-line properties of parallel wide strips by a conformal-mapping approximation*, IEEE Transactions on Microwave Theory and Techniques, MTT-12, 3, 280-289, doi:10.1109/TMTT.1964.1125810, 1964.

[29] H. A. Wheeler, *Transmission-line properties of parallel strips separated by a dielectric sheet*, IEEE Transactions on Microwave Theory and Techniques, MTT-13, 2, 172-185, doi:10.1109/TMTT.1965.1125962, 1965.

[30] E. O. Hammerstad, *Equations for Microstrip Circuit Design*, 1975 5th European Microwave Conference, 268-272, doi:10.1109/EUMA.1975.332206, 1975.

[31] K. Singh, A.V. Nirmal, and S.V. Sharma, *Study the Loss of Microstrip on Silicon*, Microwaves and RF, 2017, www.mwrf.com/components/study-loss-microstrip-silicon#close-olyticsmodal, Request: 10/2019.

[32] E. J. Denlinger, *A frequency dependent solution for microstrip transmission lines". IEEE Transactions on Microwave Theory and Techniques*, MTT-19, 1, 30-39, doi:10.1109/TMTT.1971.1127442, 1971.

[33] B. Bianco, L. Panini, M. Parodi, S. Ridetlaj, *Some considerations about the frequency dependence of the characteristic impedance of uniform microstrips*, EEE Transactions on Microwave Theory and Techniques, MTT-26, 3, 182-185, doi: 10.1109/TMTT.1978.1129341, 1978.

[34] N. Marcuvitz, *Waveguide handbook*, Institution of Electrical Engineers, ISBN: 9789332873667, 1951.

[35] J. Baker-Jarvis, M. D. Janezic, B. Riddle, C. L. Holloway, N. G. Paulter, J. E. Blendell, *Dielectric and Conductor-Loss Characterization and Measurements on Electronic Packaging Materials*, NIST Technical Note 1520, doi:10.6028/NIST.TN.1520, 2001.

[36] R. K. Hoffmann, *Handbook of microwave integrated circuits*, Norwood, MA, Artech House, Inc., 544, 1, ISBN: 9780890061633, 1987.

[37] R. M. Barrett, *Microwave printed circuits-A historical survey*, Microwave Theory and Techniques, IRE Transactions on, 3, 1-9, doi:10.1109/TMTT.1955.1124910, 1955.

[38] S. H. Hall, G. W. Hall, J. A. McCall, *High-speed digital system design: a handbook of interconnect theory and design practices*, Wiley-Interscience Publication JOHN WILEY & SONS, ISBN: 0471360902, 2000.

[39] C. P. Wen, *Coplanar waveguide: A surface strip transmission line suitable for nonreciprocal gyromagnetic device applications*, Microwave Theory and Techniques, IEEE Transactions on, 17, 1087-1090, doi:10.1109/TMTT.1969.1127105, 1969.

[40] R. N. Simons, *Coplanar Waveguide Circuits, Components, and Systems*, Wiley, 1-2, ISBN: 9780471463931, 2004.

[41] D. Grischkowsky, I. Duling III, J. Chen, C.-C. Chi, *Electromagnetic shock waves from transmission lines*, Physical review letters, 59, 1663, doi:10.1103/PhysRevLett.59.1663, 1987.

[42] J. Jelley, *Cerenkov radiation and its applications*, British Journal of Applied Physics, 6, 227, 1955.

[43] KLayout, *KLayout - High Performance Layout Viewer And Editor*, https://www.klayout.de/index.php.

[44] Yanglong Hou, David J. Sellmyer, *Magnetic Nanomaterials: Fundamentals, Synthesis and Applications*, Wiley-VCH, 104, ISBN:352734134X, 9783527341344, 2017.

[45] Haluska *et al.*, *Multilayer ceramics from hydrogen silsequioxane*, United States Patent, 4756977, 1986.

[46] M. Loboda, C. Grove, R. Schneider, *Properties of a-SiO x: H Thin Films Deposited from Hydrogen Silsesquioxane Resins*, Journal of the Electrochemical Society, 145, 2861-2866, doi:10.1149/1.1838726, 1998.

[47] V. Belot, R. Corriu, D. Leclercq, P. H. Mutin, A. Vioux, *Thermal reactivity of hydrogenosilsesquioxane gels*, Chem. Mater., 3, 127, doi:10.1021/cm00013a029, 1991.

[48] C.-C. Yang, W.-C. Chen, *The structures and properties of hydrogen silsesquioxane (HSQ) films produced by thermal curing*, Journal of Materials Chemistry, 12, 1138-1141, doi:10.1039/b107697n, 2002.

[49] F. Levy, *Film Growth and Epitaxy: Methods*, Reference Module in Materials Science and Materials Engineering, 2016.

[50] W. W. Pultz, W. Hertl, *SiO2+SiC reaction at elevated temperatures. Part 1. Kinetics and mechanism*, Transactions of the Faraday Society, 62, doi:10.1039/TF9666202499, 1966.

[51] P. Wagner, M. Hegner, H.-J. Guentherodt, G. Semenza, *Formation and in Situ Modification of Monolayers Chemisorbed on Ultraflat Template-Stripped Gold Surfaces*, Langmuir, 11, 10, 3867-3875, doi:10.1021/la00010a043, 1995.

[52] L. J. van der Pauw, *A method of measuring specific resistivity and Hall effect of discs of arbitrary shape*, Philips Research Reports, 13, 1-9, 1958.

[53] F. Caspers, *RF engineering basic concepts: S-parameters*, https://cds.cern.ch/record/1415639/files/p67.pdf, requested: 11/2019, 2012.

[54] J. Kerr, *A new relation between electricity and light: Dielectrified media birefringent*, Philosophical Magazine, 4, 50, 332, 337-348, doi:10.1080/14786447508641302, 1875.

[55] S. Dai, Z. Fei, Q. Ma, A. S. Rodin, M. Wagner, A. S. McLeod, M. K. Liu, W. Gannett, W. Regan, K. Watanabe, T. Taniguchi, M. Thiemens, G. Dominguez, A. H. Castro Neto, A. Zettl, F. Keilmann, P. Jarillo-Herrero, M. M. Fogler, D. N. Basov, *Tunable Phonon Polaritons in Atomically Thin van der Waals Crystals of Boron Nitride*, Science, 343, 6175, 1125-1129, doi:10.1126/science.1246833, 2014.

[56] Z. Fei, A. S. Rodin, G. O. Andreev, W. Bao, A. S. McLeod, M. Wagner, L. M. Zhang, Z. Zhao, M. Thiemens, G. Dominguez, M. M. Fogler, A. H. Castro Neto, C. N. Lau, F. Keilmann, D. N. Basov, *Gate-tuning of graphene plasmons revealed by infrared nano-imaging*, Nature, 487, 82-85, 2012.

[57] X. Chen, D. Hu, R. Mescall, G. You, D. N. Basov, Q. Dai, M. Liu, *Modern Scattering-Type Scanning Near-Field Optical Microscopy for Advanced Material Research*, Advanced Materials, 31, 24, doi:10.1002/adma.201804774, 2019.

Acknowledgement

There are many people who supported me performing this thesis and I would like to thank all of them. Besides I would like to give my special thanks to some special people.

Firstly, I have to thank my research supervisors, Professor Andrea Cavalleri and PD Guido Meier. I am grateful to Andrea to give me the great opportunity to perform this master thesis in his working group. It was an impressive experience. Furthermore, big thanks to Guido, who guided me through my thesis in the best way one could wish for.

Secondly, I would like to thank James McIver who always supported me with expertise, good ideas and a spectacular collaboration with the Columbia University. It was a pleasure working with him and I cannot wait to proceed.

Moreover, I would like to thank Benedikt Schulte, who supported me in many cases but especially with teaching me lab procedures, ordering new and new elements and materials as well as discussing challenges my project provided. And thanks for your excellent music taste!

In addition, I am very grateful to Toru Matsuyama who supported me with the transmission line simulations with passion and high expertise.

Further I would like to express my gratitude to Michael Volkmann who constructed the SNOM sample stage and also realized together with Boris Fiedler the sample heating in the evaporator. It sounds easy but it was a puzzle on the grand scale. In this context I would also like to thank Elena Koenig who always provided big support in every cleanroom challenge.

I am thankful to Mehdi Ramin Moayed, who helped me with the magnetron sputtering. And Michele Buzzi, who supported me with his expertise in laser optics.

Thanks also to Kateryna Kusyak, the first assistant I ever had.

Last but not least I want to give my deepest thanks to my family for their endless support, love and understanding.

Eidesstattliche Versicherung

Hiermit bestätige ich, dass die vorliegende Arbeit von mir selbständig verfasst wurde und ich keine anderen als die angegebenen Hilfsmittel – insbesondere keine im Quellenverzeichnis nicht benannten Internet-Quellen – benutzt habe und die Arbeit von mir vorher nicht einem anderen Prüfungsverfahren eingereicht wurde. Die eingereichte schriftliche Fassung entspricht der auf dem elektronischen Speichermedium. Ich bin damit einverstanden, dass die Masterarbeit veröffentlicht wird.

Hamburg, den _____, _____

A. Simulated primary line constants

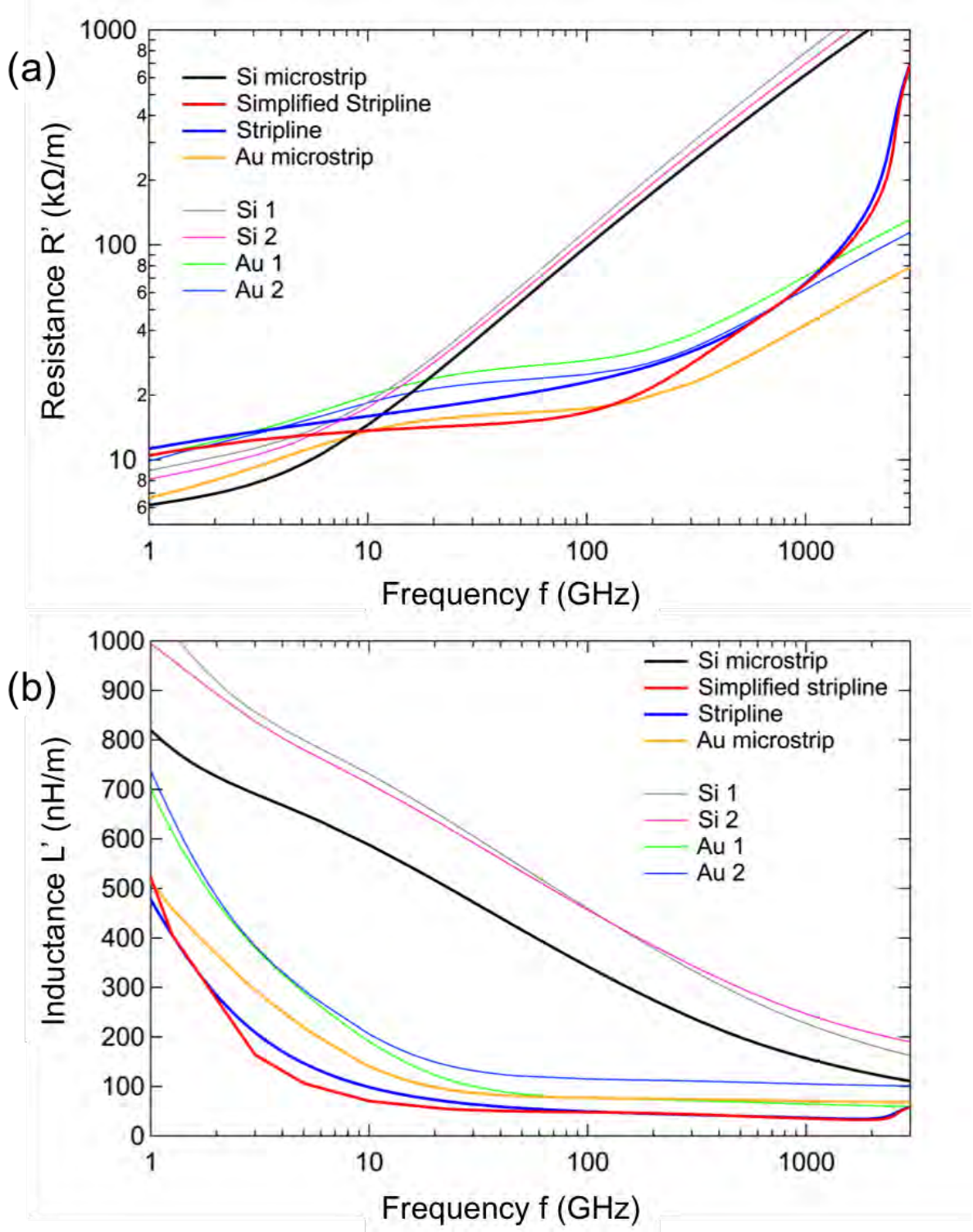

Figure A.1.: Simulated resistance per unit length R' (a) and inductance per unit length L' (b) as function of frequency f for the eight simulated transmission line geometries listed in table 5.1.

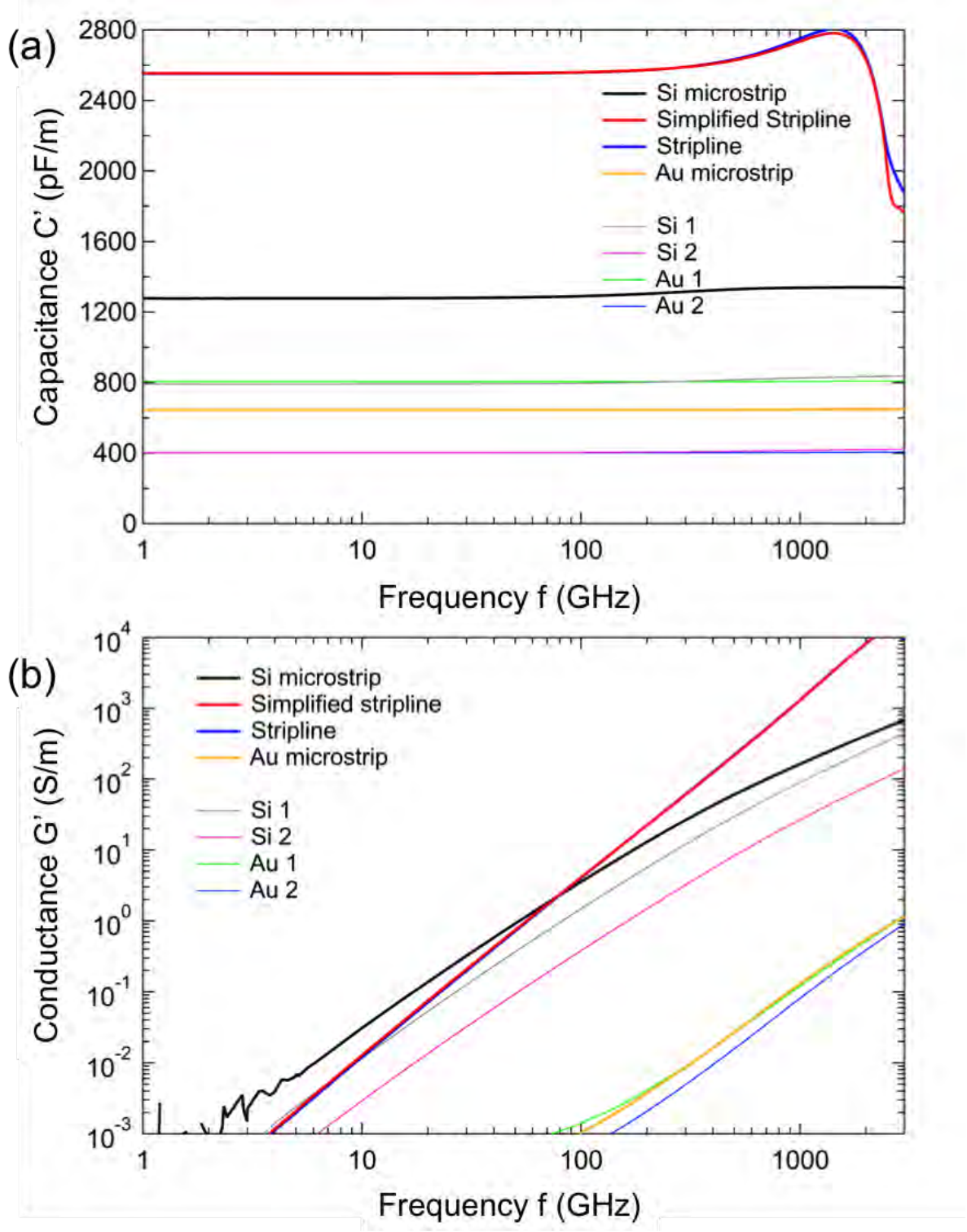

Figure A.2.: Simulated capacitance per unit length C' (a) and conductance per unit length G' (b) as function of frequency f for the eight simulated transmission line geometries listed in table 5.1.

B. Operating THz circuits using fiber optics

In order to conduct future on-chip THz spectroscopy experiments on structures such as twisted bilayer graphene at millikelvin temperatures to exploit superconductive states, samples have to be placed in a closed millikelvin setup. The generation and detection of THz signals via photoconductive switch triggering is then not directly possible. Moreover, fiber optics are required to guide laser pulses into the setup to focus on the sample.

Besides low-dispersive transmission lines, a further step towards advanced on-chip THz spectroscopy at millikelvin temperatures is therefore to operate THz circuits using fiber optics. The following sections describe test measurements that have been performed in order to implement fiber-coupled pump beams in the experimental pump-probe setup.

B.1. Experimental setup

To test whether switches can be triggered with short laser pulses using fiber optics, the pump - probe setup used to measure the signal propagation in different transmission line geometries is modified. A fiber-coupled pump beam is implemented in the setup as depicted in figure B.1.

In order to trigger the photoconductive switches for pump-probe signal data collection, the fiber-coupled pump beam and the probe beam have to be focussed close to each other (400 µm switch distance) on the sample. Since it is rather difficult to realize that both beams are focussed on the sample from one direction, a coplanar waveguide (see chapter 2.3.3) sitting on a transparent sapphire substrate is fabricated. In this coplanar waveguide design, photoconductive switches can be triggered from both sides of the sample. As shown in figure B.2, the pump beam is focussed though the fiber from the back through the two-side polished sapphire on the generation switch and the probe beam is guided through the microscope objective from the frontside onto the sample.

As a first fiber, a 1 m long single-mode fiber with 3.5 µm core diameter is utilized. Laser pulses with 520 nm wavelength, 1 mW power, a repetition rate of 211 kHz and pulse lengths of 500 fs are coupled into the fiber for the pump beam.

The pump-probe measurement results are presented in the following section.

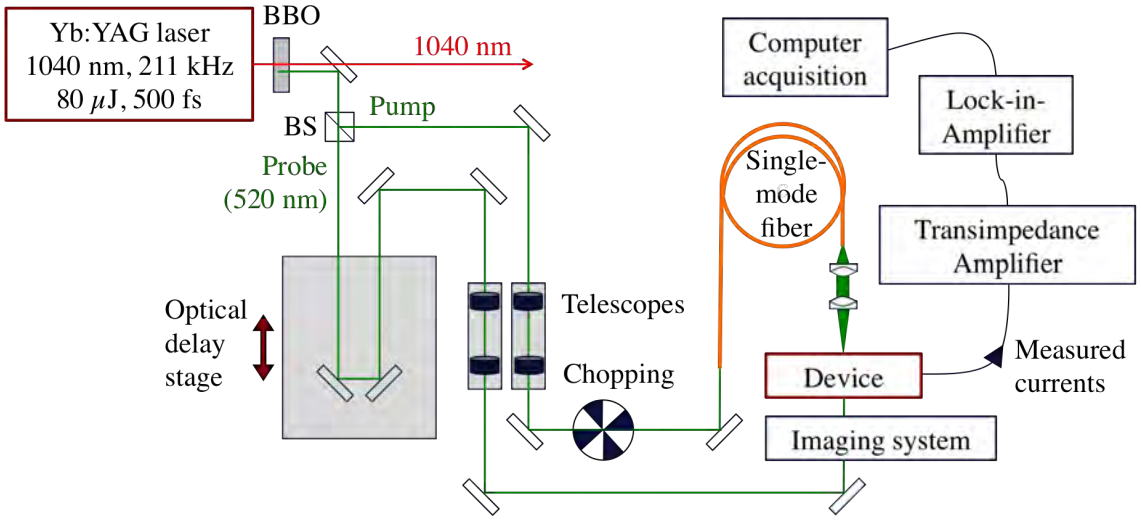

Figure B.1.: Implementation of fiber optics in the pump-probe setup: The pump beam is guided through a single-mode fiber and focussed on the device, which is subject to study. The probe beam is guided through free space and a microscope objective, as in the previous pump-probe setup (see figure 3.16).

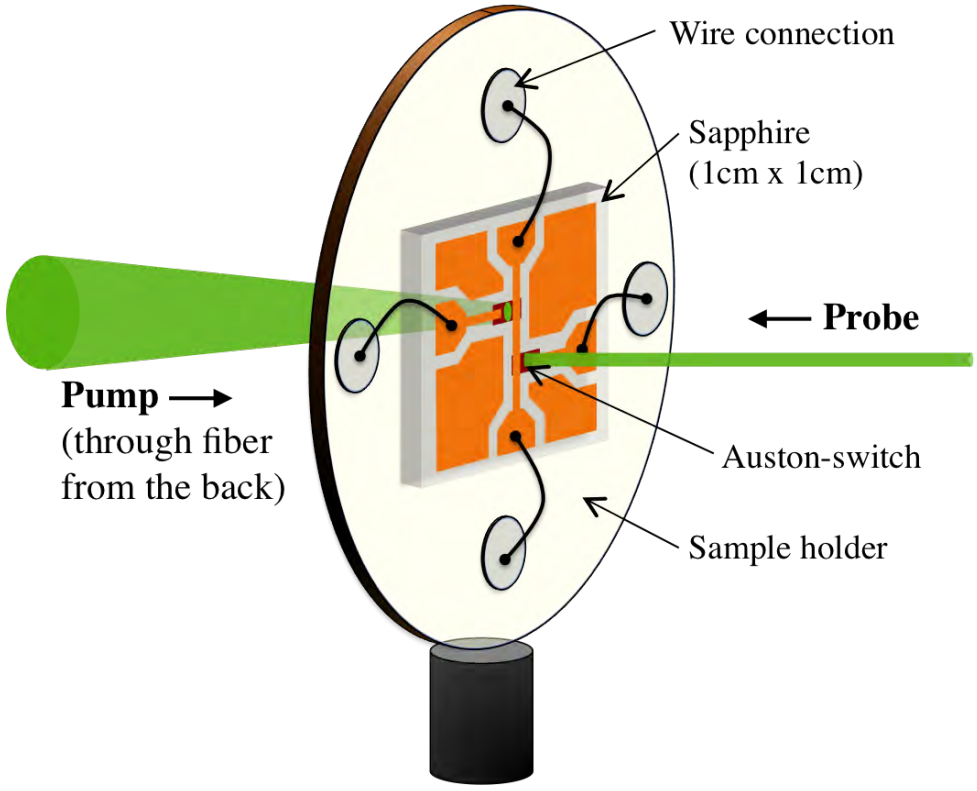

Figure B.2.: Fiber-coupled pump-probe signal measurement on a coplanar waveguide structure: The pump beam is focussed through a fiber from the back on the generation switch and the probe beam is focussed from the front on the detection switch.

B.2. Fiber-coupled current pump generation

Pump-probe signal data collection is performed as previously described in chapter 3.6.2. For the fiber-coupled current pump generation, a bias voltage of 200 V is applied to the generation switch. As shown in figure B.3, switch 1 is used as the generation switch which is triggered from the back through a fiber and through air without a fiber for comparison. Switch 2 is operated as the detection switch without fiber optics.

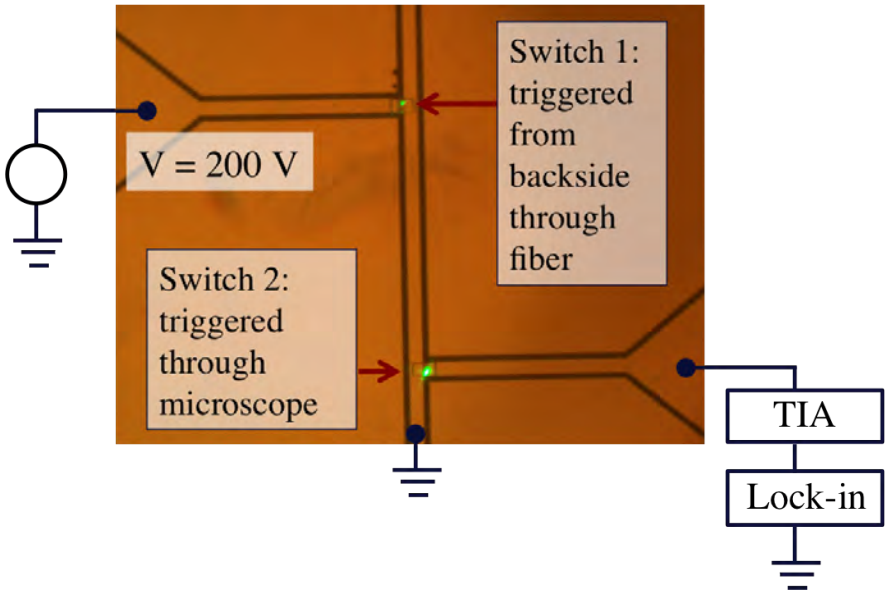

Figure B.3.: Coplanar waveguide sample in measurement: Generation switch 1 is biased with 200 V and triggered from the backside through the fiber. Detection switch 2 is triggered through the microscope. Currents are measured via a transimpedance amplifier and lock-in techniques.

Figure B.4 shows the measured signals without fiber (black curve) and with the 1 m single-mode fiber (red curve). The measured signal width without a fiber amounts to approximately 1.2 ps (FWHM) and with the fiber to 9.9 ps (FWHM). Thus, the fiber causes a pulse broadening by a factor of more than eight.

The reason for the laser pulse dispersion in the fiber is the self-phase modulation, which is caused by the Kerr-effect. The Kerr effect [54] says that the refractive index n of a medium is intensity dependent for high intensities I ($> 10^{14}$ W/m^2):

$$n(I) = n_0 + n_2 \cdot I(t). \tag{B.1}$$

The pump beam with 1 mW laser power, which is guided through the fiber with core diameter of 3.5 µm reaches peak intensities of 10^{15} W/m^2. Thus, self-phase modulation is indeed a problem for the fiber-coupled pump beams. Fortunately, this problem can be avoided using shorter fibers, larger diameter fibers (multimode), phononic crystal fibers or by reducing the laser power.

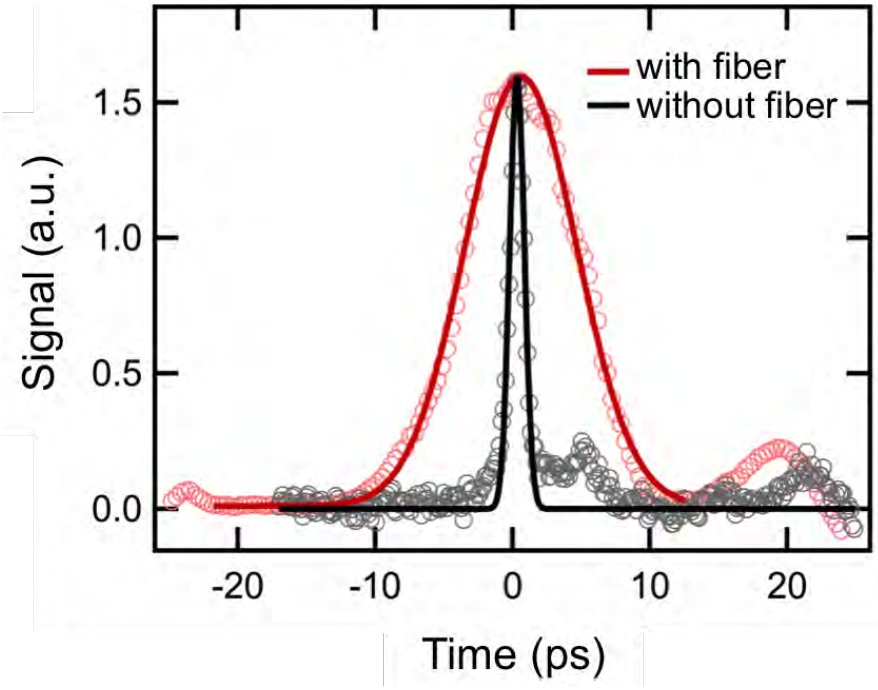

Figure B.4.: Measured signal with and without fiber-coupling of the pump beam: The measured signal width without a fiber (black curve) amounts to approximately 1.2 ps (FWHM) and with the fiber (red curve) to 9.9 ps (FWHM).

Different fibers will be tested in the future in order to reduce the pulse broadening. However, these first test measurements reveal that the generation of fiber-coupled current pumps is possible, moving a further step closer to on-chip THz spectroscopy experiments in a closed millikelvin setup.

C. Fiber-coupled current pump - SNOM probe experiment

A further application of fiber-coupled current pumps can be found in scanning near-field optical microscopy (SNOM) experiments of current pumped materials, which are planned in collaboration with the group of Professor Dimitri Basov from the Columbia University in New York. The motivation is to see what happens if a material such as (twisted) bilayer graphene is pumped with a current (see figure C.1). Possible phenomena are plasmonic wave generation or band gap openings in bilayer structures.

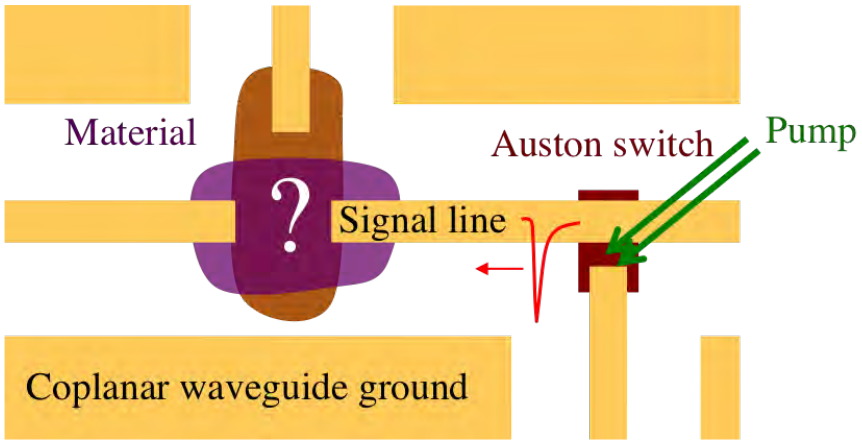

Figure C.1.: What happens when a sample is pumped with a current pulse? To find out which phenomena arise in a material that is contacted in a coplanar waveguide circuit with current pump generation via photoconductive switches, a time-resolved scanning probe is required.

In order to measure such phenomena, a time-resolved scanning probe is required such as SNOM. SNOM promises a detailed characterization of optical properties of materials over a broad spectral range and with fine spatial resolution on the nanoscale. In the last decade, SNOM has become a successful tool to study condensed matter systems such as polaritonic wave propagation in plasmonic or dielectric samples, especially low-dimensional materials (graphene, boron nitride, etc.) [55] and sub-wavelength electrodynamic responses from artificial nanostructures [56], [57].

The working principle of a scanning near-field optical microscope is depicted in figure C.2. In a SNOM, a probe beam is focussed onto the apex of an AFM (atomic force microscopy) tip. The laser interacts with the tip-sample system and is scattered elastically. The backscattered light includes the information of the evanescent waves and can be collected by a detector. Thereby, the far field resolution limit can be broken and local dielectric functions of the sample volume under the tip can be extracted [57].

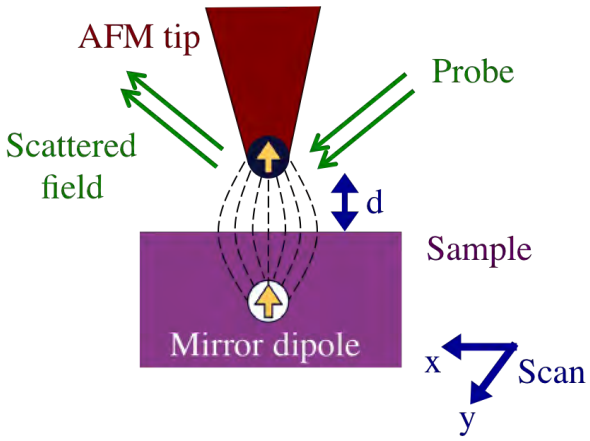

Figure C.2.: Principle of SNOM: A probe beam is focussed on the apex of an AFM tip. Thereby, the near-field of the tip-sample system is confined forming a mirror dipole. The backscattered light includes the near-field information about dielectric properties of the sample and can be collected by a detector.

The SNOM setup at the Columbia university is shown in figure C.3 (a). An AFM tip close to the sample surface is triggered via a focussed pump beam. Scanning can be performed by moving the sample with the sample stage under the fixed AFM tip. In order to implement a current pump beam in the setup, the sample stage has to be modified. There is no space between sample and AFM to focus a laser from the top on the photoconductive switch of the sample. Therefore, the switch has to be triggered from the bottom through fiber optics in a modified sample stage as shown in figure C.3 (b). Both, sample stage and fiber optics have to be movable for the sample scanning.

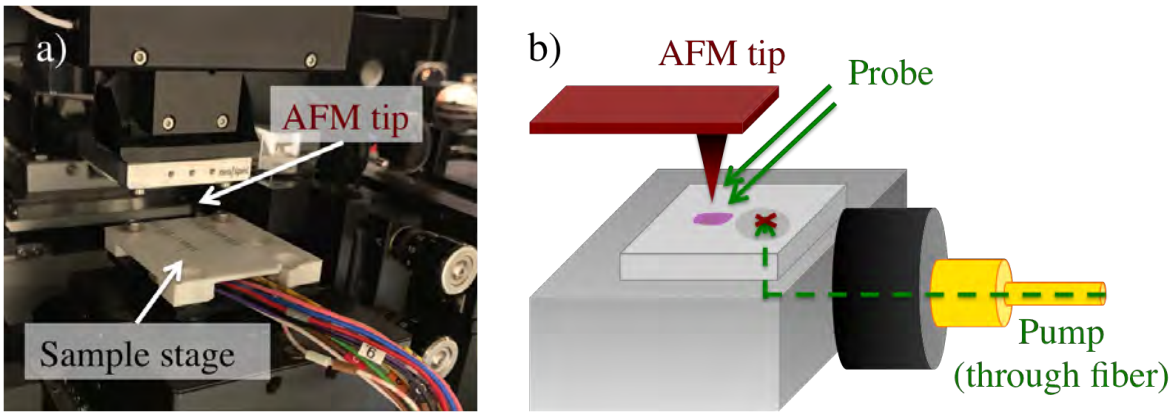

Figure C.3.: SNOM setup at Columbia University: Since there is not enough space between AFM and the sample mounted on a sample stage (a), a modified sample stage is required (b), that focusses a fiber coupled pump beam through the stage from underneath the sample on the photoconductive switch (red cross).

A small sample stage with fiber optics has been developed as depicted in figure C.4. The fiber-coupled pump beam is guided into the stage via a fiberport collimator (f = 4 mm or f = 15 mm). The collimator guides the beam towards a prism mirror in approximately 2 cm distance to the collimator, which reflects the beam onto the sample. The collimator in combination with different lens adapters allows focussing and pointing of the pump beam on the photoconductive switch.

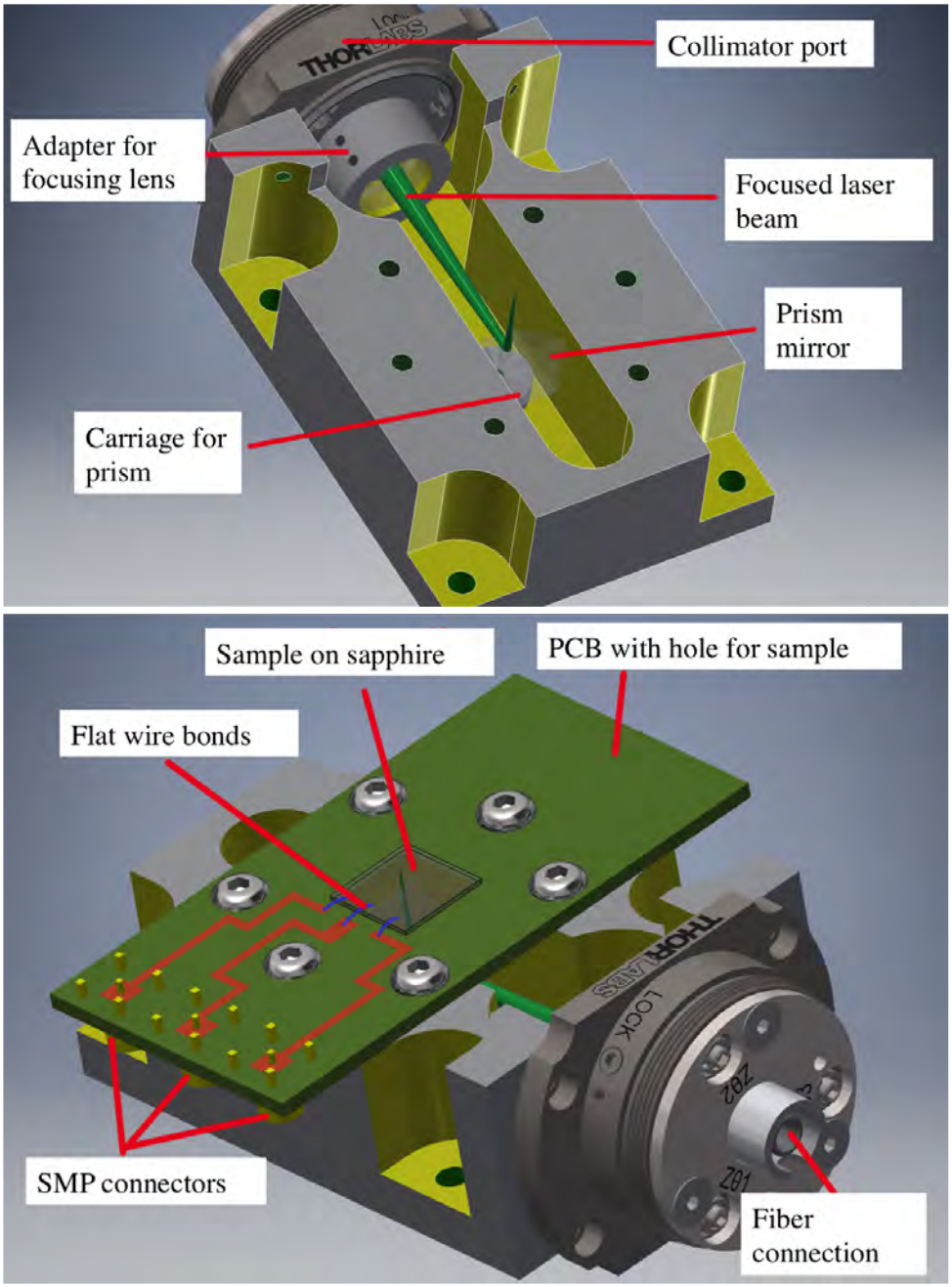

Figure C.4.: Technical drawing of the developed miniature fiber-coupled SNOM sample stage: The fiber-coupled pump beam is coupled to the sample stage via a collimator port, which allows beside sample mounting also the beam alignment as well as focussing.

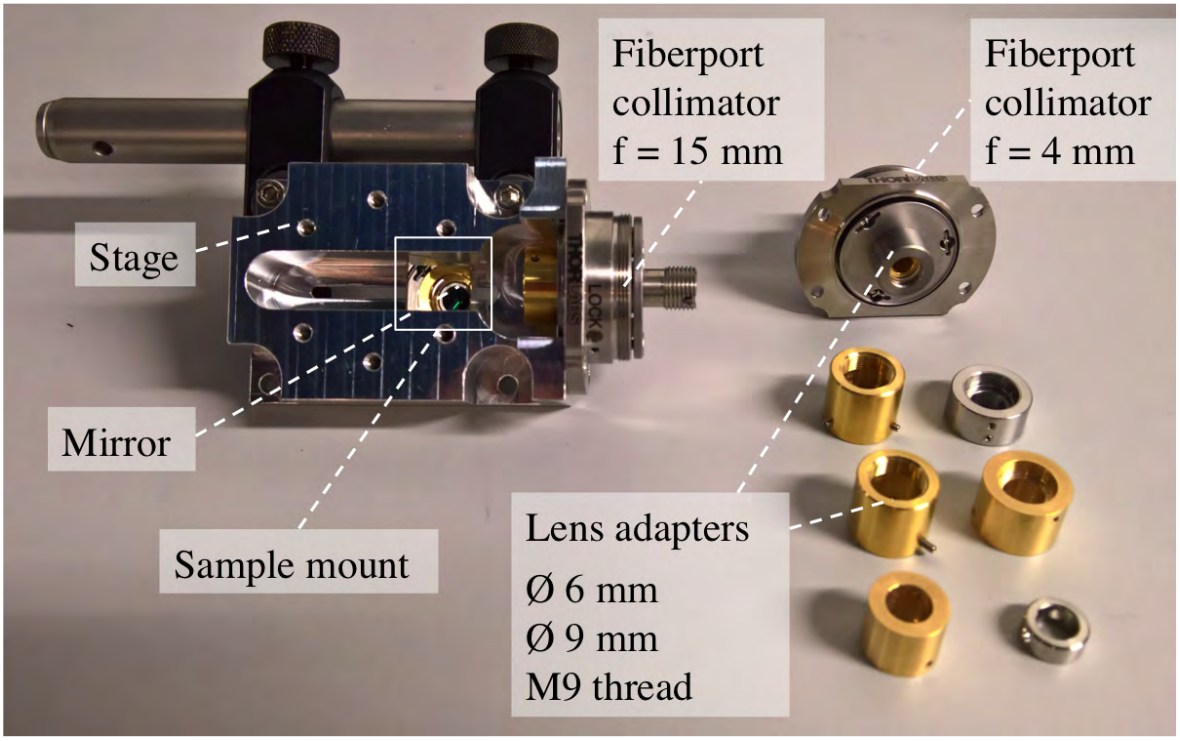

Figure C.5.: Picture of manufactured fiber-coupled SNOM sample stage with two different fiberport collimators (f = 15 mm and f = 4mm), as well as different lens adapters to have some variability concerning beam dimensions and sample adjustment during the measurement time in New York.

A picture of the manufactured fiber-coupled SNOM sample stage is shown in figure C.5. Since the sample stage can just be tested in New York when the experiment is performed, it is desired that the sample stage offers as much variability as possible. Therefore, two different fiberport collimators (f = 15 mm and f = 4 mm) are obtained from Thorlabs and different lens adapters are manufactured to ensure that the laser beam provided in New York can be focussed on the samples.

Since the photoconductive switch has to be triggered from the bottom through the substrate, the sample has to be placed on a two-side polished sapphire in a coplanar waveguide design. The developed gold microstrips from chapter 3 would have been great to use for this experiment, but laser triggering from the backside through the gold substrate is not possible. Fortunately, photoconductive switch triggering from through a sapphire substrate has already been successfully tested as explained in Appendix B.

The next step for this current pump - SNOM probe experiment will be to fabricate delicate samples of bilayer graphene, encapsulated in boron nitride with a graphite backgate, contacted in a coplanar waveguide design on two-side polished sapphire substrates. Graphene was chosen as a first test material for this experiment, since high expertise in graphene sample assembly is already there. Further, a bilayer of graphene might provide the possibility to measure a band gap opening.